

VNIVERSITAT
ID VALÈNCIA  Facultat de Física

Facultat de Física

Departamento de Física Aplicada Y Electromagnetismo



Optical emission at single level and cavity
coupling of low-dimensional perovskite
semiconductors

Tesis Doctoral

Programa de Doctorado en Física

Author:

Setatira Gorji

Supervisors:

Prof. Juan Pascual Martínez Pastor

Dr. Guillermo Muñoz Matutano

Valencia, June, 2023



Dr. Juan Pascual MARTÍNEZ PASTOR, Catedrático del Dpto. de Física Aplicada y Electromagnetismo, y Dr. Guillermo MUÑOZ MATUTANO, Investigador del Dpto. de Física Aplicada y Electromagnetismo, ambos de la Universitat de València

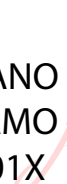
CERTIFICAN que la presente memoria “OPTICAL EMISSION AT SINGLE LEVEL AND CAVITY COUPLING OF LOW-DIMENSIONAL PEROVSKITE SEMICONDUCTORS” resume el trabajo de investigación realizado, bajo su dirección, por Setatira GORJI y constituye su Tesis para optar al Grado de Doctor en Física.

Y para que conste y en cumplimiento de la legislación vigente, firma el presente certificado en Valencia, a



Firmado digitalmente por JUAN PASCUAL[MARTINEZ]PASTOR
Nombre de reconocimiento (DN):
cn=JUAN PASCUAL[MARTINEZ]PASTOR, serialNumber=74214044J,
givenName=JUAN PASCUAL,
sn=MARTINEZ PASTOR,
ou=CIUDADANOS, o=ACCV, c=ES
Fecha: 2023.07.24 18:03:44 +02'00'
Versión de Adobe Acrobat:
2023.003.20244

Fdo. Dr. Juan Pascual Martínez Pastor



MUÑOZ
MATUTANO
GUILLERMO -
24380401X

Digitally signed by
MUÑOZ MATUTANO
GUILLERMO -
24380401X
Date: 2023.07.24
13:11:35 +02'00'

Fdo. Dr. Guillermo Muñoz Matutano



“One thing I have learned in a long life: that all our science, measured against reality, is primitive and childlike, and yet it is the most precious thing we have.”

Albert Einstein

Dedicada a mis padres

Acknowledgements

First of all, I am extremely grateful to my supervisors, Prof. Juan P. Martinez Pastor, and Dr. Guillermo Muñoz Matutano, for their invaluable advice, continuous support, and patience during my PhD study. Their immense knowledge and plentiful experience have encouraged me throughout my academic research and daily life. Sincerely, if Juan hadn't made the obstacles easier to overcome and provided me with the financial assistance to relocate from my home country and join his research group, the road toward earning my PhD would never have taken place. I would like to thank Guillermo. I consider myself extremely lucky to have him as my PhD supervisor, and I am grateful for his guidance and mentoring throughout those years. Not only has he introduced me to the subject of quantum optics and semiconductors and allowed me to experience its beauty, but he has also inspired me with his never-ending enthusiasm for seeking large objectives, which will affect me for the rest of my life regardless of the sector in which I work. Thank you for always being available to assist, for your dedication to meeting deadlines, for your patience, for being both informed and energetic, for all of the scientific discussions, and for everything I have learned from you.

Throughout my Ph.D. studies at ICMUV, I met many wonderful and helpful people who have inspired both my professional and personal lives.

I would like to thank my best colleague, Dr. Hamid Pashaei Adl, for all he has done for me during my Ph.D., including the continuing hard work in the lab with me, data analysis, numerical modeling, and everything else he has done for me. I'd like to thank Prof. Carlos J. Zapata-Rodriguez and his wife, Dr. Mahin Naserpour, not only for teaching me many essential numerical modeling skills but also for their aid, friendliness, and support from the moment I came to Valencia.

A special thanks to all our group members, Dr. Isaac Suarez Alvarez, Dr. Uladzimir Chyrvony, Dr Albert Ferrando Cogollos, Dr. Rafael Abarques Lopez, Dr. Marie Krecmarova, Prof. Juan Francisco Sanchez Royo, Dr. Pablo Perez Boix, Dr. Alejandro Molina Sanchez, Dr. Jose Bosch Bailach, Dr. Raul Ivan Sanchez Alarcon, Dr. Clara Patricia Aranda Alonso, Dr Teresa Ripolles Sanchis, Dr. Marta Vallés-Pelarda, Dr. Cristina Momblona for being kind, for listening to me whenever I wanted to talk, for being there for me whenever I needed help, and for all the laughter and joy we had in a warm environment. A big thanks for all of the students in our group and my officemates to be always present to help me, Dr. Rodolfo Enrique Canet Albiach, Jaume Noguera Gomez , Ismael Fernandez Guillen, Pablo F. Betancur, Jesus Ortiga Fibla, Miriam Mínguez-Avellán, Mahesh Eledath Changarath, Parmenio Boronat Sevilla, Alejandro Martínez Serra. You are such wonderful friends, and I appreciate all the wonderful memories you have given me. Without forgetting the administrative staff and technicians: Maria Angeles Yuste, Amparo Alarcon, David Vie, Antonio Lazaro, Julian Heredero and Juan Vicente Perez , who gave invaluable administrative and technical assistance in the completion of this thesis. I also want to thank all the funding sources from which I have benefited and who have supported the initiatives in which I have participated. "Programa

Santiago Grisolia de la Conselleria d'Educació, Investigació, Cultura i Esport (GRISOLIAP/2018/093), CPI-18-120" and, "Research Fellowship in project (CPI-22-034)."

Lastly, I would want to express my deepest thanks to my parents for their unwavering love, support, and assistance. Sincere gratitude to my sister for always being a friend, helping me to remember what's essential in life, and supporting all of my experiences. Deepest gratitude to my brother, and my nephews for always being there to inspire me and recharge my batteries when I was down and tired and helping me to continue. And thanks to all of my friends who remained by me during this difficult time, constantly providing encouragement and love.

Setatira Gorji

Valencia, June, 2023

Contents

Acknowledgements	V
Abstract	XIII
Resumen en castellano	XVII
0.1 Objetivos:	XIX
0.2 Metodología:	XXI
0.3 Preparaciones de muestras:	XXVI
0.4 Exfoliación mecánica:	XXVIII
0.5 Preparación de muestras para microcavidades de acceso abierto (CsPbBr ₃ NCs & TEA ₂ SnI ₄ microcristales):	XXIX
0.6 Caracterización óptica:	XXIX
0.7 Conclusión:	XXXII
1 State of the art	1
1.1 Introduction	1
1.2 Fundamentals and Physical Background	18
2 Experimental Method	45
2.1 Sample preparation	45
2.2 Optical Characterization	49
2.2.1 Optical microscopy	49

2.2.2	Confocal micro-PL and micro-TRPL	50
2.2.3	Photon correlation (Hanbury Brown and Twiss Setup):	59
2.2.4	Open access Microcavity setup	60
2.3	Scanner micro-PL map at low and room temperature	64
2.4	Transmission Electron Microscopy:	65
2.5	Numerical Methods	66
3	Optical stability of CsPbX₃ (Br, I) perovskite nanocrystal for single photon emission	73
3.1	Introduction and state of the art	74
3.2	Experimental Details and Methods	76
3.3	Results and Discussion	80
3.4	Conclusions	93
4	Donor-acceptor discrete optical emission in 2D perovskites	95
4.1	Introduction	96
4.2	Experimental details	99
4.3	Results	102
4.3.1	Micro-photoluminescence and time decays	102
4.3.2	Donor-Acceptor pair optical emission	108
4.4	Discussion	118
4.5	Conclusions	120
5	Light-Matter interaction and Light mode coupling in an open-access fiber based optical microcavity	123
5.1	Introduction	124
5.2	Experimental Details and Methods	126
5.3	Light-Matter interaction	127
5.4	Light-mode coupling	134

5.4.1	Bragg photons propagating in the photonic structure	135
5.4.2	DBR-based microcavities	136
5.4.3	Interaction of weakly confined cavity modes with propagating Bragg photons	138
5.5	Conclusions	144
6	Conclusions	147
	Appendices	151
A.	List of acronyms	152
B.	Publications	156
B.1	Included in the thesis	156
B.1.1	Papers published in Journals	156
B.1.2	Conferences (posters)	156
B.2	Not included in the thesis	157
B.1.2	Conferences (posters)	159
7	Bibliography	163

Abstract

Materials with perovskite lattices have caught the attention of a large community of researchers worldwide. Their importance arises from their distinctive mechanical and electrical characteristics, which include pyroelectricity and piezoelectricity, dielectric and superconducting properties, significant nonlinear coefficients, and potential electro-optic effects. As a result, this material family is a good candidate for a wide range of applications. Due to all of the various crystallographic variations and chemical diversity, despite the relative simplicity of its crystal structure, ABX_3 , the perovskite lattice encompasses a huge number of compounds, where A is an inorganic or organic bulky cation, B is a metal cation and X the halide anion. Currently, metal halide perovskites with the same crystal structure as that of ABX_3 , have become limelight in the field of optoelectronics and photonics. Within context, all inorganic $CsPbX_3$ (with X = Cl, Br, I) perovskite nanocrystals (PNCs) have more recently emerged as outstanding materials with remarkable optical characteristics, such as high absorption efficiency, a quantum yield of emission exceeding 90% at ambient temperature, an adjustable bandgap based on size and shape tuning, and high nonlinear optical coefficients. This low-cost substitutes, based on (nano)materials synthesized using colloidal chemistry methods enable semi-

conductors to have configurable optical properties that can be engineered during the synthesis. Furthermore, their colloidal nature allows for easy integration into any optical architecture using coating or printing procedures. Another outstanding point of the CsPbX₃ PNCs is the ability to tune their bandgap and, as a result, their light emission spectrum by changing the composition of the halide anion (X): their peak wavelength is observed at around 400 nm (near UV), 510 nm (green), and 680 nm (deep red) for X = Cl, Br, and I, respectively, in addition to the Cl_xBr_yI_{1-x-y} combinations with 0 ≤ x, y ≤ 1. Moreover, light emission of these PNCs in the form of films is characterized by high color purity, with Photoluminescence (PL) Full Width at Half Maximum (FWHM) as low as 20 nm for CsPbBr₃ (green emission) and less than 15 nm for those of CsPbCl₃ (emission in blue violet). Additionally, two-dimensional (2D) van der Waals nanomaterials have attracted considerable attention for potential use in photonic and optoelectronic applications in the nanoscale, due to their outstanding electrical and optical properties, differing from their bulk state. Currently, 2D perovskites belonging to this group of nanomaterials are widely studied for a wide range of optoelectronic applications. The crystal lattice in 2D perovskites is composed of an inorganic octahedral layer sandwiched by long organic cations, resulting in 2D quantum well structures. The general chemical formula for 2D perovskites is R₂A_{n-1}B_nX_{3n+1}, where R₂ is a long organic cation (phenethylammonium, butylammonium, ethylammonium, ...), A is a tiny organic cation (methylammonium (MA), formamidinium (FA), ...), B is a metal inorganic cation (e.g., lead, tin, and so on), and X is a halide inorganic anion (i.e., chloride, bromide, or iodide). 2D perovskites due to their excitonic properties are also promising materials for photonics and nonlinear devices working at room temperature. Nevertheless, strong exci-

tonic effects can reduce the photocurrent characteristics when using thinner perovskites phases. Lead and other hazardous heavy metals, on the other hand, are common in perovskites. As a consequence, lead-free perovskites were developed as a low-cost, non-toxic, earth-abundant material for the next generation of optoelectronic applications. However, recent research has revealed that lead free perovskites have poor ferroelectric properties, which may limit their applications.

In light of these concerns, the purpose of this Ph.D. thesis is to fully indicate the significance of perovskite materials as active materials for quantum photonics, from both fundamentally and an application standpoint. All physical mechanisms responsible for spontaneous emission in PNCs must be explored for the first research objective within that goal. Single PNC samples will be examined first as fundamental building blocks for quantum light sources, from which more complex architectures can be built. Controlling emitted light in single nanocrystals (NCs) and fully characterizing its dependence on excitation fluency, capping ligands and passivation to have a stable emission, and determining the decay time of these single NCs are all important steps to this objective. Once the ideal conditions for PNCs are developed, they can be used as quantum light sources, with the quality of the light being evaluated the second order photon correlation function. The next landmark will be to investigate two-dimensional (2D) perovskite, a type of 2D van der Waals nanomaterial, for its potential use in photonic and optoelectronic applications at the nanoscale. Optimizing the conditions for mechanical exfoliation of bulk crystals of two different phases of 2D perovskites with the lowest quantum well thickness of $n=1$ and $n=2$ to achieve sufficiently thin 2D nanoflakes is an important step towards achieving this goal. Once the optimal conditions for these two different phases of 2D per-

ovskites with $n=1$ and $n=2$ are established, their optical properties can be investigated at low temperatures using a confocal micro-Photoluminescence (μ -PL) spectroscopy system. The final objective is focused on the incorporation of perovskite materials in an open access fiber-based microcavity. The cavity specific geometry provides strong optical confinement of the modes. The open style of the fiber cavity allows for independent movement of the fiber mirror, allowing for in-situ tuning of the cavity resonance, and typically over a wider spectral range, which this tuning is not possible in monolithic microcavity. As a result, controlling the various parts of this cavity setup, such as glue the fiber mirror to a fiber holder, mounting piezoelectric motors, and so on, as well as properly understanding the possible light-matter interactions and Light mode coupling based on numerical models, is a significant step toward achieving this objective. The final step will be to deposit different perovskite materials (for example, the aforementioned PNCs) in the microcavity to investigate light-mater interaction and Light mode coupling. In light of the above-written results, this Ph.D. thesis suggests that perovskite materials are promising candidates for opening the way for a new generation of quantum light sources and their applications.

Resumen en castellano

Los materiales con estructura de tipo Perovskita han atraído la atención de una amplia comunidad de investigadores en todo el mundo. Su importancia radica en sus particulares características mecánicas y eléctricas, como la piroelectricidad y la piezoelectricidad, sus interesantes propiedades dieléctricas y superconductoras, o la aparición de grandes coeficientes no lineales que dan lugar a interesantes efectos electroópticos. Como resultado, esta familia de materiales es una destacada candidata para desarrollar una amplia gama de aplicaciones en el campo de los dispositivos optoelectrónicos. A pesar de la relativa simplicidad de su estructura cristalina los materiales del tipo perovskita incluyen una enorme variedad de compuestos, debido a todas las posibles variaciones cristalográficas y a su diversidad química. Actualmente, los haluros metálicos de perovskita del tipo ABX_3 , han cobrado protagonismo en los campos de la optoelectrónica y la fotónica. A es un catión voluminoso inorgánico u orgánico, B es un catión metálico como Pb^{2+} o Sn^{2+} y X el anión haluro. Particularmente, los nanocristales de perovskita (PNC) inorgánicos $CsPbX_3$ (con $X = Cl, Br, I$) son materiales excepcionales que presentan propiedades ópticas de alto interés, como una alta eficiencia de absorción, un rendimiento cuántico de emisión superior al 90% a temperatura ambiente, una banda prohibida sintonizable en función del tamaño y la forma de los nanocristales, o altos coeficientes ópticos no

lineales. Esta alternativa de bajo coste, basada en la ingeniería de nanomateriales sintetizados mediante técnicas de química coloidal, permite que los semiconductores tengan propiedades ópticas configurables que pueden diseñarse durante la síntesis. Además, su naturaleza coloidal permite integrarlos fácilmente en cualquier arquitectura óptica mediante técnicas de recubrimiento o impresión. Otro punto destacable de los PNCs CsPbX_3 es la sintonización de su banda prohibida, y por consiguiente de su espectro de emisión de luz, modificando la composición del anión haluro (X): su longitud de onda pico se observa en torno a 400 nm (UV cercano), 510 nm (verde) y 680 nm (rojo intenso) para $X = \text{Cl}, \text{Br}$ e I , respectivamente, además de las combinaciones $\text{Cl}_x\text{Br}_y\text{I}_{1-x-y}$ con $0 \leq x, y \leq 1$. La emisión de luz de estos PNC se caracteriza por una gran pureza de color, con una anchura de la PL (FWHM) de escasos 20 nm para los de CsPbBr_3 (emisión en verde) y menos de 15 nm para los de CsPbCl_3 (emisión en azul violeta) a temperatura ambiente.

Por otra parte, los nanomateriales van der Waals bidimensionales (2D) reciben una gran atención por su capacidad de integración en aplicaciones fotónicas y optoelectrónicas que requieren nanoestructuración. Sus extraordinarias propiedades eléctricas y ópticas, difieren de las propiedades de los mismos materiales masivos. En la actualidad, las perovskitas bidimensionales (2D) pertenecientes a este grupo de nanomateriales se estudian ampliamente para ser incluidas como emisores ópticos en una amplia gama de aplicaciones optoelectrónicas. La red cristalina de las perovskitas 2D se compone de una capa octaédrica inorgánica intercalada por largos cationes orgánicos, lo que da lugar a estructuras de pozo cuántico 2D. La fórmula química general de las perovskitas 2D es $\text{R}_2\text{A}_{n-1}\text{B}_n\text{X}_{3n+1}$, donde R_2 es un catión orgánico largo (fenetilamonio, butilamonio, etilamonio, ...), A es un

cación orgánico diminuto (metilamonio (MA), formamidinio (FA), ...), B es un catión inorgánico metálico (por ejemplo, plomo, estaño, etc.), y X es un anión inorgánico haluro (por ejemplo, cloruro, bromuro o yoduro). Las perovskitas 2D, debido a sus propiedades excitónicas, también son materiales muy interesantes para las aplicaciones en fotónica y dispositivos no lineales operados a temperatura ambiente. Sin embargo, los fuertes efectos excitónicos pueden reducir las características de la fotocorriente cuando se utilizan fases de perovskitas más delgadas.

Por último, conviene señalar que el plomo y otros metales pesados peligrosos son habituales en las perovskitas. Por ello, las perovskitas sin plomo vienen desarrollándose como un material de bajo coste, no tóxico y de alta abundancia que puede ser clave para la próxima generación de aplicaciones optoelectrónicas. Sin embargo, investigaciones recientes revelan que este tipo de perovskita no-tóxica posee problemas tanto desde el punto de vista de su estabilidad, como del posible detrimento de sus altas prestaciones, como sucede con la reducción de la ferroelectricidad, lo que puede limitar el desarrollo de aplicaciones y dispositivos.

0.1 Objetivos:

A la luz de estas consideraciones, el objetivo general de esta tesis doctoral es estudiar y analizar la importancia de los materiales de perovskita como medios activos para la fotónica y la optoelectrónica, y más particularmente para su inclusión en las tecnologías cuántica, tanto desde un punto de vista fundamental como de aplicación. Para ello, se utilizan las extraordinarias propiedades ópticas de las perovskitas 2D y los NCs de perovskita de haluro de plomo (LHPs) para analizar diferentes funcionalidades, como la emisión de fotones uno a uno, la emisión óptica discreta de pares aceptor-dador o

la interacción de la emisión de perovskitas 2D con resonadores y cavidades ópticas. De este modo, podemos dividir los objetivos principales en tres secundarios:

En primer lugar, hemos analizado distintos mecanismos físicos responsables de la emisión espontánea en las PNC. Se han examinado muestras PNC de perovskita aisladas, como materiales fundamentales para diseñar fuentes de luz cuántica, a partir de los cuales se pueden construir arquitecturas más complejas. El control de la luz emitida en PNCs aisladas y la caracterización completa de su dependencia con los parámetros de excitación óptica, los ligandos de recubrimiento y la pasivación para tener una emisión estable, como la medida de los tiempos de vida de las transiciones ópticas presentes en estas PNCs aisladas, son pasos importantes hacia este objetivo. Una vez establecidas las condiciones óptimas que ofrecen la mejor estabilidad y calidad óptica, estas nanoestructuras semiconductoras podrán utilizarse como fuentes de luz cuántica, evaluándose la calidad de la luz mediante una función de correlación de fotones de segundo orden.

El segundo hito propuesto en esta tesis consiste en investigar la emisión de perovskitas bidimensional (2D), un tipo de nanomaterial van der Waals 2D. Este análisis está motivado por su posible uso en aplicaciones fotónicas y optoelectrónicas en la nanoescala. Un paso importante en la consecución de este objetivo es la optimización de las condiciones para la exfoliación mecánica de cristales masivos pertenecientes a distintas fases de perovskitas 2D, clasificadas en función del grosor de pozo cuántico inorgánico. Una vez establecidas las condiciones óptimas para estas dos fases diferentes de perovskitas 2D con $n=1$ y $n=2$, se pueden investigar sus propiedades ópticas a bajas temperaturas utilizando un sistema de espectroscopia confocal micro-PL.

Como tercer objetivo se propone la incorporación de materiales de perovskita en microcavidades de acceso abierto diseñadas en fibra óptica. La geometría específica de las cavidades proporciona un fuerte confinamiento óptico de los modos. El acceso abierto a la cavidad de fibra óptica permite el movimiento independiente y relativo entre los espejos que forman la cavidad, lo que permite el ajuste in-situ de la resonancia de la cavidad sin la reducción en el acoplamiento que se observa en las alternativas de cavidades monolíticas. Típicamente, el rango espectral de la cavidad es más amplio. En consecuencia, el control de las distintas partes ópticas y mecánicas que forman y caracterizan estas cavidades, así como la comprensión adecuada de las posibles acoplamiento de modos de luz y luz-materia interacciones a partir de modelos y simulaciones numéricas, son pasos destacados hacia la consecución de este tercer objetivo particular. Finalmente, los resultados de los análisis numéricos se contrastarán con medidas experimentales del acoplamiento luz-materia entre los modos de la cavidad y la emisión de distintos materiales de Perovskitas.

0.2 Metodología:

Método de inyección en caliente para la síntesis de nanocristales:

Se sintetizaron NCs de perovskita de haluro de plomo (LHP) siguiendo el método de inyección en caliente comúnmente utilizado para preparar NCs de compuestos semiconductores II-VI, IV- VI, y III-V. Se obtuvieron nanocubos (NC) coloidales de CsPbX_3 ($X = \text{Cl, Br, I}$) con un PLQY cercano al 90% a temperatura ambiente y una amplia gama de colores para ser utilizados como materiales activos. En resumen, el método de inyección

en caliente consiste en la inyección de precursores de calcogenuros (S, Se, Bis(trimetilsilil)sulfuro, etc.), precursores metálicos (haluros metálicos, en el caso de los PNC) y ligandos específicos de alto poder de coordinación (oleilamina, ácido oleico, trioctilfosfina, zwitteriónico, etc.) en otra solución de coordinación caliente con precursores metalorgánicos en un disolvente de alto punto de ebullición (octadeceno). Los matraces se mantienen bajo una atmósfera inerte de N_2 y a una temperatura relativamente baja, inferior a 200 - 300 °C. Una vez inyectados los precursores, se inicia la reacción química y se generan las primeras moléculas de monómero. Según el modelo clásico de LaMer, la concentración de monómeros se sobresaturará con el tiempo, dando lugar a la formación de centros de nucleación. Las semillas formadas seguirán aumentando en número mientras que la población de monómeros disponibles disminuye constantemente hasta que se alcanza un punto crítico. En este punto, casi no se produce nucleación debido a la baja concentración de monómeros. Una vez formados los núcleos, actuarán como semilla para el crecimiento de los cristales; se formarán nanocristales más grandes por coalescencia de los ya existentes, tal y como describe un proceso conocido como maduración de Ostwald. Dado que los procesos de nucleación de las semillas y de crecimiento cristalino están acoplados, ambas etapas desempeñan un papel a la hora de decidir el tamaño medio final y la distribución de tamaños de las NC. Existen muchas estrategias para controlar el proceso de crecimiento y la distribución del tamaño de los nanocristales. Los parámetros más importantes son la temperatura de reacción, el tiempo de reacción, la concentración de precursores y la concentración de disolventes de coordinación. Durante las etapas finales de la síntesis de NCs, las NCs resultantes se recubren con una capa de moléculas tensioactivas (ligandos) que proporcionan estabilidad coloidal y pasivan los

defectos superficiales. Sin embargo, la solución de NC sintetizada también contiene disolvente de alto punto de ebullición, subproductos de la reacción, precursores que no han reaccionado y ligandos. Así pues, la solución bruta debe purificarse con una estrategia de disolventes polares/no polares para eliminar los residuos químicos y mejorar la distribución final de tamaños y las propiedades reológicas generales de la solución final. Normalmente, el disolvente de alto punto de ebullición se sustituye por disolventes de bajo peso molecular, como el n-hexano o el tolueno. La solución coloidal final de NC, lista para el colado de la película, suele denominarse nanotinta.

CsPbX₃ (X=Br, I) Nanocristales con Oleilamina, ligandos de ácido oleico:

Las CsPbX₃ PNCs se sintetizaron siguiendo el método de inyección en caliente con algunas modificaciones. Todos los reactivos se utilizaron tal como se recibieron, sin ningún proceso de purificación adicional. Después de preparar la solución de Cs-oleato, se añadieron 0,41 g de Cs₂ CO₃ (Sigma-Aldrich, 99,9%), 1,25 mL de ácido oleico (OA, Sigma-Aldrich, 90%) y 20 mL de 1-octadeceno (1-ODE, Sigma-Aldrich, 90%) en un matraz de tres bocas de 50 mL a 120 °C en vacío durante 1 h bajo agitación constante. Después, la mezcla se purgó con N₂ y se calentó a 150 °C, disolviendo completamente el Cs₂ CO₃. La solución se almacenó bajo N₂, manteniendo la temperatura a 100 °C para evitar la oxidación del Cs-oleato.

Para la síntesis de CsPbBr₃, y CsPbI₃ NPs, se mezclaron 0,69 g de PbBr₂ (ABCR, 99,999%), 0,87 g de PbI₂ (TCI, 99,99%), con 50 mL de 1-ODE en un matraz de tres bocas de 100 mL. La mezcla se calentó a 120 °C en vacío durante 1 h con agitación constante. A continuación, se añadieron por separado 5 mL de OA y oleilamina (OLA, Sigma-Aldrich,

98 %) al matraz bajo N_2 , y la mezcla se calentó rápidamente a $170\text{ }^\circ\text{C}$. Simultáneamente, se añadieron 4 mL de solución de Cs-oleato a la mezcla y ésta se sumergió en un baño de hielo durante 5 s para apagar la reacción. Para realizar el proceso de aislamiento de las PNCs, las soluciones coloidales se centrifugaron a 4700 rpm durante 10 min. A continuación, se separaron los pellets de NCs tras desechar el sobrenadante y se volvieron a dispersar en Tolueno para concentrar las PNCs a 50 mg mL^{-1} .

CsPbBr₃ Nanocristales con ligandos zwitteriónicos:

La síntesis de CsPbBr₃ PNCs mediante la adición de ligandos zwitteriónicos se realizó mezclando cantidades estequiométricas de Cs-oleato, Pb-oleato, TOP-Br₂ y sulfobetaína basada en N- dodecil-N,N-dimetil-3-amonio-1-propanosulfonato (ASC12), con algunas modificaciones. Para preparar la solución de Cs-oleato (0,4 M), se mezclaron 1,628 g de Cs₂ CO₃ (5 mmol), 5 mL de ácido oleico (OA, 16 mmol) y 20 mL de 1-octadeceno (1-ODE) en un matraz de tres bocas bajo vacío al calentar a $120\text{ }^\circ\text{C}$, hasta la finalización de la evolución del gas. Por otra parte, el Pb-oleato (0,5 M) se preparó mezclando 4,61 g de acetato de plomo (II) trihidratado (12 mmol), 7,6 mL de OA (24 mmol) y 16,4 mL de ODE en un matraz de tres bocas bajo vacío al calentar a $120\text{ }^\circ\text{C}$, hasta la evaporación completa del ácido acético y el agua. Simultáneamente, se preparó la disolución de TOP-Br₂ (0,5 M) combinando 6 mL de trioctilfosfina (TOP, 13 mmol) 9,4 mL de tolueno y mesitileno, y 0,6 mL de bromo (11,5 mmol) bajo purga de N_2 .

En esta etapa, se mezclaron 5 mL del Pb-oleato preparado (0,0025 mol), 4 mL de Cs-oleato (0,0016 mol), 0,336 g de ASC12 (1 mmol) y 10 mL de 1-ODE en un matraz de tres bocas de 50 mL y se calentó a $120\text{ }^\circ\text{C}$ en vacío. A continuación, se purgó la reacción de mezcla con N_2 y se aumentó la

temperatura hasta alcanzar 180 °C. Aquí, se inyectaron rápidamente 5 mL de TOP- Br₂ (0,0025 mol), y la reacción se apagó en un baño de hielo. Para aislar el producto final, las PNC se centrifugaron a 5000 durante 5 min con 60 mL de acetona. Los pellets de PNCs se separaron del sobrenadante, se redispersaron con tolueno a 50 mgmL⁻¹.

TEA₂SnI₄ microcristales:

Síntesis de SnI₂ - Solución precursora TOP

En este procedimiento típico, se mezclaron 1 mL de 2-etilhexanoato de estaño (II) y 2 mL de trioctilfosfina (TOP) en un matraz de fondo redondo de 25 mL y se desgasificaron en vacío bajo agitación magnética durante 1 hora a temperatura ambiente. Después se cambió la atmósfera por flujo de nitrógeno y se inyectó 1 mL de trimetil silil yoduro (TMSI) en una relación molar de TMSI/Sn²⁺ = 2.

Síntesis de microplacas TEA₂SnI₄

En un matraz de fondo redondo de 3 bocas, se desgasificaron 20 mL de mesitileno y 1 mL de ácido oleico a temperatura ambiente durante 1 hora en vacío. A continuación, se inyectó la solución de SnI₂ - TOP en el matraz de reacción bajo atmósfera de nitrógeno y se elevó la temperatura a 160 °C. Por último, se inyectaron 0,11 mL de 2-tiofenetilamina (TEA) y, tras 5 segundos, se enfrió la mezcla de reacción hasta temperatura ambiente. Por último, se inyectaron 0,11 mL de 2-tiofeneetilamina (TEA) y después de 5 segundos, la mezcla de reacción se enfrió en un baño de hielo hasta temperatura ambiente. Las microplacas TEA₂SnI₄ se aislaron por centrifugación y se lavaron con n-hexano tres veces. Las microplacas de TEA₂SnI₄

se volvieron a dispersar en 3 mL de n-octano y se almacenaron en una guantera.

0.3 Preparaciones de muestras:

Preparación de NCs aisladas de CsPbX_3 ($\text{X}=\text{Br}, \text{I}$) dispersas sobre sustratos de SiO_2 :

Nuestra intención en este estudio es medir la emisión de luz de las CPN aisladas. Con este objetivo, preparamos muestras dispersadas sobre un sustrato. Para la preparación de las muestras se utilizó una oblea comercial de Si recubierta con una película de SiO_2 de 285 nm de espesor, la oblea se limpia secuencialmente con etanol, isopropanol y acetona. A continuación, la deposición de PNCs se llevó a cabo mediante recubrimiento por inmersión utilizando una suspensión coloidal de PNCs con una concentración controlada en Tolueno, con el fin de definir una interdistancia de partículas mayor que nuestra resolución óptica.

Preparación de muestras de perovskita 2D:

Síntesis de PEA_2PbI_4 ($n=1$): Solución A. Se disolvió polvo de PbO (1116 mg, 5 mmol) en una mezcla de solución acuosa de HI al 57% p/p en peso (5,0 mL, 38 mmol) y H_3PO_2 acuoso al 50% (0,85 mL, 7,75 mmol) calentando hasta ebullición bajo agitación enérgica durante unos 10 min. Entonces pudo observarse la formación de una solución de color amarillo brillante. **Solución B.** En un vaso de precipitados separado, se neutralizó $\text{C}_6\text{H}_5\text{CH}_2\text{CH}_2\text{NH}_2$ (fenetilamina, PEA) (628 μl , 5 mmol) con HI 57% p/p (2,5 mL, 19 mmol) en un baño de hielo, obteniéndose una solución clara de

color amarillo pálido. Si se observa un precipitado sólido o la formación de una suspensión, se puede calentar ligeramente hasta que se haya disuelto. Una vez preparadas ambas soluciones, se procede a la adición lenta de la solución B a la solución A. Una adición rápida podría producir un precipitado, que se disolvería posteriormente al calentar la solución combinada hasta ebullición. Tras mantener la solución en ebullición durante 10 minutos, se interrumpió la agitación y se dejó enfriar a temperatura ambiente. Al alcanzar dicha temperatura se produjo la cristalización de placas rectangulares de color naranja. El proceso de cristalización se completó al cabo de 1 hora. Los cristales se aislaron por filtración de succión y se secaron completamente en un ambiente de presión reducida. Los cristales individuales obtenidos se lavaron con éter dietílico frío.

Síntesis de $\text{PEA}_2\text{MAPb}_2\text{I}_7$ (n=2): Solución A. Se disolvió polvo de PbO (1116 mg, 5 mmol) en una mezcla de solución acuosa de HI al 57 % p/p en peso (5,0 mL, 38 mmol) y H_3PO_2 acuoso al 50 % (0,85 mL, 7,75 mmol) calentando hasta ebullición bajo agitación energética durante unos 5 min y formando una solución amarilla. A continuación, se añadió muy lentamente $\text{CH}_3\text{NH}_3\text{Cl}$ en polvo (169 mg, 2,5 mmol) a la solución amarilla caliente, formándose un precipitado negro que se redisolvió rápidamente bajo agitación para conseguir una solución clara de color amarillo brillante. **Solución B.** En un vaso de precipitados separado, $\text{C}_6\text{H}_5\text{CH}_2\text{CH}_2\text{NH}_2$ (PEA) (880 μl , 7 mmol) se neutralizó con HI 57 % p/p p/p (2,5 mL, 19 mmol) en un baño de hielo, obteniéndose una solución clara de color amarillo pálido. La adición de la solución de PEAI a la solución de PbI_2 produjo inicialmente un precipitado negro, que se disolvió calentando la solución combinada hasta ebullición. Tras interrumpir la agitación, la solución se enfrió a temperatura ambiente y empezaron a aparecer cristales de color rojo cereza. La

precipitación se consideró completa tras ~ 1 h. Los cristales se aislaron por filtración de succión y se secaron a fondo a presión reducida. El material se lavó con éter dietílico frío.

0.4 Exfoliación mecánica:

La exfoliación mecánica es una de las mejores técnicas para obtener películas finas de hasta una monocapa (ML) de materiales exfoliables. Se trata de una técnica descendente, basada en la diferencia de fuerza entre los débiles enlaces van der Waals (vdW) entre capas y los fuertes enlaces covalentes intracapa en la estructura laminar. En este proceso, un cristal estratificado masivo recién escindido (perovskita 2D en nuestro caso) se deposita sobre una cinta scotch o adhesiva y se despega suavemente varias veces de la cinta, doblándose repetidamente contra sí mismo. Debido a los enlaces vdW más débiles entre capas, en cada exfoliación el material pelado separado de la fuente masiva será más delgado, obteniéndose finalmente hasta MLs del material original. Cuantas más veces se exfolie el material, las nanohojas de perovskita 2D obtenidas serán más delgadas, a costa de perder tamaño lateral de la nanohoja final. No existe una receta para el número ideal de veces o de la presión a aplicar en cada exfoliación; depende del material exfoliado. Se utilizó Nitto Tape azul para minimizar la cantidad de restos de adhesivo en las nanohojas exfoliadas. Por último, una vez exfoliado el material en la cinta, se realizará la última exfoliación entre la cinta y el sustrato de destino para transferir o reexfoliar aleatoriamente las nanohojas de la cinta al sustrato.

0.5 Preparación de muestras para microcavidades de acceso abierto (CsPbBr₃ NCs & TEA₂SnI₄ microcristales):

El objetivo en este caso es acoplar la emisión PL de los materiales de perovskita a los modos de cavidad. Para lograr este objetivo, depositamos NCs de CsPbBr₃ y microcristales de TEA₂SnI₄ a concentraciones optimizadas sobre el DBR planar, dando lugar a una monocapa uniforme de NCs y microcristales más o menos aislados. El DBR planar se limpia con etanol, isopropanol y acetona antes de depositar los materiales. A continuación, utilizando un método de recubrimiento por centrifugación a 3000 rpm durante 30 segundos, se depositaron materiales de perovskita con una concentración optimizada (con una dilución de tres órdenes de magnitud) sobre el espejo DBR planar.

0.6 Caracterización óptica:

Espectroscopia óptica y microscopia óptica confocal:

Todas las mediciones a baja temperatura se llevaron a cabo utilizando una configuración μ -PL estándar, con las muestras colocadas en el dedo frío de un criostato de ciclo cerrado de bajas vibraciones (AttoDRY800 de Attocube AG). Se utilizó un láser de excitación de onda continua (pulsada) con una longitud de onda de $\lambda=405$ nm (450 nm) para excitar la muestra, para obtener los espectros de μ -PL (trazas de TRPL – Fotoluminiscencia resuelta en tiempo). El estenope confocal queda definido por el núcleo de fibras ópticas monomodo utilizadas para recoger la emisión óptica. La excitación

y la detección se llevaron a cabo utilizando un objetivo de microscopio 50 X de larga distancia de trabajo y una apertura numérica de $NA = 0,42$, que se colocó fuera del criostato. La reflexión laser de la muestra a se filtró usando un filtro pasa larga- La señal óptica recogida por la fibra se dirigió a la entrada de un monocromador doble de 0,3 m de distancia focal (Acton SP-300i de Princeton Instruments). La señal difractada por las redes de Bragg se detectó con una cámara CCD de Si refrigerada (Newton EMCCD de ANDOR) para registrar los espectros μ -PL, y un detector de fotodiodo de avalancha monofotónico de silicio (de Micro Photon Devices) conectado a una tarjeta electrónica contaje de fotones para correlacionar coincidencias en el tiempo (TCC900 de Edinburgh Instruments) para las medidas μ -TRPL y de correlación de fotones.

Correlación de fotones (interferometría Hanbury Brown y Twiss):

Para medir y clasificar experimentalmente las distribuciones temporales de fotones, debemos disponer de algún modo de registrar los tiempos de llegada de los fotones emitidos. La técnica de interferometría de Hanbury Brown y Twiss (HBT) es una técnica sencilla y robusta para medir las estadísticas de fotones mediante el análisis de coincidencias. Esta técnica emplea un divisor de haz 50/50 para dividir el flujo de fotones en los dos brazos de salida del divisor de haz, que se hacen dirigir hacia dos detectores de fotones (en este caso Fotodiodos de Avalancha, APDs) separados que funcionan en el modo de recuento de fotones. De esta forma la coincidencia de fotones se puede medir sin un deadtime relativo entre la medida de cada detector. La medida de coincidencia se realiza mediante una tarjeta de contaje de pulsos, o mediante un etiquetado temporal de puslos. Usando una técnica

de TCSPC (Time Correlated Single Photon Counting), uno de los canales activa un temporizador, que se detiene con la medida en el segundo canal. De esta forma se puede medir la coincidencia relativa al tiempo entre ambos eventos (start y stop). El tiempo de retardo de las coincidencias proporciona un valor relativo temporal, cuya resolución viene determinada por la propia respuesta temporal de los detectores APD y el jitter electrónico, limitando por tanto la ventana mínima de detección y la precisión temporal de la medida de coincidencia. En las técnicas de etiquetado temporal la medida de coincidencia se reconstruye como proceso postmedida. Para extraer información útil de esta medición mediante la función de correlación de segundo orden $g^{(2)}(0)$, se comparan los recuentos de coincidencias en para retraso nulo ($\Delta t=0$) respecto al nivel de coincidencia descorrelacionadas (i.e., a retrasos muy largos comparados con el tiempo de emisión del sistema ($\Delta t \rightarrow \pm\infty$)).

Mapa de microfotoluminiscencia (mapa μ -PL):

Para desarrollar el mapa de μ -PL utilizamos el software libre Qudi, que es un conjunto de sistemas generales, modulares y multioperativos escrito en Python 3 para controlar experimentos de laboratorio. Proporciona un entorno estructurado mediante la separación de la funcionalidad en capas de abstracción de hardware, lógica de experimentos e interfaz de usuario. El conjunto de características básicas comprende una interfaz gráfica de usuario, visualización de datos en directo, ejecución distribuida en redes, creación rápida de prototipos mediante cuadernos Jupyter, gestión de la configuración y registro de datos. La colección de la señal de μ -PL se llevó a cabo utilizando un microscopio confocal de barrido basado en fibra, con las muestras colocadas en un criostato de ciclo cerrado sin vibraciones (AttoDRY800

de Attocube AG). El rango máximo de barrido de un piezoeléctrico se reduce con la temperatura desde $50\ \mu\text{m}$ a temperatura ambiente hasta $\sim 30\ \mu\text{m}$, a bajas temperaturas (4K). En nuestro estudio, realizar un mapa completo de $\mu\text{-PL}$ de una muestra es muy útil antes de comenzar las mediciones puntuales; por ejemplo, al estudiar el $\mu\text{-PL}$ de NCs de perovskita individuales, el mapeo ayuda a reconocer cubos individuales aislados. En el caso de monocapas 2D, también es útil para estudiar la emisión PL no uniforme debida a la morfología de la muestra.

0.7 Conclusión:

Teniendo en cuenta los resultados anteriores, esta tesis doctoral concluye que los materiales de perovskita son candidatos prometedores para abrir el camino hacia una nueva generación de aplicaciones y dispositivos fotónicos y cuánticos. El objetivo principal de esta tesis doctoral se ha centrado en la incorporación de materiales de perovskita que emiten en las longitudes de onda visibles en aplicaciones fotónicas y cuánticas. En particular, la implementación de las propiedades ópticas destacadas de los NCs LHPs 2D y coloidales para aportar diferentes funcionalidades, tales como caracterización de la emisión de fotones uno a uno, la emisión óptica de pares aceptador discretos, como la interacción luz-materia y entre modos ópticos por medio del control de cavidades ópticas abiertas, en diversas implementaciones fotónicas y cuánticas. La mayoría de ellas se estudiaron utilizando CsPbX_3 PNCs, perovskitas 2D y sin plomo y los resultados más importantes se presentan en los párrafos siguientes:

Estabilidad óptica del nanocrystal de perovskita CsPbX₃ (X=Br, I) para la emisión de fotón único:

En el análisis de este capítulo hemos utilizado espectroscopia criogénica de μ -PL y μ -TRPL para examinar PNCs individuales con dos ligandos de recubrimiento diferentes, deduciendo un ancho de línea homogéneo medio de las transiciones ópticas excitónicas en muestras preparadas para ambos casos. En comparación con los ligandos OLA/OA típicos con anchos de línea medios de $\sim 2,35$ meV, los anchos de línea homogéneos de la emisión óptica de NCs CsPbBr₃ individuales con ligandos ZW muestran un estrechamiento significativo, y una mayor estabilidad, reduciendo tanto los efectos de parpadeo óptico y de difusión espectral. El valor medio del ancho de línea PL de las NCs con los ligandos de ZW, con un valor medio de ~ 250 μ eV, es el valor más pequeño registrado hasta ahora en la bibliografía para las NCs de CsPbBr₃. Además, basándonos en las medidas de μ -TRPL, se observó un tiempo de decaimiento ligeramente más largo para las NCs simples de CsPbBr₃ con ligandos ZW, lo que las hace mejores candidatas para ser integradas como fuentes de luz cuántica que las que usan ligandos del tipo OLA/OA. Sin embargo, en el caso de las NCs de CsPbI₃, esta estrategia (utilizar ligandos ZW en lugar de OLA/OA) no obtuvo los mismos resultados, y los ligandos tradicionales OLA/OA siguieron siendo los mejores candidatos.

Emisión óptica discreta donante-aceptor en perovskitas 2D:

En este capítulo, nuestra observación de las líneas de μ -PL estrechas y discretas asociadas a las transiciones de pares dador-aceptor (DAP) com-

plementa algunas observaciones recientes sobre este tipo de complejos de carga, como la sintonización de la energía de enlace del excitón mediante interacciones dador-aceptor o el rendimiento de la emisión de fotones uno a uno emitidos por la recombinación DAP en hBN 2D. Mediante espectroscopía HR-XPS, demostramos que los dos componentes orgánicos presentes en la muestra de fase $n=2$ promueven la formación de los defectos responsables de la transición DAP. En concreto, la coexistencia del catión MA^+ , que da lugar a la segregación de Pb, y del catión PEA_2 , que provoca la distorsión de la lámina de la red inorgánica, podría favorecer el desplazamiento e intercambio de átomos de MA^+ y Pb, de ahí la formación de los estados aceptor de MA_{Pb} y dador de Pb_{MA} . El uso de un modelo sencillo de corrección coulombiana predice la presencia de estados DAP de baja densidad en el rango espectral cercano a la emisión de las transiciones excitónicas, y, por tanto, tanto la baja DOS como la gran separación de la función de onda donante-aceptora explican las transiciones ópticas estrechas DAP medidas con tiempos de vida de varios nanosegundos. Para proporcionar una aplicación futura basada en el control de estos estados, deberían diseñarse rutas específicas de preparación de muestras para controlar y optimizar la población de los estados DAP, su como su localización o aislamiento. Debido a sus características y sus propiedades espectrales, junto con su alto brillo de fotoluminiscencia, el estado DAP en Perovskitas 2D representa un estado electrónico interesante a tener en cuenta para el desarrollo del campo emergente de las tecnologías cuánticas, como la polaritónica cuántica o la óptica cuántica no lineal.

Interacción Luz-Materia y acoplamiento de modos de luz en una microcavidades óptica basada en fibra de acceso abierto:

En esta última parte de la tesis, se ha estudiado el acoplamiento de los modos de una microcavidad basada en fibra de acceso abierto y la emisión de distintas muestras de Perovskitas. Tras montar la microcavidad y controlar varios aspectos de su configuración y sus propiedades, como obtener control en el pegado de los espejos DBR cóncavo depositados sobre los extremos de la fibra y caracterizar las propiedades fundamentales de los modos estacionarios, se depositaron NCs de CsPbBr_3 en el interior de la cavidad óptica, estudiando la interacción de los modos ópticos fundamentales con la emisión de las NCs a temperatura ambiente. La geometría específica de las cavidades proporciona un fuerte confinamiento óptico de los modos, y su estilo abierto permite el movimiento independiente del espejo de la fibra, permitiendo el ajuste in situ de la resonancia de la cavidad sin la reducción del acoplamiento. Además, la configuración se modeló numéricamente para comprender con precisión las posibles interacción luz-materia y acoplamiento de modos de luz entre las ondas de Bloch contenidas en los espejos DBR y los modos parcialmente confinados de la microcavidad localizados fuera de su banda prohibida, que observamos experimentalmente durante la adquisición de las medidas de emisión óptica. Los resultados de la simulación revelaron que las ondas Bloch en los DBR y los modos parcialmente confinados de la microcavidad pueden acoplarse fuertemente incluso en el caso de no depositar material emisor óptico. Sin embargo, la fuerza de este acoplamiento entre modos ópticos puede modificarse depositando materiales en el interior de la cavidad.

Para recapitular, esta tesis muestra que los materiales de perovskita son

candidatos prometedores para futuras aplicaciones. El PLQY de las LHP se sitúa en torno al 100 %, lo que las convierte en buenas candidatas para todo tipo de tecnologías fotónicas y optoelectrónicas, incluyendo el desarrollo de emisores de fotones uno a uno en el seno de las actuales tecnologías cuánticas. Además, nuestro trabajo en perovskitas 2D muestra que la investigación sobre DAP en materiales 2D representa un campo en crecimiento con un alto potencial, y nuestra observación de las líneas PL estrechas y discretas asociadas a las transiciones DAP se añade a las propiedades recientemente reportadas de DAP en materiales 2D. Además, revelar la Acoplamiento en modo luz simultáneamente con la interacción luz-materia en una microcavidad de acceso abierto es muy beneficioso para el futuro desarrollo de microcavidades complejas acopladas para aplicaciones fotónicas cuánticas basadas en el control de estados de luz, como puede ser inicializadores de qubits o sistemas de sensado cuántico en el campo de la acusto-óptica y la optomecánica.

Chapter 1

State of the art

1.1 Introduction

Materials with perovskite lattices have caught the attention of a large community of researchers worldwide. Their significance stems from their unique mechanical and electrical properties, which include pyroelectricity and piezoelectricity [1]; dielectric and superconducting properties [2]; large nonlinear coefficients [3]; and potential electro-optic effects [4]. As a result, this material family is an ideal candidate for a wide range of applications [1], such as photodetectors [5,6], light emitting diodes [7,8], and a single-photon source (a "quantum emitter") that is required for quantum-information and quantum-communication techniques [9–11]. Despite the relative simplicity of its crystal structure, ABX_3 , where, A is an inorganic or organic bulky cation, B is a metal cation and X the halide anion, the perovskite lattice contains a vast array of compounds [12] because of all of the possible crystallographic variations and chemical variety. Lead Halid Perovskites (LHPs) have the general formula of $APbX_3$ (Figure 1.1 displays a rendered illustration of the LHP unit cell), where A is an organic or inorganic monovalent

cation and X is the Cl, Br, or I anion. Methylammonium (MA) and Formamidinium (FA) are among the most common monovalent organic cations currently being used in the synthesis of LHPs. If the organic cation is replaced by an inorganic cation, a fully inorganic LHP is formed. In terms of available size inside the perovskite structure, the cesium cation (Cs) is a suitable choice, forming the cesium LHP family (CsPbX_3). There is a higher stability under thermal and humidity attacks in comparison with organic cation-based hybrids is offered by the all-inorganic CsPbBr_3 perovskites [13].

Additionally, two-dimensional (2D) van der Waals nanomaterials have attracted considerable attention for potential use in photonic and optoelectronic applications in the nanoscale, due to their outstanding electrical and optical properties, differing from their bulk state. Currently, 2D perovskite belonging to this group of nanomaterials is widely studied for a wide range of optoelectronic applications, due to strong quantum confinement and the sizable band gap in these materials [14–16]. The crystal lattice in 2D perovskites is composed of an inorganic octahedral layer sandwiched by long organic cations, resulting in 2D quantum well structures. The general chemical formula for 2D perovskites is $\text{R}_2\text{A}_{n-1}\text{B}_n\text{X}_{3n+1}$, where R_2 is a long organic cation (phenethylammonium, butylammonium, ethylammonium, ...), A is a tiny organic cation (methylammonium (MA), formamidinium (FA), ...), B is a metal inorganic cation (e.g., lead, tin, and so on), and X is a halide inorganic anion (i.e., chloride, bromide, or iodide) [17–21]. 2D perovskites due to their excitonic properties are also promising materials for photonics and nonlinear devices working at room temperature. Nevertheless, strong excitonic effects can reduce the photocurrent characteristics when using thinner perovskites phases.

Lead and other hazardous heavy metals, on the other hand, are common cations used in perovskites materials. As a result, lead-free perovskites were developed as a low-cost, non-toxic, earth-abundant material for the next generation of optoelectronic applications [22].

This Ph.D. Thesis has been mainly focused on the optical characterization of LHP nanocrystals and 2D perovskites of phases PEA_2PbI_4 ($n=1$) and $\text{PEA}_2\text{MAPb}_2\text{I}_7$ ($n=2$) and their potentiality for applications in photonics and quantum technologies.

Lead Halide Perovskite Nanocrystals:

Since the first publication of lead-halide perovskite nanocrystals (PNCs) in 2014, several researchers all around the world have been actively examining them [23]. PNCs made of lead halides are made in the same way as standard nanocrystals using the chemical synthesis technique known as hot injection [24,25], and the Ligand assisted reprecipitation (LARP) method [26]. Basically, LARP is similar to hot injection but the synthesis is carried out at room temperature and with solvents different polarities. The size and shape of the NCs can be precisely tuned using this synthesis technique, ranging from bulky ones (low quantum confinement) to zero-dimensional quantum dots (QDs) [24]. Lead halide PNCs shown a high absorption coefficient, a quantum yield of emission that exceeds 90% at ambient temperature, and a tunable bandgap depending on chemical composition [24]. Furthermore, PNCs can also be processed from solution into films using standard techniques, such as spin coating or inkjet printing, on a wide range of optical architectures or substrates [27]. The fundamental morphology of a semiconductor NC, including the capping ligands that surround the perovskite crystal structure, is shown in Figure 1.1. The solubility, colloidal stability,

and interactions of NCs with their surrounding media are affected by these ligands. Additionally, the ligands in PNC close-packed films can serve as barrier to charge-carrier conversion and transport.

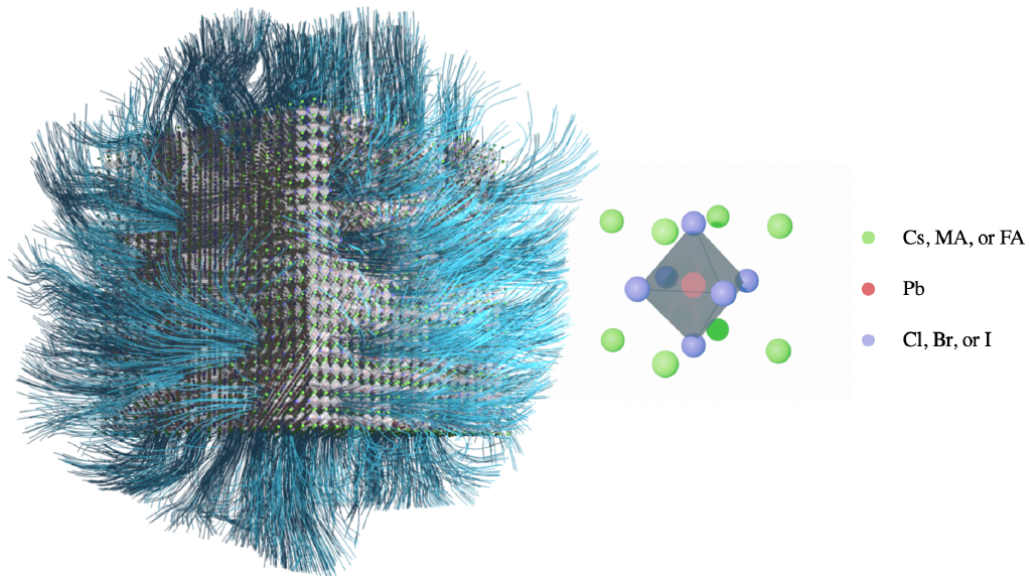


Figure 1.1: The unit cell of the LHP family is on the right, and a PNC is the left [28].

2D Perovskites:

Since the discovery of the high light-energy conversion efficiency published in 2009 [24], the use of perovskite materials has been demonstrated in a large number of photonics devices due to their remarkable aforementioned properties.

This rapid growth in academic activity has merged with a second intense field of research, the study of 2D monolayer semiconductors. The isolation of mechanically exfoliated graphene in 2004 has boosted the engineering of an interesting new set of high-quality 2D semiconductor samples that can be prepared at a low cost and without specialized equipment. This is the case for 2D LHPs [29, 30], which have recently been analyzed more closely

because of their potential integration in high-efficiency photovoltaics and photonic devices [17,31–33]. As a 2D van der Waals family material, layered perovskites show enhanced stability and structural tunability [17,29,34], but with a particular soft lattice and a dynamically disordered structure [35].

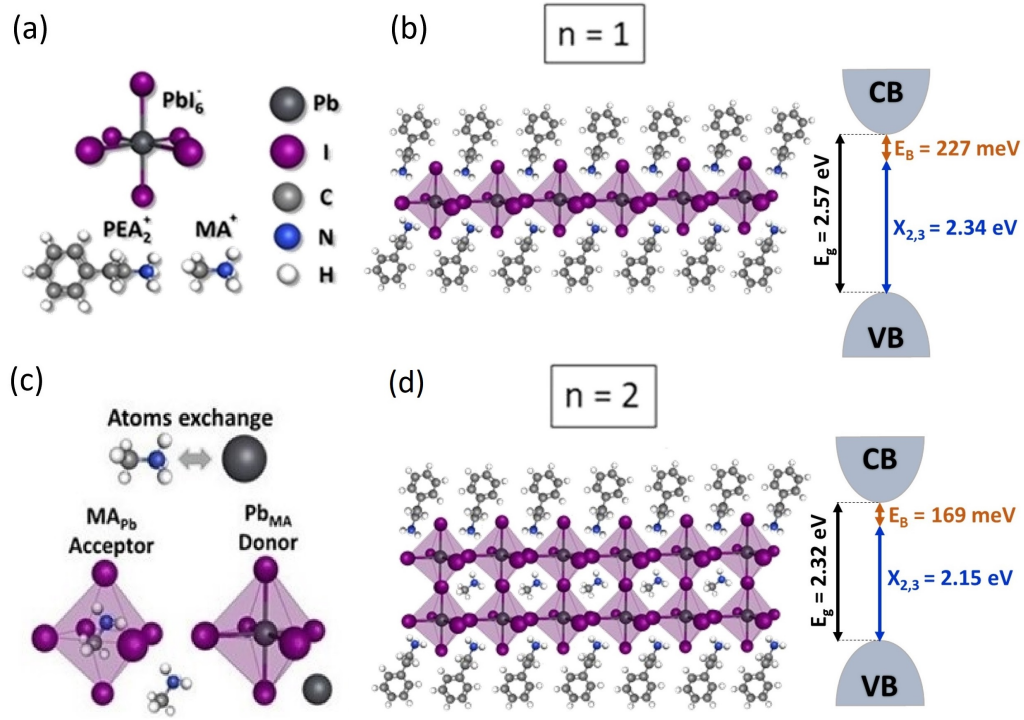


Figure 1.2: (a) 2D LHPs are composed of inorganic octahedral $(\text{PbI}_6)^-$, short organic methylammonium $(\text{MA})^+$ cation, and long organic Phenethylammonium $(\text{PEA}_2)^+$ cation. (b) Crystal structure of a 2D perovskite monolayer of the PEA_2PbI_4 ($n=1$) Ruddlesden-Popper phase, where a single octahedral sheet is sandwiched by a PEA_2 organic spacer. The inset image shows its bandgap with values taken from [36]. (c) Crystal structure of a quasi-2D perovskite monolayer of the $\text{PEA}_2\text{MAPb}_2\text{I}_7$ ($n=2$) Ruddlesden-Popper phase, consisting of two octahedral sheets intercalated with short MA molecules, sandwiched by a PEA_2 organic spacer. The inset image shows its bandgap with values taken from [36] and a donor-acceptor pair of Pb_{MA} and MA_{Pb} created by the MA and Pb atom exchanges [37].

Its crystal lattice typically consists of single or multiple organic–inorganic hybrid phases arranged into a Ruddlesden–Popper structure of formula $R_2A_{n-1}B_nX_{3n+1}$ [18]. In contrast to 3D perovskites, the semiconducting inorganic layer is passivated with insulating organic cations, forming a 2D

natural quantum-well structure where the electronic excitations are confined in the inorganic layers [34]. Its optical emission properties can be controlled by the n value in the above given formula, which labels the number of inorganic monolayers building the quantum well structure (from $n = 1, 2, 3$ to $\sim \infty$) [17, 34]. Figure 1.2.a-c shows the crystal structures of both PEA_2PbI_4 ($n=1$) and $\text{PEA}_2\text{MAPb}_2\text{I}_7$ ($n=2$) Ruddlesden-Popper phases. They are made up of a single layer ($n=1$) and a double layer ($n=2$) of perovskite inorganic octahedral flakes composed by $(\text{PbI}_6)^-$ anions sandwiched by long organic $(\text{PEA}^2)^+$ cations, which serve as spacers. The inorganic double layer is intercalated by short organic $(\text{MA})^+$ cations for $n = 2$. Only the $n = 1$ phase has a well-defined structure, whereas small inclusions of another n phase are formed for a higher inorganic flake thickness $n > 1$ [38]. Synthesized crystals can be easily exfoliated down to a few monolayers, thanks to the relatively weak van der Waals interlayer coupling. Exfoliation reduces the occurrence of unwanted hybrid phase formation [38] and leads to a strictly flat crystal orientation to the substrate [39], which may suppress the substrate's lattice imperfections.

Lead-free perovskites:

Recently, Lead-free perovskites, especially tin-based perovskites, have become attractive materials for light-matter interaction. Their advantages include straightforward fabrication by chemical synthesis, and Tin-based perovskites have drawn attention because of their low toxicity and the optimal optical bandgap (1.2-1.4 eV) close to the Shockley-Queisser (SQ) limit under 1 sun illumination. Among all of the lead-free perovskites, tin (II) halide perovskite has drawn attention because of the hybrid structure. The hybrid term refers to the combination of organic cations (in this case 2-

tiopheneethylammonium, TEA⁺) and an inorganic layer of tin iodide octahedral layer. Despite this, TEA₂SnI₄ perovskite exhibits high exciton binding energy and reduced exciton-phonon interactions (see Figure 1.3).

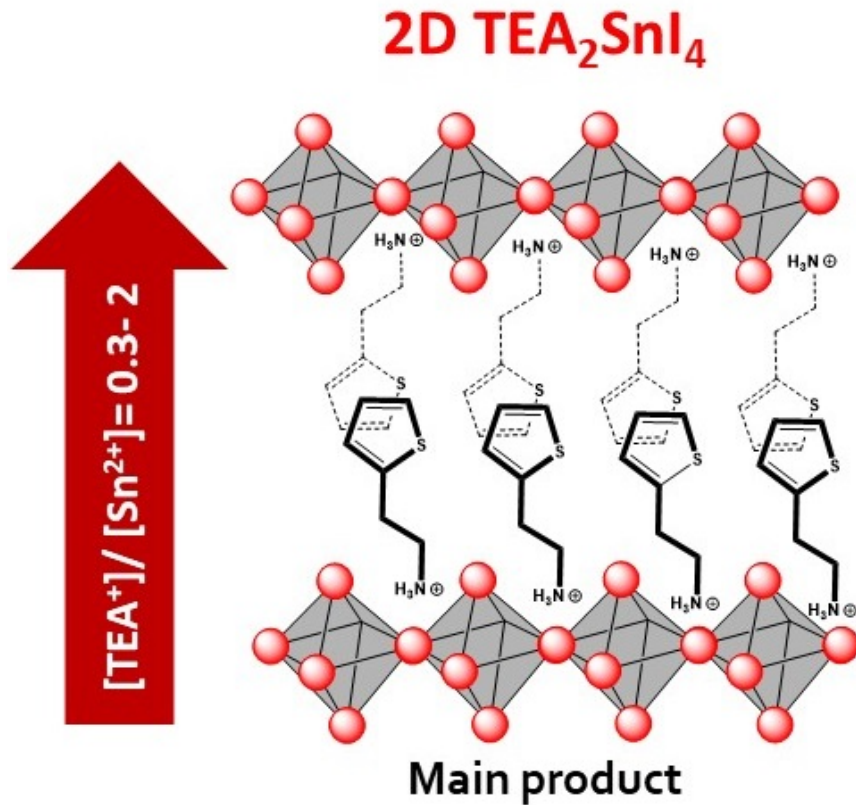


Figure 1.3: Scheme of 2D-TEA₂SnI₄ microcrystals.

Optical stability of CsPbX₃ (Br, I) perovskite nanocrystal for single photon emission

In addition to excellent optoelectronic properties of LHPs [40, 41] these materials have remarkable emission properties [42], as demonstrated by optically pumped amplified spontaneous emission [43] and lasing [44, 45]. All of these applications rely on thin films made up of microcrystalline per-

ovskite structures. However, such ensembles of crystallites do not exhibit strong quantum correlations between photons, even at the level of a single microcrystal [46].

Nonclassical light emission, observed in single organic dye molecules, [47] semiconductor quantum dots [48, 49], and color centers in diamond [50, 51] and other materials, has enabled deterministic single photon sources for secure quantum communication [52], quantum computing [53] and quantum sensing [54]. It would be attractive to use the high oscillator strength, high quantum yield, efficient charge transport, solution-processability, and ease of synthesis of these perovskites for such quantum applications. Fully inorganic PNCs of CsPbX_3 ($X = \text{Cl}, \text{Br}, \text{I}$) have been synthesized with precise size and compositional control, offering very bright, tunable, narrow-band luminescence over the whole visible wavelength range [55]. Due to the high defect tolerance and lack of detrimental mid-gap surface defects, high photoluminescence quantum yields of up to 90% at room-temperature, which can be achieved without any additional surface passivation. This opened up a plethora of possibilities for tunable quantum light sources based on compositional and quantum-size tuning.

Despite the fact that colloidal lead halide PNCs have emerged as versatile photonic sources, their processing and optoelectronic applications are hampered by the loss of colloidal stability and structural integrity caused by the facile desorption of surface capping molecules during isolation and purification, resulting in unwanted spectral diffusion and blinking effects.

To address this issue, a new ligand capping strategy is suggested in this thesis that employs inexpensive long-chain zwitterionic (ZW) molecules, *N* – Dodecyl – *N*, *N* – dimethyl – 3 – ammonio – 1 – propanesulfonate, resulting in significantly improved chemical durability. This class of lig-

ands, in particular, enables the isolation of clean PNCs with photoluminescence quantum yields (PL QYs) of more than 90% [56]. Bidentate ZW ligands, which have two functional groups that can bind to NCs, are particularly attractive [56–58] due to their ability to improve the stability of NCs and enhance ligand–surface interactions. The bidentate ligands show great promise for efficient surface passivation and PL enhancement [59]. Krieg et al. [56] suggested using long-chain ZW molecules as capping ligands for CsPbX₃ NCs, and these ligands demonstrated a significant improvement in durability and stability [56].

In this thesis, cryogenic micro-PL and micro-TRPL (Time Resolved PL) spectroscopy were used to examine single PNCs with two different capping ligands and determine the average homogeneous linewidth of excitonic optical transitions in freshly prepared samples for both cases at 4 K. In contrast with conventional oleylamine / oleic acid (OLA/OA) ligands, the homogeneous linewidths of the CsPbBr₃ NCs with ZW ligands exhibit a significant narrowing with higher stability due to drastically decreased spectral diffusion and blinking effects. Furthermore, based on micro-TRPL measurements, a slightly longer decay time (an increase of a factor ~ 1.35) was observed for CsPbBr₃ single NCs with ZW ligands, making them better for quantum light sources. However, in the case of CsPbI₃ NCs, this strategy (using ZW ligands) does not work, and the traditional OLA/OA ligands are still the best candidate.

Donor-acceptor discrete optical emission in 2D perovskites

Single layer 2D perovskites show strong Coulomb interaction, due to the effect of the quantum confinement and the weak dielectric screening. Conse-

quently, excitonic states for 2D HPs with a small n number are characterized with binding energies up to several hundreds of meV [29], which returns excitonic stability even at room temperature [60] and following the emergence of large fine structure energy shifts [61, 62]. The intense excitonic features that are present in these small n value 2D HPs play an important role in the development of new and promising optoelectronic devices. At first, the high excitonic binding energy characteristics of small n values 2D HPs reduces the overall photocurrent generation for solar cell applications [63]. Thus, for these purposes, larger n values samples ($n = 3$) with smaller excitonic binding energies are conventionally used [21]. However, there is a different strategy to produce a high generation of carriers (i.e., photocurrent) in 2D HPs with small n values. The dynamical charge from Donor-Acceptor pairs (DAP) could be an important physical process to evaluate the performance of different optoelectronic devices, based on the use of low n number 2D perovskites [21]. In fact, DAP charge transfer processes between $n = 1$ LHPs interfaced with an organic semiconductor used as spacer layer, which enhances photocurrent production [21]. Interestingly, another study has reported that a molecular doping by small electron acceptor molecules of 3,4,5,6-tetrachloro-1,2-benzoquinone (TCBQ) into $n = 1$ LHPs containing naphthalene cations molecules serving as a donor, give rise to a formation of DAP within the organic layer [64]. These DAP organic species between the inorganic layers can be used to increase the electrostatic screening of the exciton, and hence to tune the excitonic binding energy in 2D hybrid layered perovskite samples [21, 64], which is an important strategy to gain control of the performance of optoelectronic devices. In another direction, there is an open debate about the identification of the optical transitions that are present in the emission spectra of 2D LHPs, where extrinsic effects

(e.g., DAP) are suggested as possible states producing red-shifted optical emission with respect of gap [65]. Therefore, the study of DAP states in 2D LHPs is revealed as an important area of research.

In this thesis, a single DAP carrier optical recombination that provides very narrow and long-lived optical transitions in 2D LHPs based materials at low temperatures was measured and identified. By means of spatial and μ -TRPL, optical transitions with narrow linewidths, as low as $\simeq 120\mu eV$ FWHM, and time decays as long as 8.6 ns, were measured. X-Ray photoelectron spectroscopy (XPS) has been employed to identify chemical processes giving rise to electronic states responsible to DAP-related optical transitions. In particular, the DAP transitions appears to be related to the exchange of methylammonium (MA) molecule and Pb atoms present in 2D HPs samples with phase thickness $n = 2$, leading to optical recombination in a broad spectral range between two excitonic transitions. This claim is supported with complementary optical spectroscopic data by means of μ -Raman spectra. The experimental effort is accompanied with predictions from a simple model to calculate the density of states (DOS) as a function of DAP binding energy, which is built up by the attractive Coulombic interaction between their net charges. This result represents an important step forward in understanding the nature of the DAP state in 2D LHPs, its spectral features, and its relationship with the selected cation spacer and the layer thickness n value. This has important consequences for the design of new optoelectronic architectures.

Light-Matter interaction and Light mode coupling in an open access fiber-based optical microcavity

Controlling spontaneous emission (SE) is crucial from both a scientific and a technological points of view. Conventional methods for enhancing spontaneous emission by changing the dielectric environment rely on phenomena like cavity resonance, in which the spontaneous emission rate is increased throughout a small spectral range. The incorporation of an out-coupling mechanism lowers the cavity's quality factor, which result in a higher SE rate [66,67]. A Fabry-Perot optical cavity confines light by using two highly reflective parallel mirrors. To interact with cavity modes, emitters can be deposited between these mirrors. To guarantee that the coupling rate between the optical field and the emitters surpasses the system optical and material loss, the electric field of the cavity mode must be maximized at the position of the emitter.

Dielectric distributed Bragg reflectors (DBRs) are commonly used to achieve the extremely high reflectivity mirrors required for these types of cavities. DBRs are made up of layers of alternating refractive index dielectric material with a thickness of $d = \lambda_0/4n_i$ ($i=1, 2$), where n_i is the refractive index of each dielectric layer, and λ_0 is the wavelength of light. In recent years, open-access, semi-integrated fiber based microcavity designs [68] have been attracting a lot of attention. These open-access designs can replace one of the integrated semiconductor DBR mirrors with a completely independent concave dielectric DBR mirror. The Gaussian shaped geometry of the replaced DBR (Details are in chapter 2.2.4) provides a strong optical confinement of the cavity modes in the lateral dimension. The open style of the fiber cavity allows for independent movement of the fiber mirror, which is typically controlled by piezo nanopositioners. This in-

dependent movement enables in-situ tuning of the cavity resonance without the reduction in the coupling experienced by their monolithic alternatives, and typically over a wider spectral range.

Herein, the open access fiber-based microcavity was successfully mounted, and different factors of such cavity setup tested. This setup was numerically modeled in order to accurately understand the potential Light-Matter interaction and Light mode coupling. Finally, LHPs NCs were deposited inside the cavity, and weak coupling was observed and extracted the Purcell factor for this spontaneous emission enhancement. Finally, strong coupling was observed between Bloch waves in the DBRs and weakly confined modes of the microcavity outside of its stop band.

Thesis objectives

The main objective of this Ph.D. thesis, is to use 2D perovskites and PNCs for photonic and quantum applications in the visible wavelength range (500 - 700 nm). For this purpose, the outstanding optical properties of 2D perovskites and PNCs are used to bring different functionalities, such as single photon emission, single donor-acceptor discrete optical emission, and Light-Matter interaction and Light mode coupling, into different photonic and quantum applications. As a result, we can split the main goals into three secondaries:

1. The most important physical mechanisms responsible for spontaneous emission in PNCs must be investigated. Single PNC samples will be examined first as fundamental building blocks for quantum light sources, from which more complex architectures can be built. Controlling the emitted light by single PNCs and completely characterizing its dependence on ex-

citation fluency, capping ligands and passivation to have a stable emission, and determining their exciton lifetimes, are all important steps toward this objective. Once the ideal conditions for PNCs have been established, they can be used as quantum light sources, with the single photon purity being evaluated by the second order correlation function, $g^{(2)}(0)$ at zero delay, as it will explained in the section 1.2.

2. The next landmark will be the investigation of 2D perovskites, a type of van der Waals nanomaterial, for its potential use in photonic and optoelectronic applications at the nanoscale. Optimizing the conditions for mechanical exfoliation of bulk layered crystals of two different phases of 2D perovskites with the lowest quantum well thickness of $n=1$ and $n=2$ to achieve sufficiently thin 2D is an important step toward achieving this goal. Once the optimal conditions for these two different phases of 2D perovskites with $n=1$ and $n=2$ are established, their optical properties can be investigated at low temperatures using a confocal micro-PL spectroscopy set-up.

3. In addition, Open-access, semi-integrated fiber-based microcavity designs have received a lot of attention in recent years. The cavities' specific geometry provides strong optical confinement of the modes. The open fiber-based microcavity is a photonic device that can be used for a thorough understanding of the possible Light-Matter interaction and Light mode coupling based on numerical models. The final step will be to deposit different perovskite materials (PNCs and, a 2D Lead-free perovskite) in the microcavity to investigate Light-Matter interaction and Light mode coupling.

Thesis outline

The present Ph.D. thesis addresses a variety of research topics including the utilization of different types of perovskites as active materials in photonics and quantum applications. The manuscript's structure includes the current introductory chapter and one other grouping all laboratory methodologies and setups required to adequately comprehend the experimental findings, which are presented in the three subsequent chapters. In the end, a general conclusion chapter concludes this thesis.

Chapter 1: Introduction

This chapter provides a brief history and current state of the art of Perovskite materials, with a focus on the applicability of these materials and the main objectives of the current Ph.D. Thesis.

Chapter 2: experimental techniques

The purpose of this chapter is to go over the fabrication and characterization techniques utilized in the research tasks carried out in this PhD thesis.

Chapter 3: Single photon emitters (LHP)

In this chapter, cryogenic micro-PL and micro-TRPL spectroscopy were used to examine single PNCs at 4 K with two different capping ligands and determine the average homogeneous linewidth of excitonic optical transitions in freshly prepared samples for both cases. In comparison to the typical OLA/OA ligands, the blinking free homogeneous linewidths of the CsPbBr₃ PNCs with ZW ligands show a significant narrowing with higher stability. Furthermore, based on micro TRPL measurements, a slightly longer decay time (a factor ~ 1.35) was observed for single CsPbBr₃ PNCs

with ZW ligands, making them better for quantum light sources, as demonstrated by a second order photon correlation function $g^2(0) \sim 0.5$. However, in the case of CsPbI₃ PNCs, this strategy (using ZW ligands) does not work, and the traditional OLA/OA ligands are still the best candidate. For CsPbI₃ PNCs, a second order photon correlation function $g^2(0) \sim 0.3$ is obtained.

Chapter 4: Donor-acceptor (2D Perovskites)

A single Donor-Acceptor Pair (DAP) carrier optical recombination that provides very narrow and long-lived optical transitions in 2D LHPs based materials at low temperature was measured and identified. By means of spatial and μ -TRPL, optical transitions with narrow linewidths, as low as $\simeq 120\mu eV$ FWHM, and time decays as long as 8.6 ns were recorded. It has been identified that the origin of these transitions as the DAP recombination is ascribed to the exchange of methylammonium (MA) molecule and Pb atoms present in 2D HPs samples with phase thickness $n = 2$, leading to optical recombination in a broad spectral range between two excitonic transitions. This important claim is supported with strong experimental evidence by means of μ -Raman spectra and high-resolution photoemission spectroscopy measurements. The experimental effort is accompanied with predictions from a simple model to calculate the density of states (DOS) as a function of DAP binding energy, which is built up by the attractive Coulombic interaction between their net charges. This PhD thesis represents an important step forward in understanding the nature of the DAP state in 2D LHPs, its spectral features, and its relationship with the selected cation spacer and the layer n-value. This would have important consequences for the design of future new optoelectronic architectures. Moreover, the ability to isolate single DAP states can potentially be used to study advanced po-

laritonic strategies with very sharp and bright optical transitions in a high non-linear material, with binding energy/DAP radius tunability, and hence to stimulate the use of 2D LHP semiconductors as promising materials to produce new alternatives to be considered in the actual quantum material database [69–71].

Chapter 5: Open access microcavity

In this chapter, the open access fiber-based microcavity was successfully mounted, and different factors of this cavity setup, such as glue the fiber mirror to a fiber holder, mounting piezoelectric motors, and so on, were properly controlled. This setup was numerically modeled in order to accurately understand the potential Light-Matter interaction and Light mode coupling. Finally, PNCs were deposited inside the cavity, and weak coupling was observed and extracted the Purcell factor for this spontaneous emission enhancement. Finally, strong coupling was observed between Bloch waves in the DBRs and weakly confined modes of the microcavity outside of its stop band and modelled the coupling with transfer matrix approach which is a mathematical technique that allows to solve the Schrödinger or Maxwell equations in multilayer systems, and Comsol (Finite Elements).

Chapter 6: Conclusions and future prospects.

This chapter summarizes the essential conclusions and future opportunities that came from the current Ph.D. study.

1.2 Fundamentals and Physical Background

Homogeneous linewidth, Spectral diffusion and Blinking effect:

In the approximately 70 years since Bloch's original description [72], significant progress has been made in explaining the physical mechanisms responsible for T_1 and T_2 times. Within the framework of the damped optical Bloch equations that describe the macroscopic properties of a collective of identical two-level systems and under the relaxation time approximation, the following relationship between characteristic times can be defined:

$$\frac{1}{T_2} = \frac{1}{2T_1} + \frac{1}{T_2'} \quad (1.1)$$

Where T_2 is referred to as the phase delay time, T_1 represents the decay time from level 2 to level 1 and T_2' is called pure dephasing time. The homogeneous width of the absorption curve is inversely proportional to the dephasing time T_2 . In the limit of the linear regime of susceptibility (leaving out higher order effects such as power broadening or quadratic Stark shift) the line shape of the absorption coefficient in a two level system is a Lorentzian, where its FWHM is expressed as:

$$\gamma = \frac{2\hbar}{T_2} \quad (1.2)$$

This framework can be applied to carriers and excitons in QDs. The exciton in a semiconductor can be modeled as a two-level system. The lifetime of the excitons is T_1 . In the absence of interactions with phonons or other carriers and without contemplating non-radiative channels, the time lag (T_2) in a InAs QD will be limited by the lifetime. If we focus on

the strong confinement regime (see section 1.2) (Bohr radius of the exciton larger than the radius of the nanostructure), the experimental PL transients would indicate a value of the lifetime that typically oscillates in the range of 1-2 ns [73]. Thus, the typical widths of excitonic transitions should be in the order of approximately $\gamma \geq 0.66 \mu\text{eV}$. Different physical mechanisms affect to the final width and shape of the optical transition. The broadening mechanisms are classified as homogenous and inhomogeneous. The homogeneous mechanisms generally give rise to Lorentzian lineshapes (red curves), while inhomogeneous processes tend to produce Gaussian spectral lines (black curves), which are shown in the Figure 1.4.

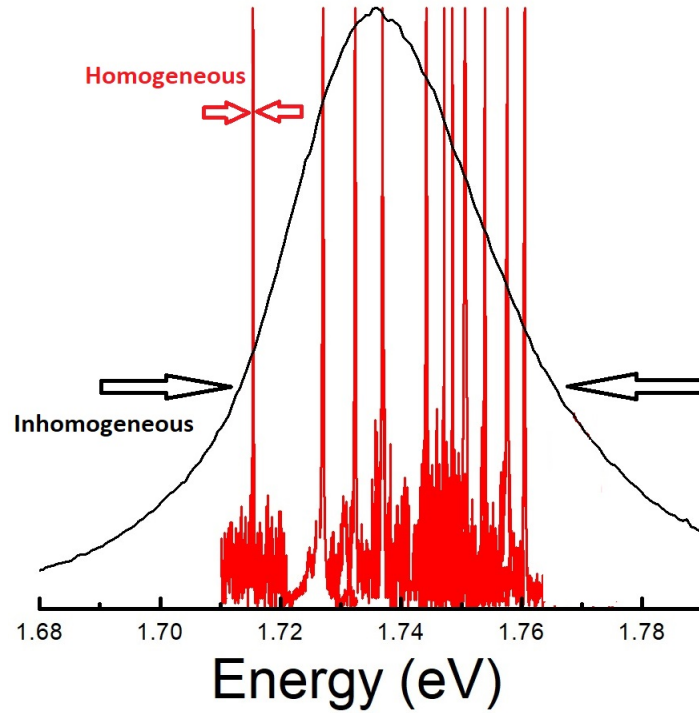


Figure 1.4: The μ -PL spectra of single CsPbI₃ PNCs (red curves) are homogeneously broadened, as compared to the inhomogeneously broadened PL spectrum (black curves) of a high-density sample containing the same PNCs.

Spectral diffusion is the random movement of a homogeneous line's energy (PL emission of a single NC) that occurs when charge and spin

changes occur on a timeframe longer than the radiative lifespan, resulting in spectral walking of the emission energy from one photon to the next (see Figure 1.5). Homogeneous line broadening can increase with excitation power due to the presence of local electric field fluctuations induced by photoexcited carriers. The increase of the homogeneous linewidth is associated with spectral diffusion phenomena. This effect is related to the charging and discharging of traps near the nanostructures at shorter time intervals than the typical integration times of micro-photoluminescence spectra. In this way, a time-fluctuating quantum confinement Stark effect is generated and the energy of the electron and hole levels of the nanostructure undergoes slight modifications that result in an inhomogeneous temporal distribution of emission energies.

The emission spectra of single nanocrystals have mostly been studied at cryogenic temperatures (4 - 10 K) because the narrowing of spectral linewidths at low temperatures shows a complex set of physical phenomena [48, 74]. Specifically, initial studies of single nanocrystals at low temperatures revealed that the emission spectra were very dynamic in terms of amplitude and duration (see Figure 1.5) [75, 76]. These spectra showed huge jumps of tens of meV as well as fast jitter that appeared to determine the observed time-integrated linewidth on sub-second timescales.

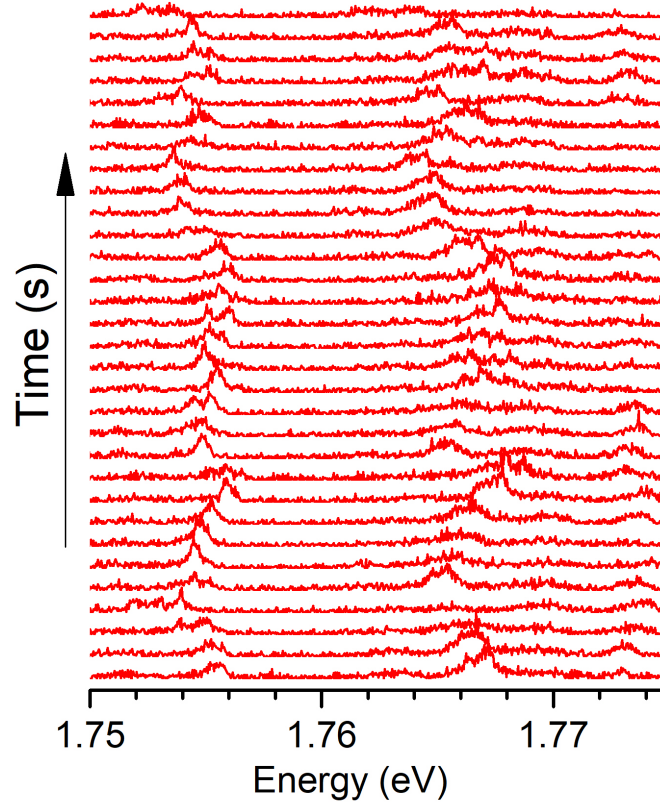


Figure 1.5: The time dependence of the μ -PL intensity of single CsPbI₃ PNCs, which shows the emission spectrum variation with time.

Blinking (fluorescence intermittency) is the phenomenon of the emitter randomly switching between ON (bright) and OFF (dark) states while it is excited, which is linked to the competition between the radiative and non-radiative relaxation routes or between two radiative routes, for example between excitons and trions, which are both radiative. Moreover, practically most of colloidal nanocrystal quantum dots (QDs) display intermittent emission, which is referred to as PL 'blinking'. Such PL blinking evident in a single QD would be easily smoothed out and so undetectable in ensembles of QDs. In fact, the photophysics of blinking could only be detected at the single QD level, as Nirmal et al. [77, 78] discovered in tests of isolated

CdSe QDs under steady-state laser excitation conditions. Figure 1.6.b depicts the time-dependent μ -PL spectra of a single CsPbI₃ PNC under CW excitation at 4K. The time dependence of μ -PL spectra, as shown in Figure 1.6.b, demonstrates a sequence of "on" and "off" periods. The most widely accepted hypothesis at the moment is that the blinking events occur as a result of illumination-induced charge (on \rightarrow off) followed by reneutralization (off \rightarrow on) of the PNC, similarly to the case of CdSe QDs [79]. This occurs because, for an uncharged NC, a photon excites an electron-hole pair (exciton), which then recombines, emitting another photon and giving rise to the PL (see Figure 1.6.a), a process known as radiative recombination. In the presence of an excess charge (charge separation in a neutral NC), the resulting electric fields can readily be on the order of tens of MV cm^{-1} . These high fields trigger a process known as non-radiative recombination, by which efficiently transfers the additional exciton energy to the extra electron or hole (see Figure 1.6.c).

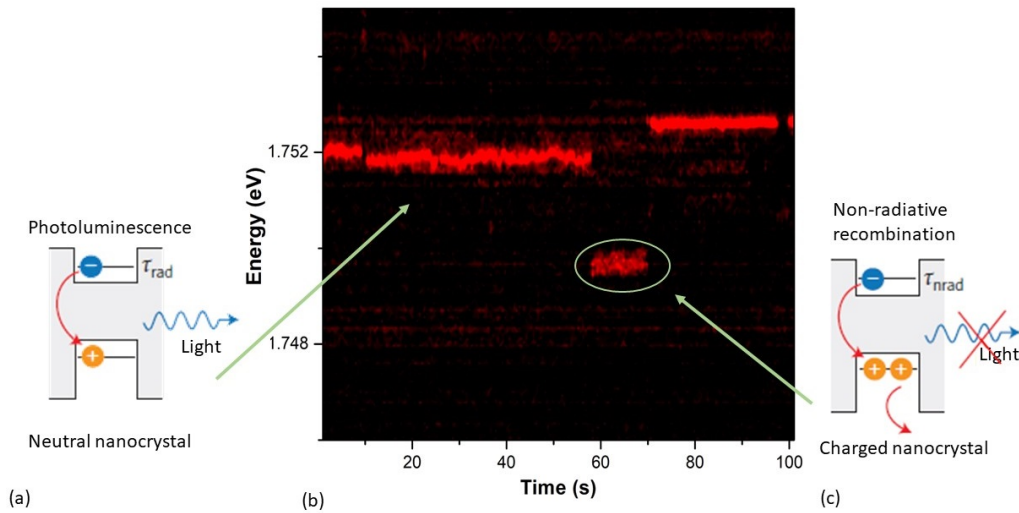


Figure 1.6: (a-c) Time dependence of the μ -PL spectrum measured in a single CsPbI₃ PNC (b) together with the recombination schemes for neutral (a) and charged (c) PNCs at different energies.

Photon Correlations:

Optical spectroscopy comprises a series of experimental techniques for analyzing light and describing its physics. Conventional spectroscopic methods, such as obtaining spectra through a spectrometer, provide certain information, such as the relationship between wavelength and intensity, the discrete or continuous nature of the emission, etc. However, there are situations in which the properties defining the light under investigation remain hidden from general spectroscopic methods. For example, the spectra of a sufficiently attenuated laser light and a spectral lamp could be equivalent (in wavelength and linewidth, for example), but there are substantial differences arising from the emitting system itself and its emission conditions. Not even conventional interferometric methods, such as those derived from Young's double-slit experiment, would not generate a differentiated interference pattern. Other approaches must be used to investigate some of the physical characteristics of light that are yet unknown.

The $g^n(\tau)$ coherence functions, which are normalized correlations of the photon field, are typically used in quantum optics to explain the coherence properties of the photon state. The first-order coherence function, $g^1(\tau)$, expresses phase coherence in time using normalized self-correlations of field amplitude. The phase coherence of a system provides information about interference effects, phase modulation, and noise. The second-order coherence function, $g^2(\tau)$, returns information about the statistical time distribution of photons via self-correlation of field intensity. Photon statistics can be classified into three types: Poissonian ($\Delta n = \sqrt{\bar{n}}$), super-Poissonian ($\Delta n > \sqrt{\bar{n}}$), and sub-Poissonian ($\Delta n < \sqrt{\bar{n}}$), where (Δn) represents the standard deviation of the photon number fluctuations, and \bar{n} is the mean value of the photon number, which refer to fluctuations with equal, larger,

or smaller variation than an uncorrelated, coherent photon state with a Poissonian probability of finding N photons in an interval τ . These photon number distributions are defined using the self-correlation version of the second-order coherence function 1.3, given by [66]:

$$g^{(2)}(\tau) = \frac{\langle \hat{a}^\dagger(t) \hat{a}^\dagger(t + \tau) \hat{a}(t + \tau) \hat{a}(t) \rangle}{\langle \hat{a}^\dagger(t) \hat{a}(t) \rangle \langle \hat{a}^\dagger(t + \tau) \hat{a}(t + \tau) \rangle} \quad (1.3)$$

where $\hat{a}^\dagger(t)$, $\hat{a}(t)$ are the photon creation and annihilation operators respectively. The $\langle \dots \rangle$ symbols indicate the time average computed by integrating over a long time period. Because the fluctuations in a Poissonian photon distribution state are random, $g^{(2)}(\tau) = 1$ for all values of τ , and thus the probability of detecting two photons at any given time interval is equal. This value would be observed for a completely coherent light source, such as a laser. The larger fluctuations in a super-Poissonian state than in a Poissonian state mean that as τ approaches zero, the probability of detecting two photons increases. Therefore, the value of $g^{(2)}(0) > 1$ is obtained, and photons are said to be "bunched". This value is often referred to as 'thermal light' or chaotic and would occur for an incoherent light source such as a candle. The reduced fluctuations in the sub-Poissonian photon number state compared to the Poissonian state mean that as τ approaches 0, the probability of detecting coincidences decreases. Therefore, the value of $g^{(2)}(0) < 1$ is obtained, and the photons are said to be "antibunched" (see Figure 1.7). This value less than 1 demonstrates a quantum nature of the photon field as the field is now discretized and can only be interpreted using a quantum definition of light. This means that for values of $g^{(2)}(0) \geq 1$, the photon field can be described using classical (semi-classical) definitions of light, while values $g^{(2)}(0) < 1$ demonstrate the photon field is in a non-trivial, non-classical state which can be described as a quantum in

nature or, more commonly, as so-called "quantum light".

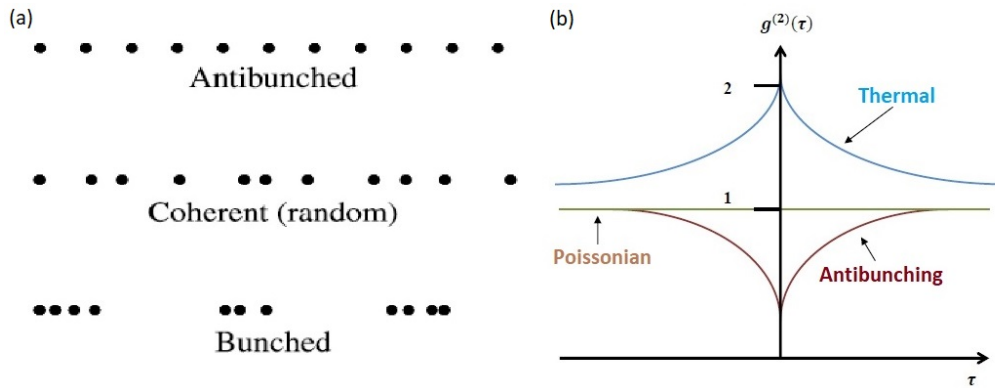


Figure 1.7: (a) Comparison of the photon chains generated by a sub-Poissonian (antibunched), Poissonian (coherent) and Super-Poissonian (Bunched) light system. [66] (b) Evolution of the second order correlation function for the Thermal, Poissonian (or coherent) and antibunching regimes. [80]

The relation between a second-order correlation function and the coincidence rate:

In order to analyze the results of the photon correlation experiment, it is necessary to relate the histogram of coincidences obtained by the Hanbury-Brown and Twiss interferometer, (see Figure 1.8), to the second-order correlation function ($g^2(\tau)$). A coincidence counter is an electronic system that produces an output signal when one photon is detected in the start detector and one in the stop detector.

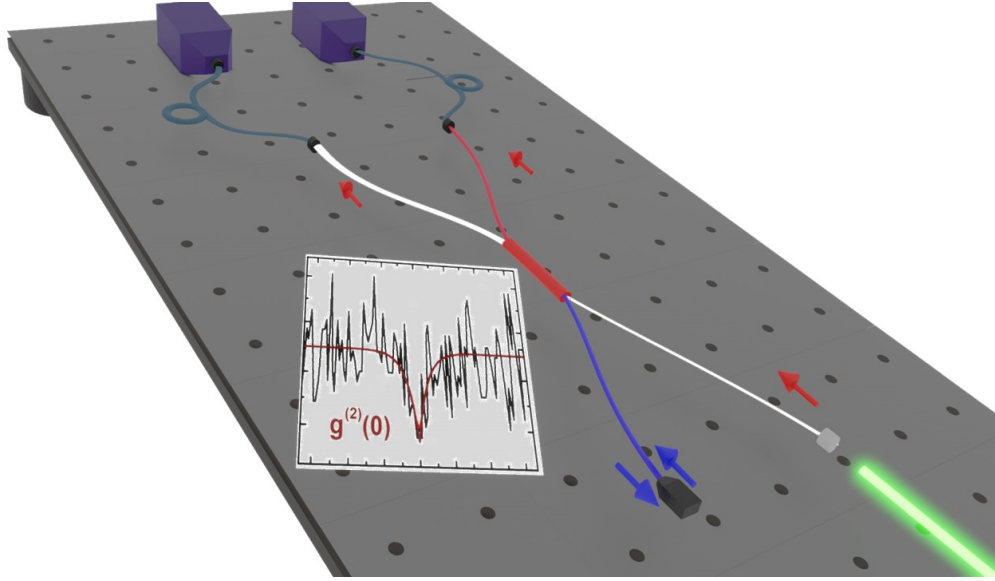


Figure 1.8: Schematic representation of Hanbury Brown and Twiss experimental setup.

The detection is considered simultaneous if it occurs in a time less than the temporal resolution of the circuit, given by the channel width of the electronic board (T_r). In other words, two detection events occurring at times t and $t + \tau$, will be displayed as occurring simultaneously if $|\tau| \leq \frac{1}{2}T_r$. In any other case, it will be said that the coincidence occurs with a delay τ between the start and stop events. After an integration time T , the number of coincidences recorded with delay τ is related to $g^{(2)}(\tau)$ by [81]:

$$C(\tau) = T \times T_r (r_1 + \gamma_1)(r_2 + \gamma_2) + T \times T_r \times r_1 r_2 (g^{(2)}(\tau) - 1) \quad (1.4)$$

where $r_{1(2)}$ is the rate of counts coming from incident light on detector 1(2) and $\gamma_{1(2)}$ is the rate of counts produced by the noise in detector 1(2), respectively. The first term of this equation represents the number of coincidences coming from the signal plus noise for each channel. On the other hand, the second term accounts for the decrease or excess of coincidences

due to non-random intensity fluctuations of the investigated light. The first part of this equation represents the number of coincidences coming from the signal plus noise for each channel. The second part reports the decrease or increase in coincidences due to non-random intensity fluctuations of the investigated light.

In order to evaluate the value of the function $g^2(\tau)$ in specific situations, it is interesting to derive an expression for the coincidence rate that is normalized and where the effect of detector noise can be eliminated. The normalized coincidence rate can be estimated from equation 1.4 as $C_N(\tau) = \frac{C(\tau)}{N_1 N_2 T_r T} = 1 + \rho_1 \rho_2 (g^{(2)}(\tau) - 1)$, where $N_1 = (r_1 + \gamma_1)$, $N_2 = (r_2 + \gamma_2)$, $\rho_1 = \frac{r_1}{r_1 + \gamma_1}$, and $\rho_2 = \frac{r_2}{r_2 + \gamma_2}$.

Therefore, the second-order correlation function can be related to the coincidence rate normalized by:

$$g^{(2)}(\tau) = [C_N(\tau) - (1 - \rho_1 \rho_2)] / (\rho_1 \rho_2) \quad (1.5)$$

Exciton, biexciton and trion:

In the most basic understanding of semiconductor materials, the highest valence electron band is completely occupied, whereas the lowest conduction electron band is empty. These bands are separated by energy, which has been identified as ‘band-gap’ energy, E_g , which is the energy needed for an valence band electron to transition into the conduction band. Once an electron is excited to the conduction band, it effectively leaves behind a positive ‘hole’ in the valence band. Whereas transitions between the valence and conduction bands can not occur for free electrons with energies less than E_g , electron-hole pairs can form bound states because of the Coulomb attraction called exciton, which lie just below the energy band gap. These

quasi-particles have wave-functions similar to hydrogen atoms. However, because of their low effective mass and the large dielectric constant of the semiconductor material, exciton Bohr radius a_X is larger than that of their atomic counterparts and can extend over several lattice sites. A modified Rydberg equation can be used to determine the energy levels of these excitons [82]:

$$E_n = E_g - \frac{e^2}{8\pi\epsilon a_x n^2} + \frac{\hbar^2 k^2}{2(m_e + m_h)} \quad (1.6)$$

where n is the principle quantum number, m_e and m_h are the electron and hole effective masses, e is the electron charge, ϵ is the appropriate dielectric constant and a_x is the exciton Bohr radius is $a_x = \frac{4\pi\hbar^2\epsilon}{e^2\mu}$, and $\mu = \frac{m_e m_h}{m_e + m_h}$.

Excitons decay by radiative recombination, in which the electron relaxes back into the corresponding hole in the valence band. As a result of this process, a photon is emitted equal to the binding energy plus the band-gap energy of the exciton. There are two types of excitons: Frankel excitons and Wannier excitons. Frenkel excitons are defined as tightly bound excitons with a very small Bohr radius that are typically confined to one lattice site. Wannier excitons, on the other hand, are weakly bound excitons with a large Bohr radius that can extend over several lattice sites (see Figure 1.9) and are typically found in inorganic semiconductor crystals. Unlike Frenkel excitons, Wannier excitons are relatively free to move in the crystal, with typical diffusion lengths up to several micrometers.

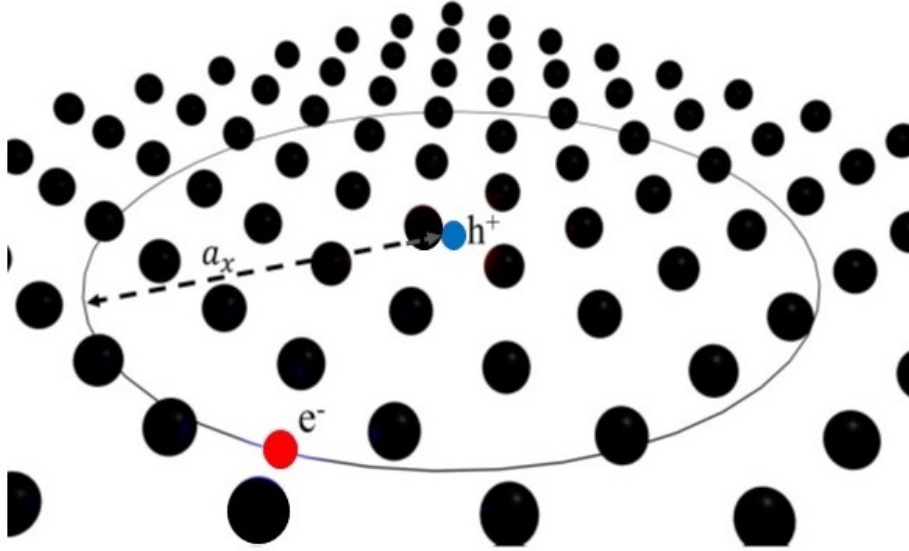


Figure 1.9: A bound electron-hole pair (red electron, blue hole) with a large Bohr radius extending over several lattice sites (black dots) [68].

The excitonic emission spectrum in a QD is found in the same spectral range as that of a biexciton or a charged exciton. This is easy to understand since the exciton is a charged neutral compound that interacts weakly with other excitons or charges. This means that shifts in the energy levels of these complexes are caused by both deviations from charge neutrality, i.e., how different holes are from electrons and mixed configurations. The mixing of configurations is, in turn, a function of characteristics such as the electron-to-valence-hole mass ratio, the confining potential for either carrier.

The trion, also known as the charged exciton, is a three-charge complex that can arise when an exciton is produced in the presence of an unpaired charge carrier in the QD. A negatively (positively) charged exciton is made up of two electrons (holes) with the same energy level as each other and one hole (electron) bonded together by Coulomb contact.

Strong and Weak Quantum Confinement:

The electronic structure and optical transitions in semiconductor materials change at the nanoscale due to quantum size confinement in one or more dimensions.

Strong confinement:

In the case of strong quantum confinement, the confinement energy is significantly larger than the Coulomb energy of the system. As a result, electrons and holes are individually confined, and their movement is also independent [83–85].

$$E_{n,l}^{e,h} = \frac{\hbar^2 \alpha_{n,l}^2}{2m_{e,h}^* R^2} \quad (1.7)$$

Here, m_e^* and m_h^* indicate the effective masses of the electron and hole, respectively. In the case of an e-h pair, it assumes the form [86, 87], Bohr radius is $a_0 = \frac{\epsilon \hbar^2}{2\pi \mu e^2}$ where $\mu = \frac{m_e^* m_h^*}{m_e^* + m_h^*}$, is the conventional reduced mass of the e-h pair. Where $\alpha_{1,0} = \pi, \alpha_{1,1} \approx 1.43\pi, \alpha_{2,1} \approx 1.83\pi$ etc. [88]. For an allowed optical transition, n and l are conserved, as revealed by the selection rules of dipolar transition. The total energy corresponding to the first allowed transition ($n_e = n_h = 1, l_e = l_h = 0, m_e = m_h = 0$) can be presented by [84, 85]:

$$E_{1s-1s} = E_g + \frac{\hbar^2 \pi^2}{2\mu R^2} - \frac{e^2}{\epsilon} \frac{1.8}{R} \quad (1.8)$$

Researchers have reported the size (R) dependence of the band gap under a strong quantum confinement regime.

Weak confinement:

When the size of the nanoparticles is larger than the Bohr radius, the quantum confinement is weak. In this case, the interaction potential of the

e-h system due to quantum confinement is also very negligible in comparison to the Coulomb potential. To calculate the band energies, it is needed to solve the Schrodinger equation for the e-h system. The energy associated with the optical transitions in the nanocrystals under a weak quantum confinement regime, can be expressed as [83, 84, 87]:

$$E_n = E_{bulk} - E_{ex} + \frac{\hbar^2 \pi^2}{2MR^2} n^2 \quad (1.9)$$

Here, M is the total mass of e-h pair and R is the center of mass of the e-h system.

Donors and acceptors pairs:

Donors and acceptors can form pairs and behave as stationary molecules in the host crystal. The Coulomb interaction between a donor and an acceptor causes their binding energies decrease. As the neutral donor (D^0) and the neutral acceptor (A^0) are brought closer together, the donor's electron becomes increasingly shared by the acceptor. In other words, the donor and the acceptor become more ionized (D^+), and (A^-) respectively. The binding energy is zero in the fully ionized state, and the corresponding level lies at the band edge. Electrons and holes in the conduction and valence bands can be created by optical excitation, respectively (see the process in Figure 1.10). These carriers can then be trapped at the (D^+), and (A^-) sites to produce neutral (D^0) and (A^0) centers. This process is known as a donor-acceptor pair transition (or DAP transition). It can be represented by the reaction: ($D^0 + A^0 = \hbar\omega + D^+ + A^-$). At first sight, one may expect the photon emitted in a DAP transition to have energy: ($\hbar\omega = E_g - E_A - E_D$), where E_g is the bandgap energy and E_D and E_A are the donor and acceptor binding energies, respectively. The amount by

which the impurity levels are shifted as a result of this pairing interaction is essentially the Coulomb interaction inside a dielectric constant medium ϵ : ($\Delta E = \frac{e^2}{4\pi\epsilon_0\epsilon_r R}$). Where R is the donor-acceptor pair separation. Since the electron is shared by the donor-acceptor pair, it is irrelevant to say what fraction of ΔE modifies the ground state of either of the two impurities. This is similar to the exciton case, where the binding energy of the exciton could be divided between an electron state and a hole state and refer those binding energies to the appropriate band edges. In the case of a donor-acceptor pair, it is convenient to consider only the separation between the donor and the acceptor level. The energy of the emitted photon in a DAP transition is given by:

$$E_{SP}(r) = E_{GAP} - E_A - E_D + \frac{e^2}{4\pi\epsilon_0\epsilon_r R} \quad (1.10)$$

where E_D and E_A are the respective ionization energies of the donor and the acceptor as isolated impurities. Since the impurities are located at discrete sites in the lattice (e.g., substitutional sites), the distance R varies by finite increments. For nearest neighbors, R is smallest; for more distant pairs, R increases in ever smaller increments. Thus, the pair interaction provides a possible range of states: from E_D and E_A for a very distant pair (a negligible pairing) to states which may lie inside the conduction and valence bands for near neighbors such that $(e^2/4\pi\epsilon_0\epsilon_r R) > E_D + E_A$ [89].

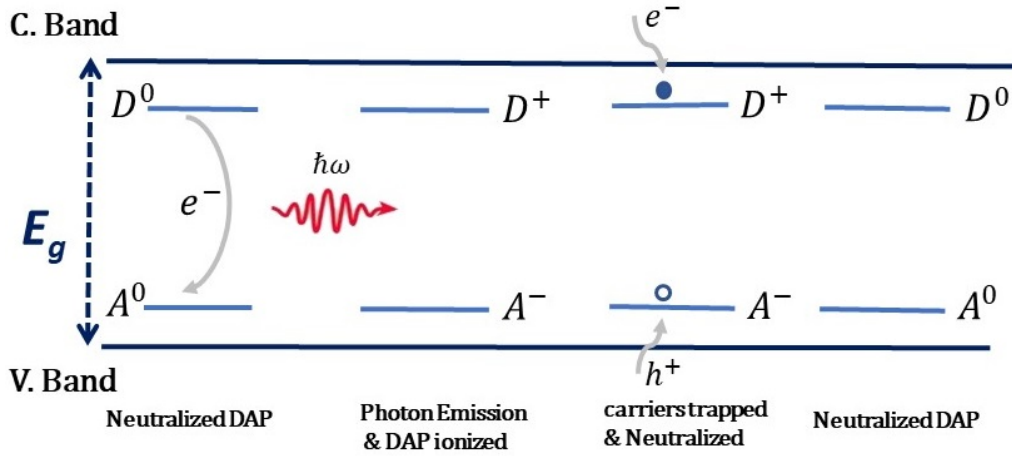


Figure 1.10: The process of a donor-acceptor pair transition.

In compound semiconductors, a difference can be formed based on the lattice site occupied by the impurities. Anions and cations create similar but distinct sublattices. Substitutional impurities can fit into either sublattice. If the donor and acceptor locate on the same sublattice, they create a type-I donor-acceptor pair (e.g., Si and Te on P-sites in GaP); if they occupy different sublattices, they form a type-II donor-acceptor pair (e.g., Zn on a Ga-site and S on a P-site in GaP) [90].

Figure 1.11 shows the geometry of the square lattice of the 2D perovskites with a sketch of the D^+A^- bound state, with the acceptor Ψ_A and donor Ψ_D , where R is the separation between both bound states.

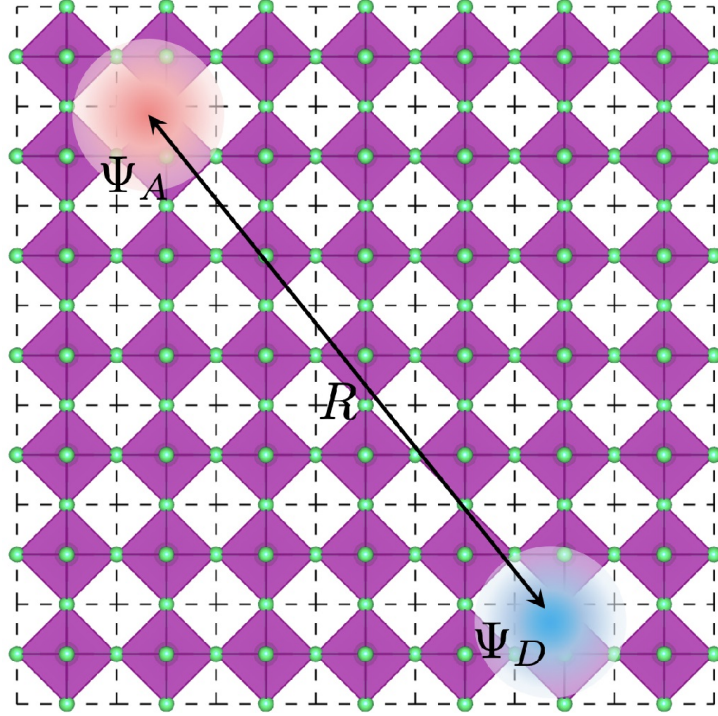


Figure 1.11: Scheme of the DAP binding complex states in a 2D perovskite lattice. R is the distance between donors and acceptors.

The Coulomb interaction energy between the ionized donor and acceptor end states is the last component in Equation 1.10. The distance between these defects decreases as the excitation power density increases, and the Coulomb interaction energy increases. As a result, when the excitation power density is increased the energy of the DAP recombination luminescence shifts to a higher energy [91], which is one of the characteristics of the DAP spectra [90–92]. Another characteristic of DAP pair bands is that the decay time of fluorescence increases with increasing pair separation. As a result, the high-energy emission decays faster than the low-energy emission, creating a shift of the band’s maximum to lower energies with time after excitation. Another distinguishing characteristic of DAP recombination is the redshift of emission energy as a function of time. The radiative recombination probability of an electron in a donor and a hole in an acceptor

depends exponentially on the distance between them, r as $\exp[-2(r/a_{DA})]$, where a_{DA} is the Bohr radius of the donor and acceptor. A closer DAP will recombine faster and emit at higher energy. Pairs separated by a greater distance will recombine with longer decay time, PL spectrum shifted toward lower energies [93]. A blueshift with increasing temperature is characteristic of DAP emission, as demonstrated by Urban et al. [93] and Tilchin et al. [94].

Fabry Perot Microcavity:

Controlling spontaneous emission (SE) is crucial from both a scientific and a technological standpoint. Traditional methods for enhancing spontaneous emission by changing the dielectric environment rely on resonant phenomena like cavity resonances, in which the spontaneous emission rate is increased throughout a small spectral range. Incorporating an out-coupling mechanism lowers the cavity's quality factor, resulting in a higher SE rate [67, 95].

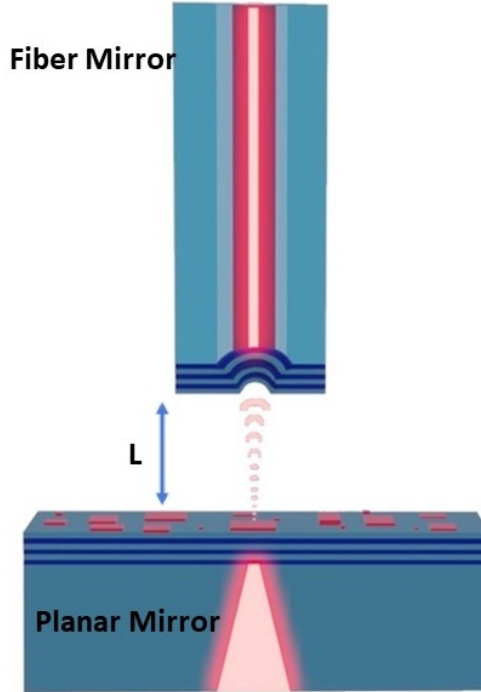


Figure 1.12: Scheme of Fabry-Pérot optical μ -cavity.

A Fabry-Pérot optical cavity confines light by using two highly reflective parallel mirrors. To interact with cavity photons, emitters can be deposited between these mirrors. To guarantee that the coupling rate between the optical field and the emitters surpasses the system optical and material losses, the electric field of the cavity mode must be maximized. To achieve this requirement, a cavity with a small effective mode capacity and a high quality or Q-factor is required. The effective mode volume (v_{eff}) is defined as the physical size of the cavity mode [68], given by:

$$v_{eff} = \iiint d^3r |\phi(r)|^2 = \frac{1}{4} w_0^2 \pi L \quad (1.11)$$

where $\phi(r)$ is the normalised electric field amplitude, w_0 is the cavity mode waist radius, and L is the cavity length. The **quality or Q-factor** is defined as the ratio of a resonant cavity frequency, ν , to the linewidth

(FWHM) of the cavity mode, $\delta\nu$:

$$Q = \frac{\nu}{\delta\nu} \quad (1.12)$$

The **cavity finesse**, is defined as the ratio of **free spectral range (FSR)** (the frequency separation between consecutive longitudinal cavity modes $\Delta\nu = \frac{2\pi c}{L}$) to the linewidth (FWHM) of a cavity mode. The finesse is shown as follows:

$$F = \frac{\Delta\nu}{\delta\nu} = \frac{\Pi\sqrt{R}}{1-R} \quad (1.13)$$

where R is the mirror reflectivity. To achieve appreciable coupling between the emitter and the cavity mode, the first is deposited inside the microcavity so that ideally it can overlap with an anti-node (maximum) of the cavity field. As a result, the electric field distribution inside the cavity is crucial to the design of the microcavity. In this thesis the transfer matrix method (TMM) [96–99], and COMSOL Multiphysics (Finite Element Method (FEM)) have been used to compute the electric field distribution (see Chapter 2, section Material and Method 2.5).

Purcell Factor and Spontaneous emission:

Embedding an emitter inside a microcavity can lead to additional effects due to the change in the optical density of states. When the quality factor of the resonant structure is not too high, the oscillator's resonance width is much larger than the spontaneous emission rate. The resonant structure then behaves, from the spin point of view, as a continuum, which means that when the emitter's linewidth is smaller than the cavity mode linewidth ($\delta\lambda_c$), in terms of the detuning between the emitter (λ_e) and cavity, the

emission lifetime, τ , modified from free space, (τ_0) , is described as follows:

$$\frac{\tau_0}{\tau} = F_P \frac{2}{3} \frac{|E(r)|^2}{|E_{max}|^2} \frac{\delta\lambda_c^2}{\delta\lambda_c^2 + 4(\lambda_c - \lambda_e)^2} + f \quad (1.14)$$

which is controlled by the Purcell factor given by

$$F_P = \frac{3}{4\pi^2} \frac{\lambda_c^3}{n^3} \frac{Q}{V_{eff}} \quad (1.15)$$

where n is the cavity's refractive index, V_{eff} is the effective volume of the mode, $E(r)$ is the field amplitude in the cavity, and $|E_{max}|^2$ is the maximum of its intensity. The constant f in Equation 1.14 describes the losses into leaky modes.

Prior to Purcell's research in 1946, the **spontaneous emission** was considered to be a radiative inherent characteristic of atoms or molecules. [100]. Purcell's study shown that the spontaneous decay rate of a magnetic dipole placed in a resonant electrical device was enhanced when compared to the free-space decay rate. Consequently, it can be deduced that the environment in which an atom is embedded modifies the radiative properties of the atom. A physical device with dimensions on the order of the emission wavelength λ is needed in order to observe this effect experimentally. The modification of spontaneous decay was not an obvious fact since most of the atomic transitions occur in or near the visible spectral range. In 1966, Drexhage studied the effect of planar interfaces on the spontaneous decay rate of molecules [101, 102], and the enhancement of the atomic decay rate in a cavity was later verified by Goy et al. [103]. However, it was also observed that the decay of excited atoms can be inhibited by a cavity [104]. Afterward, the modification of the spontaneous decay rate of an atom or molecule has been studied in various environments, including photonic crystals [105–108], and DBRs. Recent experiments of purcell factor

using Perovskites NCs [109, 110]

Weak and Strong coupling:

Weak coupling happens when the atom-cavity coupling constant g_0 is smaller than the loss rate because of either leakage of photons from the cavity (K) or decay to non-radiative modes (γ). This indicates that photons are lost from the atom-cavity system faster than the characteristic interaction time between the atom and the cavity. As with emission into free space, light emission by the atom in the cavity is irreversible. Since the effect of the cavity is relatively small in the weak coupling limit, it is appropriate to treat the atom-cavity interaction by perturbation theory [66].

Strong coupling requires that the atom-cavity coupling rate g_0 being greater than the cavity decay rate determined by the cavity lifetime as well as the non-resonant atomic decay rate. The interaction between photons in the cavity mode and the atom is reversible under these conditions. The atom emits a photon into the resonant mode, which is confined between the mirrors and can be reabsorbed by the atom faster than it is lost from the mode. Thus, the reversible interaction between the atom and the cavity field is faster than the irreversible processes caused by photon loss [66].

Two coupled oscillators model:

This is the model that describes the interaction of two bosonic modes. These bosonic modes can be electromagnetic field excitations (photons) or semiconductor excitations (excitons), but with the detail that excitons are not bosons but composite bosons, i.e., bosons made from two fermions. Then this is the simplest model for describing the interaction of a photon and an exciton, or two photons. Consider two mechanical oscillators with the same

mass and spring stiffness and a common oscillation frequency of ω_0 (labeled (a) and (b)). The oscillators are linked by an additional coupling spring (see Figure 1.13.A). The energies of the (a) and (b) oscillators are combined with the potential energy of the coupling spring, which is an element of the system Hamiltonian:

$$V_{ab} = m\omega_0 \frac{g}{2} (X_a - X_b)^2 \quad (1.16)$$

where X_a and X_b ($[X_a, X_b] = 0$) are the quantum operators for the two oscillator position, and these operators commute between them, and g is a coupling constant that depends on the stiffness of the coupling spring. For the purpose of simplicity, we assume $g \ll \omega_0$ and represent all quantities up to the first order in $\frac{g}{\omega_0}$.

We incorporate the components corresponding to X_a^2 and X_b^2 in the free-oscillator Hamiltonians by expanding the coupling energy V_{ab} , which corresponds to redefining the oscillator frequencies. They both become $\omega \approx \omega_0 + \frac{g}{2}$.

Then we have two oscillators with frequency ω coupled by the interaction potential energy $-m\omega g X_a X_b$ (we can neglect, to the first order, the difference between ω and ω_0). Where $X_a = (\frac{\hbar}{2m\omega})^{\frac{1}{2}}(a + a^\dagger)$, and $X_b = (\frac{\hbar}{2m\omega})^{\frac{1}{2}}(b + b^\dagger)$, calling a and b the annihilation operators associated to the renormalized oscillators, we can replace $X_a X_b$ in the coupling term with $(\frac{\hbar}{2m\omega})(a + a^\dagger)(b + b^\dagger)$, and the total Hamiltonian is:

$$H = H_a + H_b + H_{ab} \quad (1.17)$$

With:

$$H_a = \hbar\omega(a^\dagger a + \frac{1}{2}); H_b = \hbar\omega(b^\dagger b + \frac{1}{2}); H_{ab} = -\frac{\hbar g}{2}(a + a^\dagger)(b + b^\dagger) \quad (1.18)$$

There are four terms in the coupling Hamiltonian H_{ab} . Two of them, proportionate to ab and $a^\dagger b^\dagger$, represent transitions in which both oscillators lose or acquire an excitation quantum at the same time. These methods do not save overall energy. These anti-resonant elements can be ignored, leaving only the two others terms, hence the oscillator coupling is now:

$$H_{ab} = -\frac{\hbar g}{2}(ab^\dagger + a^\dagger b) \quad (1.19)$$

The last two terms, which combine an annihilation and a creation operator, depict a single quantum excitation between (a) and (b). An interaction term of this basic type describes any linear connection between two oscillators, regardless of their nature. As we will see shortly, our discussion is not limited to the mechanical case.

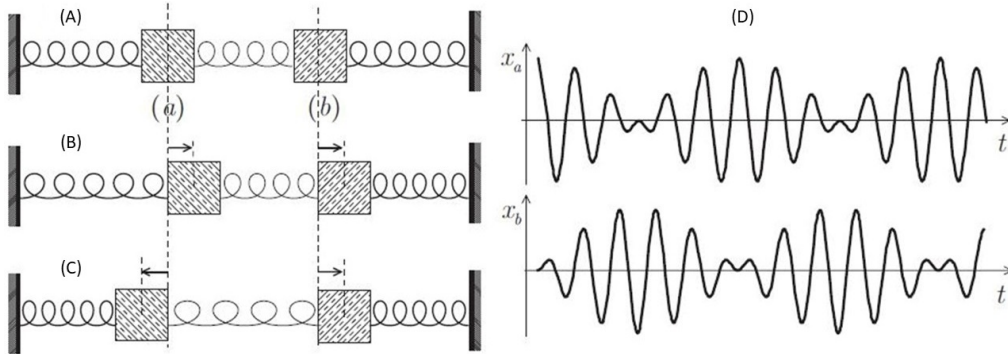


Figure 1.13: Two coupled mechanical oscillators. (A) Pictorial representation: two identical oscillators coupled by a spring. (B) Symmetrical eigenmode. (C) Anti-symmetrical eigenmode. (D) Classical beat signal for $g/\omega_0 = 1/6$, when the oscillator (a) alone is initially excited. Upper and lower traces: amplitudes for (a) and (b) respectively. [111].

It is easier to characterize the dynamics of this system by dividing it into independent sections and establishing new eigenmodes that combine

the dynamical variables (a) and (b). Let us define the symmetrical and anti-symmetrical superpositions of a and b as follows:

$$E_{LPM} = \frac{a+b}{\sqrt{2}}; E_{UPM} = \frac{a-b}{\sqrt{2}} \quad (1.20)$$

These combinations are real annihilation operators that obey the commutation relations of independent oscillators. They commute together and satisfy $[a_i, a_i^\dagger] = 1$ for $i=1, 2$. The total Hamiltonian is as follows:

$$H = \hbar(\omega - \frac{g}{2})(E_{LPM}^\dagger E_{LPM} + \frac{1}{2}) + \hbar(\omega + \frac{g}{2})(E_{UPM}^\dagger E_{UPM} + \frac{1}{2}); \quad (1.21)$$

The coupled oscillators develop as two separate systems with $\omega - \frac{g}{2} = \omega_0$ and $\omega + \frac{g}{2} = \omega_0 + g$ frequencies. The symmetrical mode (E_{LPM}) corresponds to an oscillation of the "center of mass" in which the two masses stay separated by a constant distance (see Figure 1.13.B). Because the coupling spring exerts no force, the oscillation frequency is ω_0 . The 'anti-symmetrical' mode (E_{UPM}) corresponds to a mass separation oscillation, leaving their center of mass stationary (see Figure 1.13.C). The coupling effect is therefore maximized, and the frequency is g higher than ω_0 .

The superposition of two eigenmodes with different frequencies gives rise to beats in the evolution of the system. An arbitrary initial condition generally corresponds to a superposition of eigenmodes. The position of each mass versus time is thus the sum of two oscillating functions at frequencies ω_0 and $\omega_0 + g$. This results in an oscillation at ω_0 with a modulated amplitude. This 'beat signal' is represented in Figure 1.13.D in the simple case where (a) is at $t = 0$ out of its equilibrium position and (b) is at equilibrium (both being initially motionless). In this beating process, the two oscillators

periodically exchange their energy. After half a beat period, $\frac{\pi}{g}$, (a) comes to rest, while (b) is taking over all the energy.

Avoided crossing:

We have demonstrated a and b as cavity modes. The cavity mode includes an effective mass (m) for the light, and this implies that we have a parabolic dispersion in K_{\parallel} , in the directions perpendicular to the confined modes. We assume mode b is larger than mode a, and we can tune the minimum energy of mode a. As a result, we can represent the crossing of these modes, and in the two coupled oscillator model, we will see an avoided crossing. This will be the signature of the two coupled oscillators in this system.

$$E_a(K_{\parallel}) = E_a + \frac{\hbar^2 k^2}{2m_a}, E_b(K_{\parallel}) = E_b(K_{\parallel} = 0) + \frac{\hbar^2 k^2}{2m_b} \quad (1.22)$$

The avoided crossing is a direct feature from strong coupling regime between two coupled oscillators. Figure 1.14 shows the two coupled oscillators model of anticrossing of lower photonic mode (LPM) and upper photonic mode (UPM) energy levels when tuning the energy a (E_a) across the energy b (E_b).

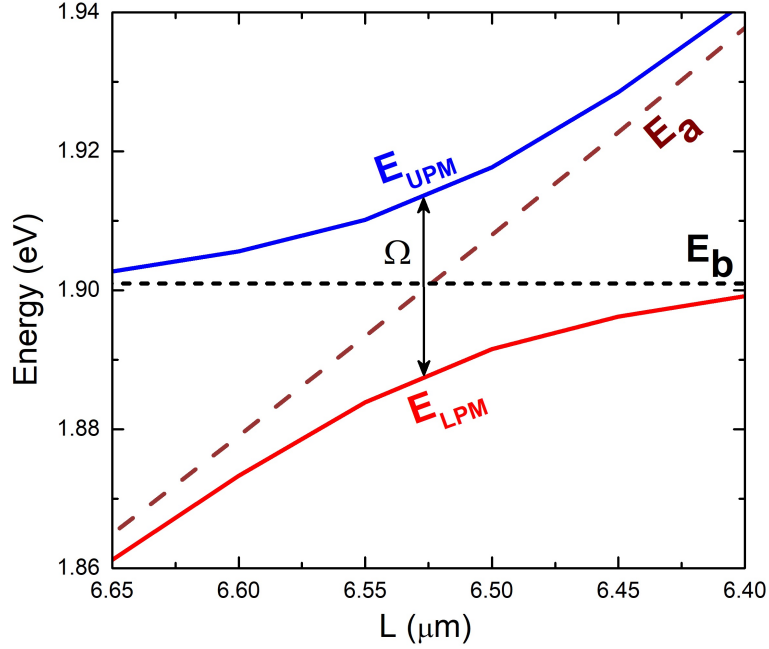


Figure 1.14: Anticrossing of LPM and UPM energy levels when tuning the cavity mode a, across the mode b energy.

The equation 1.23 is a two coupled oscillator model representing the UPM and LPM energy levels:

$$E_{UPM,LPM} = \frac{E_a + E_b}{2} \pm \sqrt{\Omega^2 + \left(\frac{E_b - E_a}{2}\right)^2} \quad (1.23)$$

When two optical modes are at resonance, $E_a = E_b$, LPM and UPM energies have the minimum separation $E_a - E_b = \Omega$, which is often called the normal-mode splitting in analogy to the Rabi splitting of a single-atom cavity system. Due to the coupling between this two modes, the new anticross happen when the energy a (E_a) is tuned across the energy b (E_b). This is one of the signatures of “strong coupling” (see Figure 1.14).

Chapter 2

Experimental Method

This chapter will provide a description of the experimental techniques used in the various research studies included in the thesis.

2.1 Sample preparation

Spin-Coating:

To cover the prepared sample with polymethylmethacrylate (PMMA) using a common and simple technique coined as spin-coating [112–114]. It entails basically depositing a drop of a material dispersed in solution (in this example, PMMA) on the sample and spinning it to cover the whole surface with a thin film of the needed material. Figure 2.1 depicts the spin-coating device, together with a hot plate to evaporate the solvent of the samples (dry) after deposition and spinning. In the spinning device the substrate is held by means of a vacuum the PMMA solution with a precisely controlled concentration is dropped at the center of the substrate and the spinner. The final thickness of the layer is controlled by modifying the rotation velocity and the solvent concentration.

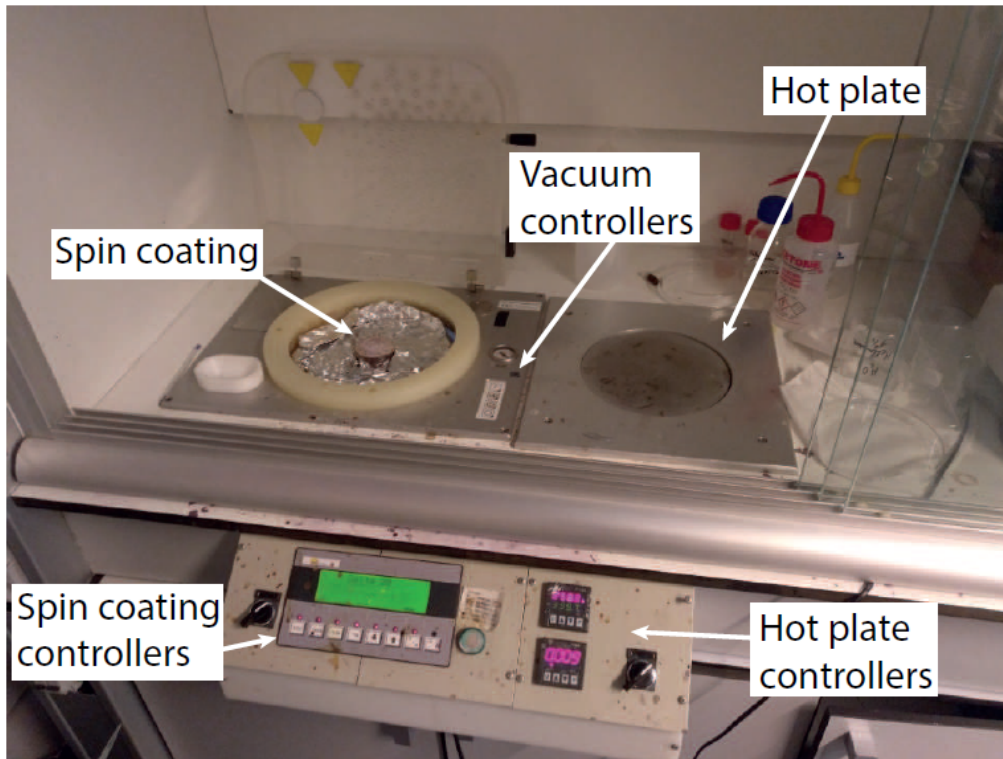


Figure 2.1: The spinning mechanism on the left of the image protected with aluminum foil to prevent dirt from accumulating on the device while it spins. On the right, there is also a hot plate.

Immediately after completing the spinning, we bake the sample at 80°C and 150°C for two minutes at each temperature [112]. The first bake will entirely evaporate the solvent, and the second will produce PMMA polymerization.

Dip coating:

Dip coating is the process of immersing a substrate in a tank with a solution of a material, withdrawing the piece from the tank, and allowing it to dry. The coated piece can then be dried by force-drying or heating. It is an effective approach for preparing samples for single NC measurements since, in these types of experiments, it is necessary to spread quantum emitters on the substrate spatially isolated from each other. The control of dipping

time and the concentration of the colloidal solution determine the dispersion of quantum emitters on the substrate. In addition, dipping tanks can be any shape and size to match the substrate dimension to be coated.

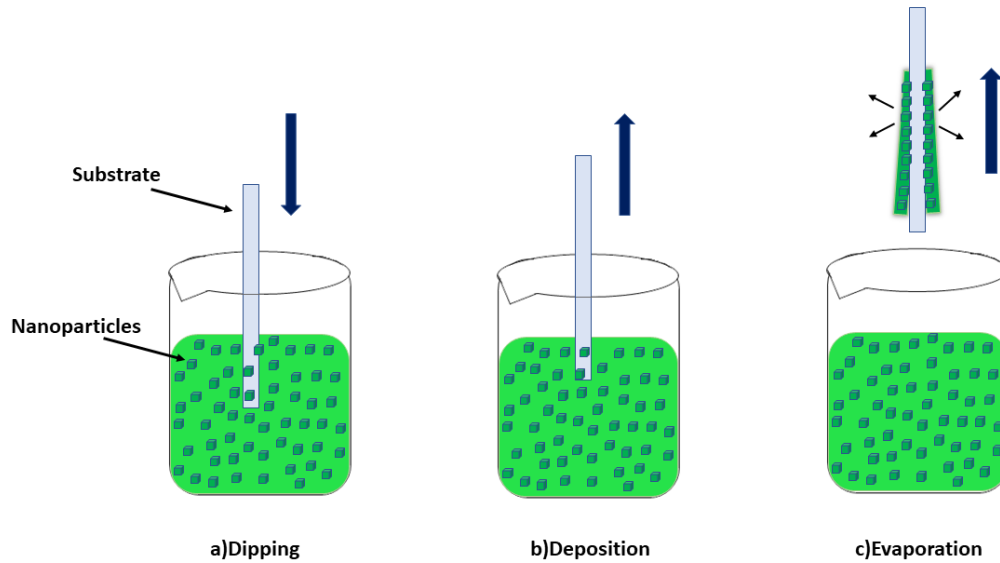


Figure 2.2: Process of dip coating is shown schematically.

The dip-coating process can be divided into the three steps, as shown in Figure 2.2:

- Immersion: the substrate is submerged in the coating material's solution.
- Dwell time: the substrate needs to be completely submerged and motionless to allow for the coating material to apply itself to the substrate.
- Withdrawal: To avoid vibration, the substrate is removed at a constant speed. The quicker the substrate is removed from the tank, the more material will be deposited on to the substrate.

Mechanical exfoliation:

Mechanical exfoliation is one of the most known techniques to obtain high optical quality 2D samples, with sample thickness up to the monolayer (ML). It is a top-down technique, based on the difference in the strength between the weak interlayer van der Waals (vdW) bonds and the strong intralayer covalent bonds in the laminar structure.

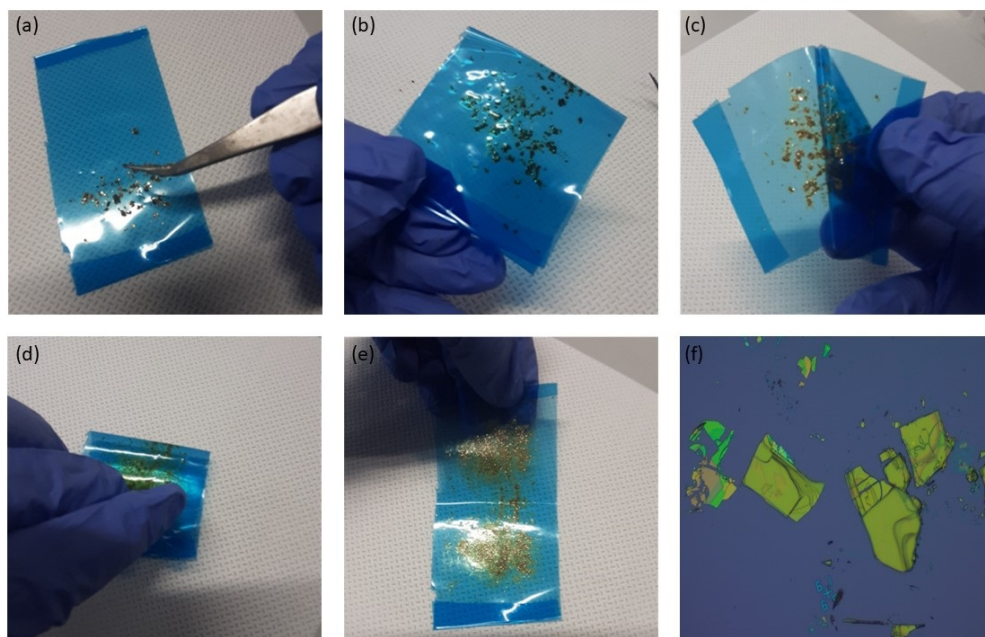


Figure 2.3: (a-e) Mechanical exfoliation from the bulk material to the single monolayer of 2D perovskite obtained in the substrate, (f) images of 2D perovskite nanosheets from optical microscope.

In this process, a bulk layered crystal (2D-perovskite in this case) is deposited on a scotch or adhesive tape and is gently peeled off several times in the tape, being folded repeatedly against itself. Due to the weaker vdW interlayer bonds, in each exfoliation the peeled off material separated from the bulk source will be thinner, obtaining eventually up to few MLs of the original material. The more times the material is exfoliated, the 2D perovskite nanosheets obtained will be thinner, at the cost of losing lateral size

of the final nanosheet. There is no a recipe for the ideal number of times or pressure to apply in each exfoliation; it depends on the material to be exfoliated. Blue Nitto Tape was used to minimize the amount of remaining adhesive residues in the exfoliated nanosheets. Finally, once the material has been exfoliated on the tape, the last exfoliation will be performed between the tape and the target substrate to randomly transfer or re-exfoliate the nanosheets from the tape to the substrate. (See Figure 2.3.a-e). Figure 2.3.f shows an optical microscope image of a nanosheet of a 2D (n=1) perovskite after mechanical exfoliation.

2.2 Optical Characterization

2.2.1 Optical microscopy

Optical microscopy is a technique for closely checking a sample using a magnifying lens and visible light. An optical microscope, often known as a light microscope, uses visible light to magnify images of small materials through one or more lenses. The lenses are positioned between the sample and the viewer's eye to magnify the image and allow for a more detailed examination. To do this, we used a Zeiss Axio Scope.a1 microscope with an Axiocam ERC 5s camera (Figure 2.4). The microscope contains numerous lenses ranging in magnification from 10X to 100X, allowing it to take high-resolution images at various magnifications, as demonstrated in the right panels of Figure 2.4 images of hBN flake.

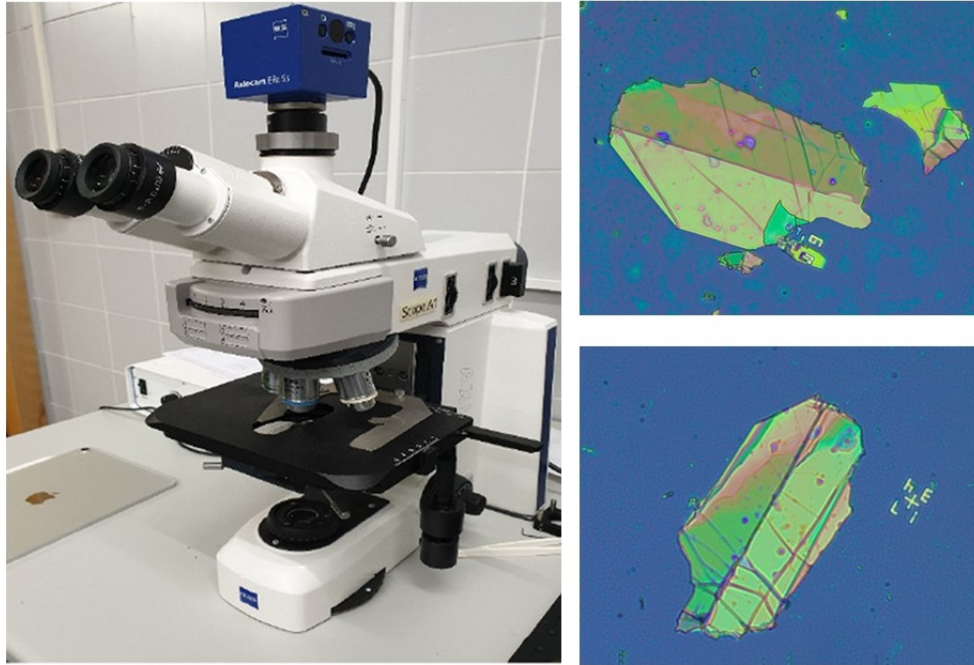


Figure 2.4: On the left, a Zeiss microscope, which is commonly used for the optical identification of the hBN flake. On the right, two pictures from hBN transposed onto samples with single PNCs captured under magnification.

2.2.2 Confocal micro-PL and micro-TRPL

Marvin Minsky invented the confocal microscope while he was a post-doctoral student at Harvard University in 1955. [115]. In 1961, he received a patent for his concept (Figure 2.5 (Top panel)). For a long time, his invention was ignored until sufficiently powerful light sources were developed and calculation tools for dealing with large amounts of data were created. Based on Minsky's work, M. David Egger and Mojmir Petran created a multi-beam confocal microscope in the late 1960s. In the late 1970s, Colin Sheppard developed an imaging theory within the theoretical framework, and in his article "Image generation in the scanning microscope," Sheppard coined the word "confocal" [116]. During the 1980s, Tony Wilson, Brad Amos, and John White continued to make contributions to the field of con-

focal microscopy (Figure 2.5 (Down panels)), and the first commercially accessible apparatus was released in 1987.

This microscopy provides various advantages over traditional microscopy, including optical sectioning, less scattered light, and increased microscope resolution. These effects are mostly caused by the use of spatial filtering methods to reduce light generated outside the focus. [117, 118].

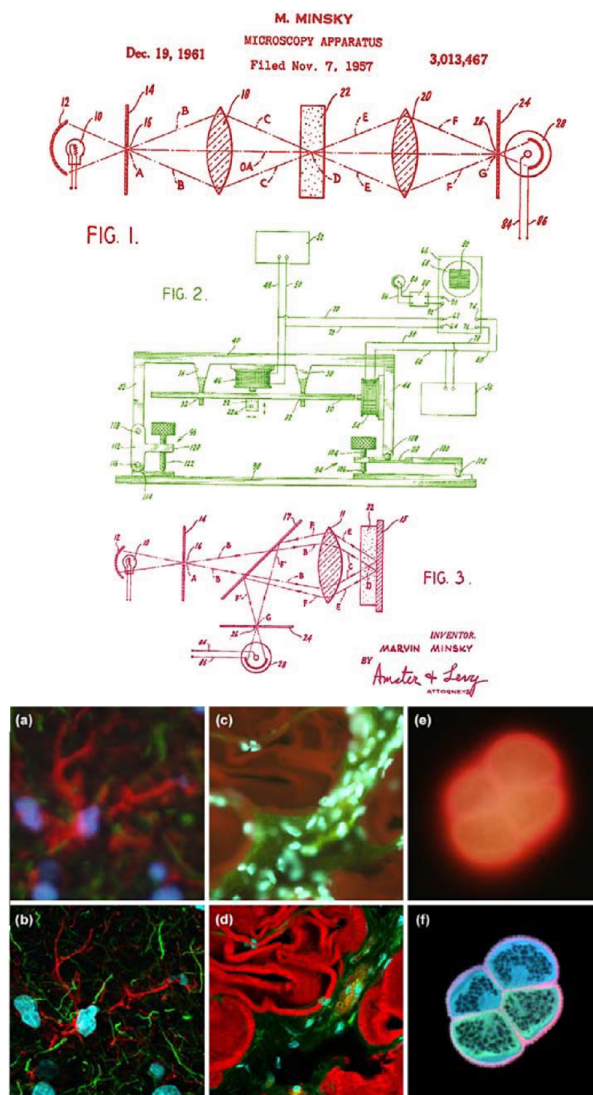


Figure 2.5: (Top), Schematic of the first confocal microscope described in the Minsky patent. (Down), A confocal microscopy ((b), (d), (f)) and traditional microscopy ((a), (c), (e)) on biological specimens were compared. [119] is the source of the graph.

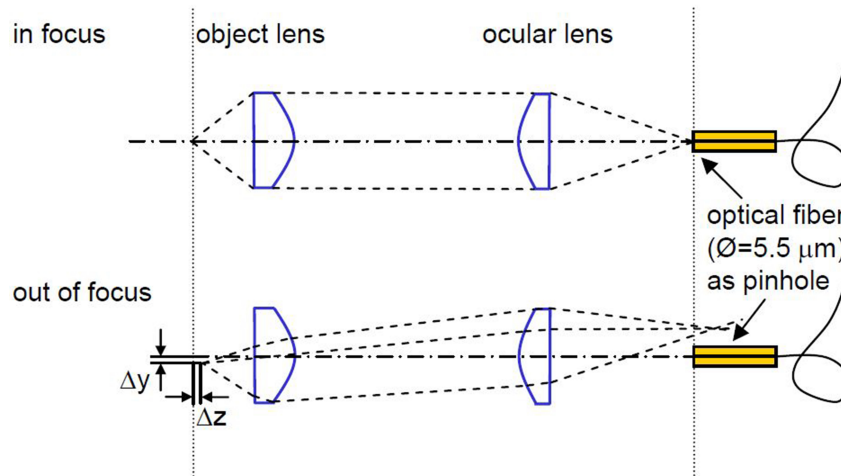


Figure 2.6: A fiber-based confocal objective is depicted schematically. An optical fiber couples the illuminating light to the objective. With the aid of an ocular lens, the diverging light leaving the fiber is collimated. An objective lens is then used to focus the parallel light beam on a diffraction-limited spot in the focal plane of the lens (upper drawing). The entire amount of light that is emitted or reflected from the focal point into the solid angle of the objective lens follows along the same path as the illuminating light back into the fiber core before being returned to the analyzing setup. Any light coming from an out-of-focus source won't be imaged onto the fiber core, so it will not be coupled into the fiber and will not be visible by the analyzing setup (lower part). The fiber core acts as a pinhole. Graph adapted from [120].

The fundamental concept for an optical fiber-based confocal microscope is depicted in Figure 2.6. The idea is to introduce a pinhole into the image plane of an objective. The objective is made up of two lenses that are aligned such that the focal area of one lens, the object lens, is imaged by the second lens, the ocular lens, onto a pinhole. The pinhole in the system depicted in Figure 2.6 is made up of the $5.5 \mu\text{m}$ diameter core of a single-mode optical fiber. The only light that couples into the fiber and can be directed out of the microscope to the analyzing setup is the light that hits the fiber core at the solid angle provided by the fiber's NA. The light emitted by the sample from the confocal setup's focal region is imaged alongside the fiber core (lower sketch of Figure 2.6). As a result, it is not effectively coupled to the fiber. Because of this, confocal microscopes

have better spatial resolution than traditional optical far-field microscopes [121]. The confocal microscope's diffraction-limited resolution, on the other hand, means that the sample cannot be imaged at the same time. At a time, only light from a single point is detected. Scanning can provide a three-dimensional image of the sample. Figure 2.7 shows how inspection volumes are lowered, making this approach an ideal candidate for the study of isolated NCs.

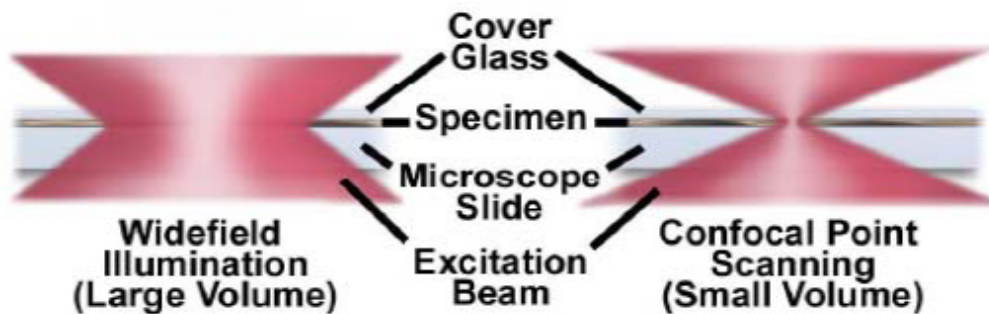


Figure 2.7: Volumes of investigation in conventional and confocal microscopy, graph adapted from [122].

Airy Disc:

To understand the basis and benefits of confocal microscopy, basic diffraction theory ideas must be reviewed. The electromagnetic field creates an amplitude distribution on the image plane when a point source of light passes through the microscope system (apertures, lenses, etc.). This is represented as an amplitude diffraction pattern, and the image of this pattern corresponds to the PSF (point spread function, or intensity point spread function). When the openings are circular, the Airy disk describes the intensity distribution of the PSF in the plane of focus. This distribution has an intensity maximum in the center and a series of maximums separated by zero intensity areas in ideal optical systems. The PSF distribution is depicted in the Figure 2.8 at various distances from the focus, with the image

in the center corresponding to the Airy disk.

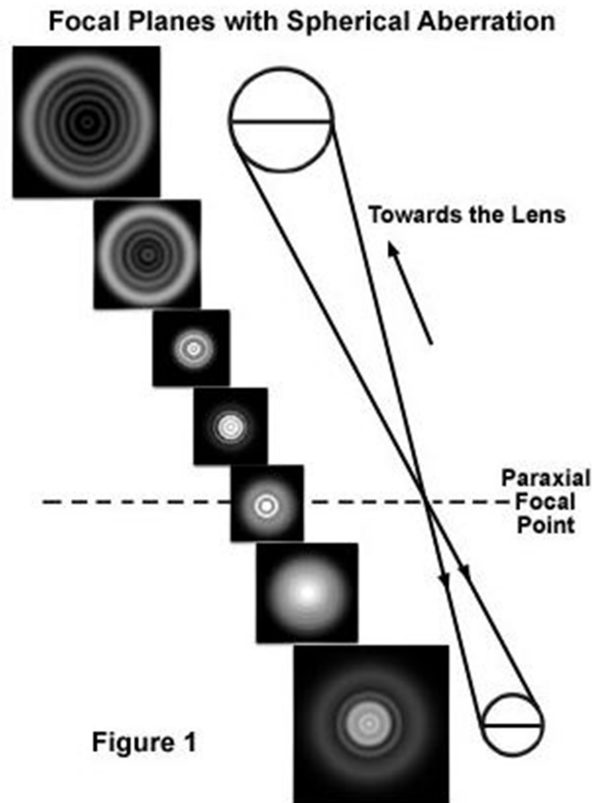


Figure 2.8: The PSF is depicted as a function of focus distance. Each image is captured on a plane perpendicular to the focal plane. The Airy disk is represented by the image captured in the focal plane. Because the center of the image in focus is 100 times brighter than the rest, the intensity has been manipulated. Graph adapted from [123].

Resolution criteria:

The resolution between two objects is defined as the shortest distance between them at which both can be clearly recognized. As a result, the lateral resolution will correspond to the width of the PSF peaks. There are several factors that determine the highest resolution of a system. According to Rayleigh's criteria, two objects are laterally resolved when the distance between them equals the distance between the first minimum of one's airy disk and the center maximum of the other (see Figure 2.9). In this approach, the

ideas of resolution and contrast are inextricably linked, and the influence of noise will be important for achieving good resolutions. A similar approach can be used to estimate the axial resolution of the system [119, 123].

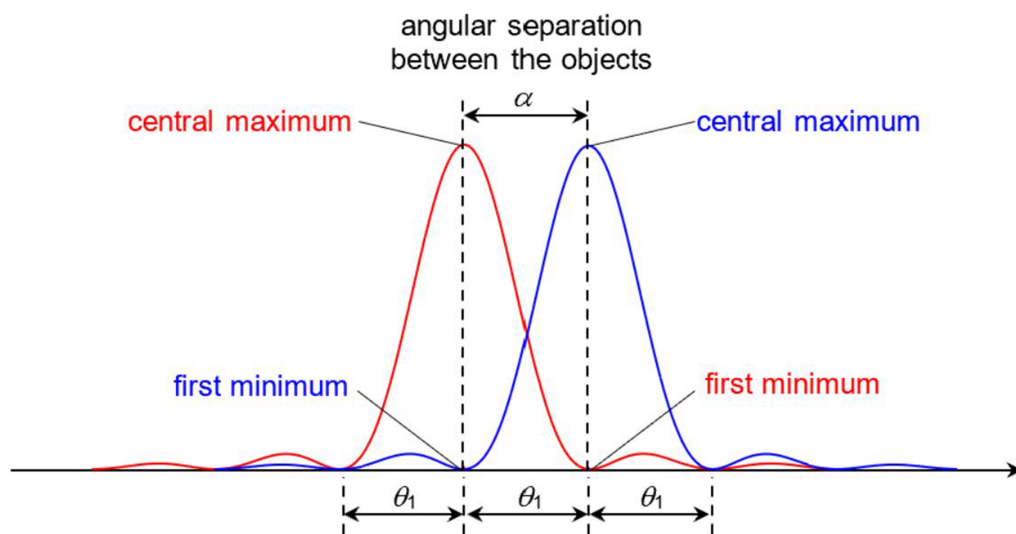


Figure 2.9: Rayleigh criteria for the highest optical resolution between two nearby objects.

Thus, for conventional microscopy, the lateral resolution according to the Rayleigh criterion will be given by the expression:

$$\Delta r_{lat.} = 0.6 \frac{\lambda}{NA} \quad (2.1)$$

where NA is the numerical aperture, and the λ is the wavelength of the light.

Resolution in the confocal microscope:

Confocal microscopy uses optical components that improve resolution. As previously stated, the system's PSF will describe the distribution of light over the volume under consideration. Nevertheless, the same function defines the intensity distribution of the observed volume in the confocal system; therefore, if the same optics are used or if the reflection configuration is utilized, the $PSF_{conf.}$ will be represented by:

$$PSF_{conf.} = PSF \times PSF = PSF^2 \quad (2.2)$$

As predicted, the $PSF_{conf.}$ has a narrower intensity distribution (Figure 2.10), signaling that this type of instrument's resolution will be enhanced. When compared to traditional microscopy, the lateral extension of PSF in fluorescent confocal microscopy investigations is reduced by around 30% [122]. The lateral resolution expression in the confocal arrangement is as follows:

$$\Delta r_{lat.(conf.)} = 0.4 \frac{\lambda}{NA} \quad (2.3)$$

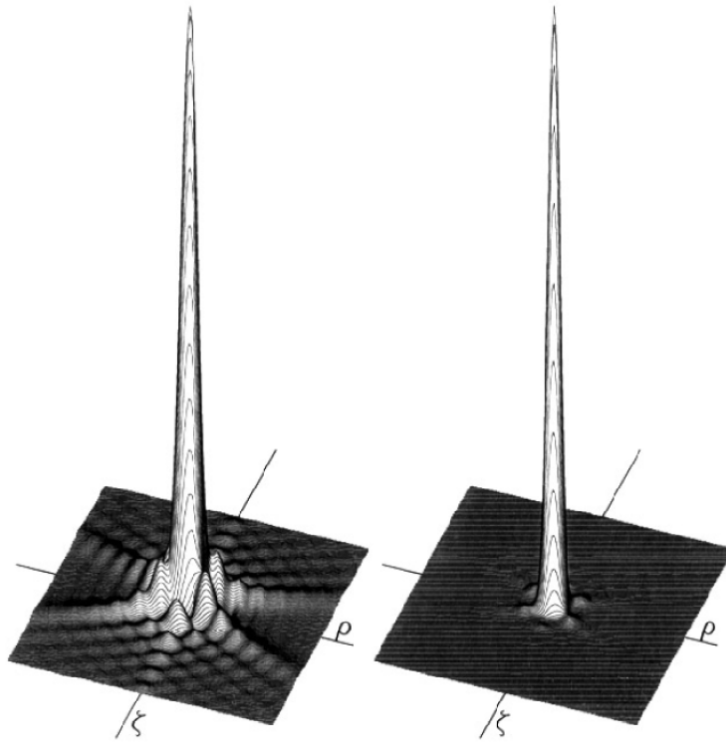


Figure 2.10: PSF under conventional (a) and confocal (b) microscopy. The graphics are represented in optical units (ξ , y , ρ), which are often designated with the letters (u , y , v), respectively. The graph was adapted from [123].

It should be noted that in order to utilize high-quality confocal microscopy, the radius of the pinhole must be small enough (below the Airy disk in the plane of the pinhole), but anything less than a certain value results in a drop in signal intensity without an increase in resolution. The ideal value for each assembly must be determined by the required resolution and intensity levels [124]. The paraxial approximation is used to characterize the assumptions in this section, which is satisfied only under certain conditions (NA less than 0.6 [125]).

Confocal fluorescence microscopy setup:

Low temperature measurements were carried out using a confocal microscope (Figure 2.11.a), where the samples were held in the cold-finger of a

vibration-free closed-cycle cryostat (AttoDRY800 from Attocube AG) that can be cooled down to 4K.

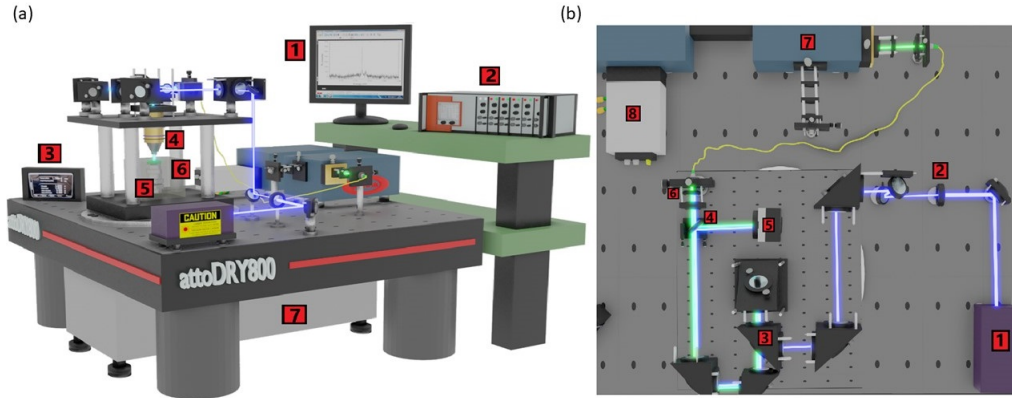


Figure 2.11: Experimental setup (a) A schematic picture of the confocal fluorescence microscopy set-up with which the low temperature (4K) measurements were done in isolated perovskite NCs, Some of the setup elements are: 1-Spectra Monitoring, 2-Piezoelectric motors controllers, 3-Temperature & Vacuum monitoring, 4-Microscope objective, 5-Piezoelectric motors, 6-Vacuum chamber, 7-Cooling system (b) Top view of the low temperature confocal microscope set-up: 1-The laser source, 2-Filters set, 3-Beam sampler, 4-Beam splitter, 5-Camera, 6-Long pass filter, 7-The spectrograph, 8-CCD camera.

μ -PL was excited by means of a continuous wave (CW) laser diode at a wavelength of $\lambda = 405, 532, 650, 785$ nm. Additionally, the collection and excitation arms were independently aligned by using single-mode fiber-coupled laser diodes at selected wavelengths in order to simulate the optical emission from the different sets of samples. The cores of the single mode optical fibers in detection will define the corresponding confocal pinholes. Excitation and detection are performed through the same long-working distance $50\times$ microscope objective (378-811-15) from Mitutoyo, which was mounted outside the cryostat ($NA=0.42$). The emission from NCs was long-pass filtered, dispersed by a double 0.3 m focal length grating spectrograph (Acton SP-300i from Princeton Instruments) and detected with a cooled Si CCD camera (Newton EMCCD from ANDOR) for recording μ -PL spectra.

In the cryogenic μ -PL setup (Figure 2.11.a), the 405 nm CW laser diode

was used to excite both green and red emitting NCs (1-label in Figure 2.11.b). Parallel mirrors cross a set of neutral filters and a beam sampler (with just 4% reflectivity) to send laser light to the setup's excitation arm, which determines the excitation power from mW to tens of pW (2, 3 labels in Figure 2.11.b). The pump laser beam is incident normally on the sample surface, which is mounted on an Attocube piezoelectric XYZ motor within the cryostat. Before collecting the emitted PL via the single-mode fiber, a Pellicle beam splitter (50:50) is used in the collection arm (4-label in Figure 2.11.b) to construct a image of the sample surface using a C-MOS camera (5-label in Figure 2.11.b). A 450 nm long-pass filter (6-label in Figure 2.11.b) was used to block the pumped laser and transmit emitted light to the double spectrograph (7-label in Figure 2.11.b), and the 8-label in Figure 2.11.b shows the CCD camera.

2.2.3 Photon correlation (Hanbury Brown and Twiss Setup):

To experimentally measure the photon time distribution, we must have some way of recording the arrival times of the emitted photons. The Hanbury Brown and Twiss (HBT) technique is a straightforward and robust technique for measuring photon distribution by the statistics of photon coincidences. This technique employs a 50/50 beam splitter to divide the photon stream into two branches which are guided onto two separate APD detectors operating in the photon counting mode. To start the timer and stop it, one APD starts it, and the other APD stops it, using TCSPC (Time correlated single photon counting) technique, that measure the interval between detection events (see Figure 2.12). The time period or delay of the detection coincidences is binned in absolute time delay values, with only the

APD time resolution and electronic jitter limiting the minimum detection window and thus ultimate time precision. In order to extract useful information from this measurement by means of the second order correlation function $g^{(2)}(0)$, the coincidence counts at $\Delta t=0$ is compared to coincidence counts for $\Delta t \rightarrow \pm\infty$.

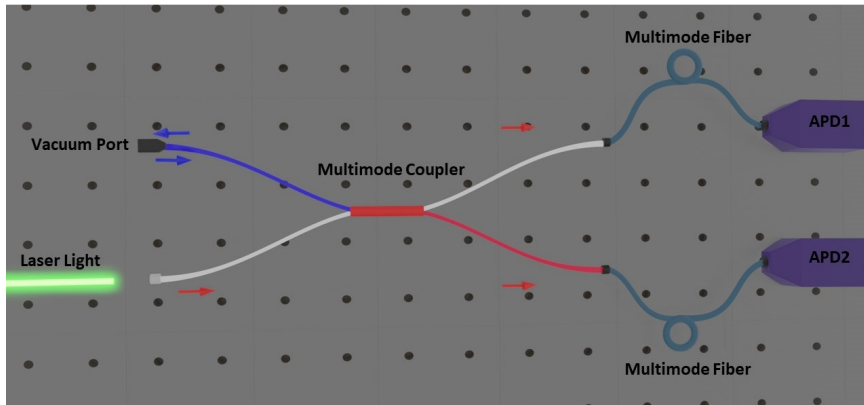


Figure 2.12: Schematic representation of Hanbury Brown and Twiss experimental setup using fiber beam splitter.

2.2.4 Open access Microcavity setup

Distributed Bragg Reflectors (DBRs) are commonly used to achieve the extremely high reflectivity mirrors required for Laser cavities. DBRs are made up of two alternating dielectric materials with thicknesses of $d_i = \lambda_0/4n_i$ ($i=1, 2$), where n_i is the refractive index of dielectric layer i ($i = 1, 2$), and λ_0 is the wavelength of light. The DBR works on the thin-film interference principle [126], and by properly selecting the thickness of the layers, all the reflected light will constructively interfere. As a result, practically most of the light is reflected back into a cavity mode of two DBR mirrors. This, however, only happens in a region around λ_0 called the stopband, which is a function of the number of paired layers (see Figure 2.13.d). To achieve good coupling between the emitter and the cav-

ity mode, the first is deposited inside the microcavity so that it overlaps with an anti-node (maximum) of the cavity field. As a result, the electric field distribution inside the cavity is pivotal to the design of the microcavity. The transfer matrix method [96–99], and COMSOL Multiphysics (Finite Element Method (FEM)) can be used to compute the electric field distribution.

There are two critical components of the system: the fiber DBR mirror and the planar DBR (see the scheme in Figure 2.14.c). The optical fiber that we chose for the fiber DBR patterning is single mode, copper coating fiber with a wavelength range of 460-600 nm with a mode field diameter of $6 \mu\text{m} \pm 0.5 \mu\text{m}$. This fiber is sourced from IVG Cu450 [127]. The Radius of Curvature at the center of the concave impression of the set of fiber mirrors used in these experiments was $R = 100 \mu\text{m}$. The second crucial component, is the planar DBR consisting of 13 paired layers of Diniobium pentoxide (Nb_2O_5) and Silicon dioxide (SiO_2) with the center wavelength of the stopband at 530 nm. Figure 2.13.a shows three planar DBRs, with the green one has containing a film of CsPbBr_3 NCs deposited on top by spin coating. All three are illuminated with ultraviolet light, in order to observe the PL of the NCs. The reflectivity of each DBR mirror, which is determined by the number of pair repetitions and the refractive index difference between the two dielectric materials used, determines the finesse of the cavity. Figure 2.13.b shows how the theoretical finesse is strongest between 480 and 620 nm. Figure 2.13.c&d. shows the refractive index and reflectivity of the planar DBR, respectively, and Figure 2.13.e&.f show the refractive index and reflectivity of the fiber DBR, respectively. The alternate layer configuration produces a periodic refractive index contrast that is specifically designed to maximize the electromagnetic field at the

surface of the DBR, where the semiconductor material will be deposited, and reduce it in the center (see Figure 2.13.c). Figure 2.13.e depicts the DBR refractive index graph of the end of the fiber and the field intensity. The index contrast is designed to have a minimum field intensity at the end of the fiber. Figure 2.13.d&.f shows The calculated stopband function with 13 paired layers of Diniobium pentoxide (Nb_2O_5) and Silicon dioxide (SiO_2) at 530 nm for a planar DBR and fiber DBR, respectively. The blue curve represents the cavity's reflection efficiency. The stopband is a large high reflectivity window centered at 530 nm. In principle, increasing the number of layers increases the reflectivity of the cavity.

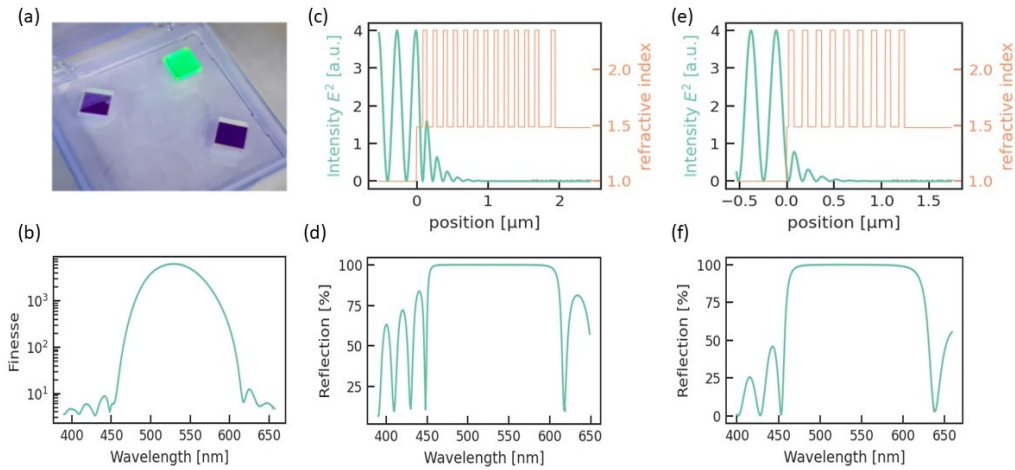


Figure 2.13: (a) Three DBRs, the green one has CsPbBr_3 NCs deposited on top by spin coating. All three are illuminated with ultraviolet light. The photoluminescence of the NCs can be seen when it is irradiated. (b) Theoretical models of fiber finesse. (c) The planar DBR's periodic refractive index profile is depicted (red), together with the field intensity (green). (d) reflection of planar DBR's (e) The fiber DBR's periodic refractive index profile is displayed (red) together with the field intensity (green). (f) reflection of fiber DBR's. All the modeled plots are produced and delivered by the manufacture company [127].

The fiber is glued to a top metal block which has a trapezoidal shape by means of a silicon V-groove and connects to the piezoelectric motors. Light is collected via objective 20X with the $\text{NA}=0.6$ (see Figure 2.14.a.). We used

a 20X objective with a 0.6 numerical aperture instead of a 50X (NA=0.42) objective to collect more signal. Because the signal was too weak in the room temperature measurements in the cavity setup for some samples, and a greater numerical aperture is needed to increase the collected signal. The fiber is allowed to protrude approximately the diameter (125 μm) of the v-groove and Titanium holder which is shown in Figure 2.14.b. This has the main advantage of keeping the fiber tip clean, allowing the shortest cavity (see Figure 2.14.c), and at the same time reducing the possible vibrations at the fiber tip. The planar DBR is screwed to a holder so that the DBR is facing downwards to the upward-facing fiber mirror.

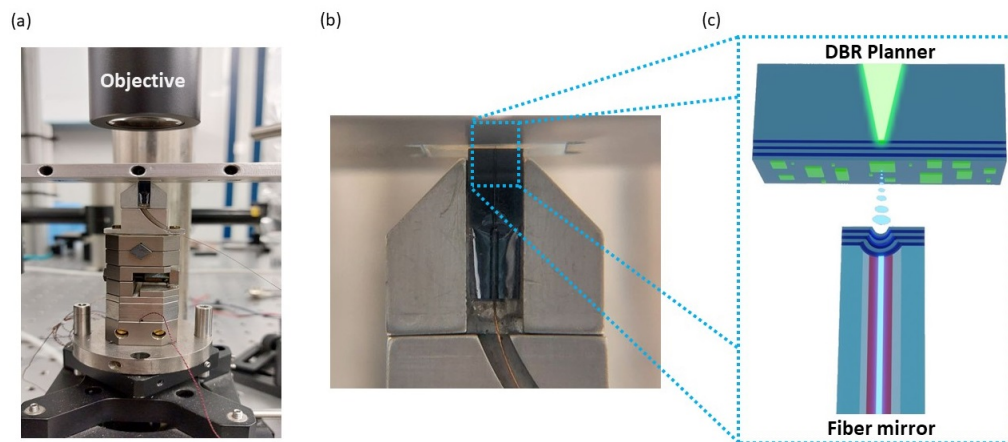


Figure 2.14: (a) The fiber mirror is glued vertically into a Titanium mounting block (trapezoidal piece) using a Silicon V-groove. This mounting block is placed on a vertically moving Attocube nanopositioning piezo stage. The planar DBR is screwed to a holder that can move in the XY plane. (b) Depicts a magnified view of the fiber mirror approaching the planar DBR. (c) shows a scheme of machined fiber tip with a concave DBR mirror coating substitutes one of the integrated, semi-conductor DBR mirrors in the fiber microcavity architecture.

2.3 Scanner micro-PL map at low and room temperature

We utilized Qudi [128] python open source module to program the μ -PL map measurements, which is a broad, modular, multi-operating system suite developed in Python 3 for controlling laboratory experiments. It creates an organized environment by separating functionality into hardware abstraction, experiment logic, and user interface layers. The primary feature set includes a graphical user interface, live data visualization, distributed execution via networks, fast prototyping through Jupyter notebooks, configuration management, and data recording.

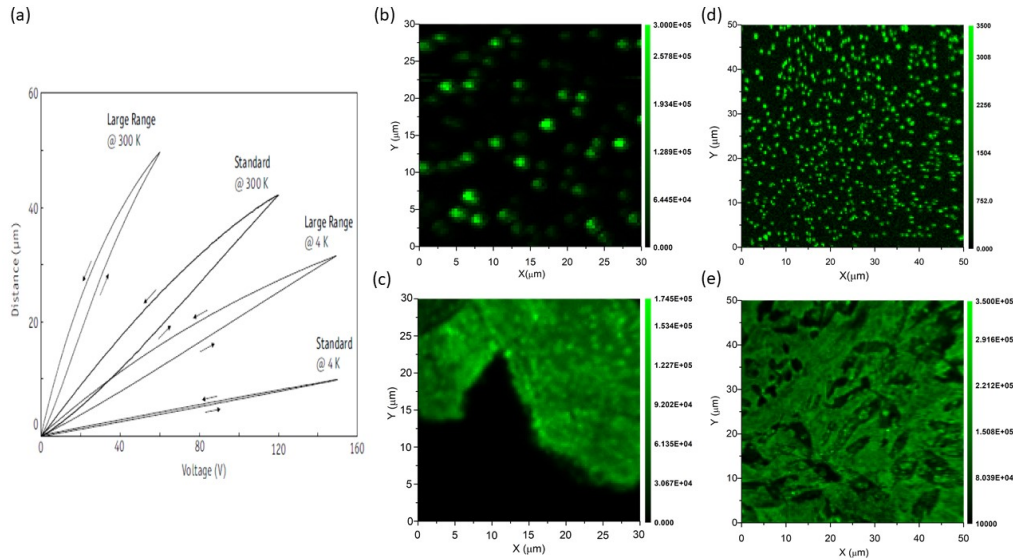


Figure 2.15: (a) Hysteresis curves of different ANSxy100 scanners. μ -PL map of single CsPbBr₃ PNCs (b), and a 2D TEA₂SnI₄ perovskite thin film (c) at low temperature. μ -PL map of a composite of MAPbBr₃ nanoparticles (NPs)(d) and a MAPbBr₃ thin film (e) at Room temperature.

μ -PL mapping was carried out using our fiber-based scanning confocal microscope (see Figure 2.11), with the samples placed in a vibration-free closed-cycle cryostat (AttoDRY800 from Attocube AG). As can be seen

in Figure 2.15.a, the maximum scan range of the piezo electric stage reduces with temperature from $\sim 50 \mu\text{m}$ at room temperature to $\sim 30 \mu\text{m}$ at low temperatures (4K). In terms of the scanning range changes at different temperature of the "LargeRange" Piezomotor scanners, the scan range at 4K would be $30 \times 30 \mu\text{m}$, and it increases up to $50 \times 50 \mu\text{m}$ at 300K. Figures 2.15.b&c represent a μ -PL maps of single CsPbBr₃ NCs, and a 2D TEA₂SnI₄ perovskite thin film, respectively at 4K. While Figure 2.15.d&e shows the μ -PL map of a composite containing nanoparticles (NPs) of MAPbBr₃ and a thin film of MAPbBr₃ at 300K. The PL intensity is shown by the color coded μ -PL maps. The μ -PL intensity of the emitters is zero in dark zones, while it grows in the green zone from dark green to light green. In this thesis, making a complete μ -PL map of a sample is very useful before beginning point measurements; for example, when studying the μ -PL of single perovskite NCs, mapping helps to recognize isolated single nanocrystals. In the case of 2D flakes, it is also useful for studying non-uniform PL emission due to sample morphology.

2.4 Transmission Electron Microscopy:

The transmission electron microscopes (TEM) can magnify objects up to 2 million times and is capable of achieving atomic (sub-angstroms) spatial resolution. [129, 130].

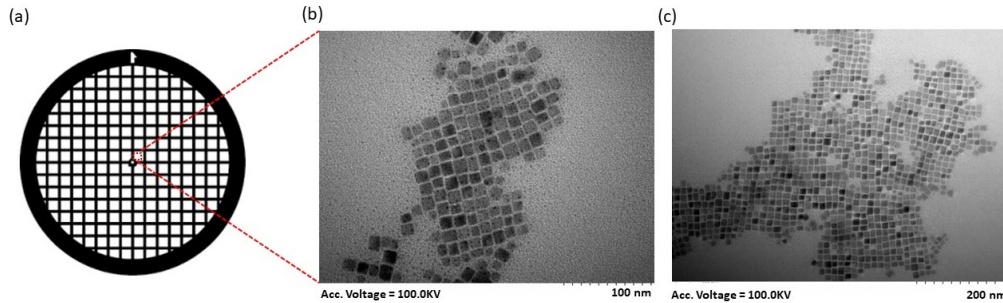


Figure 2.16: Transmission Electron Microscopy (TEM) image was measured by a JEOL 100 kV microscope, model HT7800 Series, in a copper grid (a) in which the colloidal material was dropped. The resolution of (b) is 100 nm and (c) 200 nm.

TEM can only load thin samples (<150 nm) and requires special preparations. In this thesis, we use the TEM to investigate the morphology and size distribution of the NCs with the HT7800 RuliTEM at 100 kV, in a copper grid where the colloidal suspension of Material was dropped (see Figure 2.16.a). A TEM image is shown in Figure 2.16.b with a scale rule of 100 nm and in Figure 2.16.c with a scale of 200 nm.

2.5 Numerical Methods

Transfer matrix method:

The transfer matrix method is used to determine the reflection and transmission characteristics of multi-layered structures [131, 132]. Imagine a plane wave incident on an m -layered structure sandwiched between semi-infinite input and output mediums, as depicted in Figure 2.17.

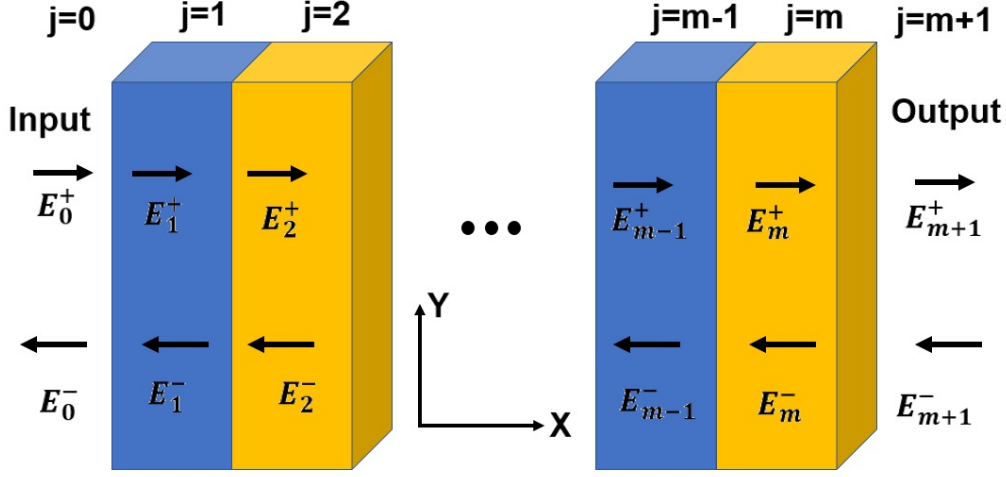


Figure 2.17: Anisotropic material having uniaxial isotropy and varying dielectric constants in the xy -plane and z -plane.

Each layer j ($j = 1, 2, \dots, m$) has a thickness d_j and its optical characteristics are defined by its complex index of refraction $\tilde{n}_j = n_j + ik_j$, which is a function of incident light wavelength. At any indicate in the system, the optical electric field is a sum of two components, one propagating in the positive x direction and the other, in the negative x direction, which at a position x in layer j are indicated by $E_j^+(x)$ and $E_j^-(x)$, respectively. An interface matrix describes the refraction at the interface of an electromagnetic (EM) wave as it propagates from layer j to layer k :

$$I_{jk} = \frac{1}{t_{jk}} \begin{pmatrix} 1 & r_{jk} \\ r_{jk} & 1 \end{pmatrix} \quad (2.4)$$

where r_{jk} and t_{jk} are the complex Fresnel reflection and transmission coefficients at the interface jk [133]. The Fresnel coefficients for light with an electric field vector in the plane of incidence (TM or p-polarized) are as follows:

$$r_{jk} = \frac{\tilde{n}_k^2 q_j - \tilde{n}_j^2 q_k}{\tilde{n}_k^2 q_j + \tilde{n}_j^2 q_k} \quad (2.5)$$

$$t_{jk} = \frac{2\tilde{n}_j \tilde{n}_k q_j}{\tilde{n}_k^2 q_j + \tilde{n}_j^2 q_k} \quad (2.6)$$

The Fresnel coefficients for TE polarized or s-polarized light (light with an electric field vector perpendicular to the plane of incidence) are given by:

$$r_{jk} = \frac{q_j - q_k}{q_j + q_k} \quad (2.7)$$

$$t_{jk} = \frac{2q_j}{q_j + q_k} \quad (2.8)$$

where $q_j = \tilde{n}_j \cos \varphi_j$, φ_j denote the refraction angle in layer j . Apart from refraction at an interface, the EM wave gains a phase as it propagates through the layer j , which is represented by the phase matrix:

$$L_j = \begin{pmatrix} \exp(-i\xi_j d_j) & 0 \\ 0 & \exp(i\xi_j d_j) \end{pmatrix} \quad (2.9)$$

where $\xi_j = \frac{2\pi}{\lambda} q_j$. Determine a transfer matrix S , which links the electric field at the input medium to the field at the output medium, by the equation:

$$\begin{pmatrix} E_0^+ \\ E_0^- \end{pmatrix} = S \begin{pmatrix} E_{m+1}^+ \\ E_{m+1}^- \end{pmatrix} \quad (2.10)$$

Utilizing the interface and the phase matrices provided by Equations 2.4 and 2.10, an equation for S can be expressed as follows:

$$S = \begin{pmatrix} S_{11} & S_{12} \\ S_{21} & S_{22} \end{pmatrix} = \left(\prod_{\nu=1}^m I_{(\nu-1)\nu} L_{\nu} \right) \cdot I_{m(m+1)} \quad (2.11)$$

There is no wave propagating inside the output medium in the negative x direction, When an electric field is incident from the input medium in the positive x direction; so, $E_{m+1}^- = 0$. For the overall system transfer matrix of Equation 2.12, the complex reflection and transmission coefficients of the complete system can be written as:

$$r = \frac{E_0^-}{E_0^+} = \frac{S_{21}}{S_{11}} \quad (2.12)$$

$$t = \frac{E_{m+1}^+}{E_0^+} = \frac{1}{S_{11}} \quad (2.13)$$

Write the total multilayer transfer matrix as follows to get the electric field in layer j :

$$S = S_j^- L_j S_j^+ \quad (2.14)$$

with

$$S_j^- = \left(\prod_{\nu=1}^{j-1} I_{(\nu-1)\nu} L_{\nu} \right) \cdot I_{(j-1)j} \quad (2.15)$$

and

$$S_j^+ = \left(\prod_{\nu=j+1}^m I_{(\nu-1)\nu} L_{\nu} \right) \cdot I_{m(m+1)} \quad (2.16)$$

The normalized incident wave is linked to the electric field propagating in the positive direction in layer j by:

$$\frac{E_j^+}{E_0^+} = t_j^+ = \frac{\frac{1}{S_{j11}^-}}{1 + \frac{S_{j12}^- S_{j21}^+}{S_{j11}^- S_{j11}^+} \exp(2i\xi_j d_j)} \quad (2.17)$$

In terms of the incident electric field, the total electric field at any arbitrary position inside layer j can be written as follows:

$$E_j(x) = E_j^+(x) + E_j^-(x) = [t_j^+ \exp(i\xi_j x) + t_j^- \exp(-i\xi_j x)] E_0^+ \quad (2.18)$$

Finite Element Method (FEM):

Scientific developments and contemporary computer technical capabilities pushed researchers to undertake high resources' consuming computations to solve Maxwell equations in photonics, for example, as also in many other disciplines. To correctly comprehend the investigated problems, mathematical models that imitate system behavior are required. These models are based on differential and integral equation systems, and FEM is one of the most used methods for solving them. Although this approach necessitates extensive computer use, it can be used to numerically answer a wide range of problems in Electromagnetism and Mechanics, for example. It can be used to solve tasks in one, two, or three dimensions, even if the geometry is complicated or the material under consideration is heterogeneous. In a few circumstances, the issues can be solved analytically, but the majority of them require a numerical solution. The FEM transforms differential or integral equations into numerical model equations that are easier to solve by utilizing a simple approximation of unknown variables, often based on several types of discretizations. For a detailed description see [134–136]. The first step in this approximation is to replace the continuous system with its discrete equivalent. To do this, we divide the domain into smaller subdo-

mains known as finite elements. The elements are linked by nodes, which are where we solve the numerical model equations. By employing a finer mesh, the electric fields can be estimated with more precision/resolution (more calculating points).

Commercial software based on FEM (COMSOL Multiphysics):

To model and simulate the photonic structures in this thesis, a commercial software named COMSOL Multiphysics was used [137]. The version used in this case is v.5.2.0. It enables us to run simulations using either its graphical user interface or the MATLAB program. The first method can be more intuitive since you can graphically model the structure and the computer displays lists of parameters, materials, geometric properties, and study resolutions at all times. Another benefit of the program is that the user can structure, assign different characteristics to any geometric domain at any time. We can choose a different material for each region, as well as the appropriate boundary conditions and, if necessary, a restriction.

The module "Electromagnetic waves, frequency domain" is required for the simulations. We define the parameters to utilize in the model and create the geometry after selecting the study for each case. We have to mesh our model after we have determined the geometry and materials (see Figure 2.18). To compute the electromagnetic fields at each discrete point, this mesh subdivision divides each domain into small, finite parts.

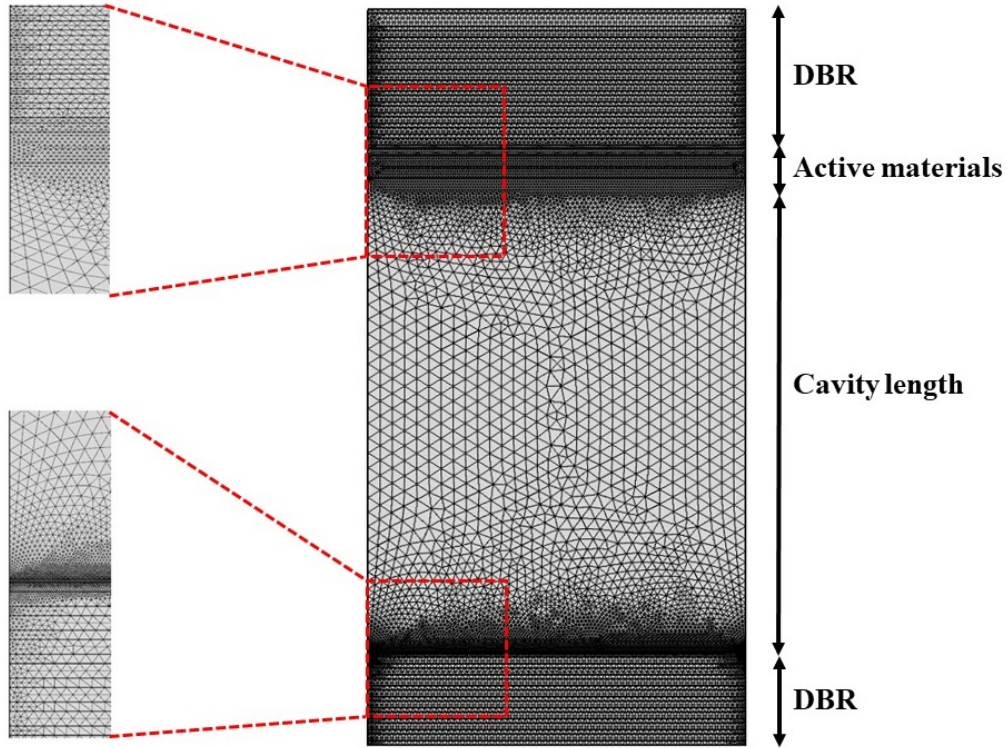


Figure 2.18: Each domain is subdivided into multiple subdomains. An example of a COMSOL image displaying a meshed model of a Fabry Perot Microcavity based on planar DBRs in an environment medium built for doing certain electric field distribution investigations.

As previously mentioned, we must adjust the mesh by increasing the density points in areas where the electromagnetic field is expected to vary more (at interfaces between two materials with quite different refractive index) and leaving it larger (but never larger than half a wavelength) in areas where we believe the field variation is smoother. We can get sufficient accuracy while saving calculating resources, i.e., the work will take less time, but we will have results with sufficient precision.

Chapter 3

Optical stability of CsPbX₃ (Br, I) perovskite nanocrystal for single photon emission

Metal-halide semiconductors with a perovskite crystal structure are interesting due to their ease of solution processing and have recently been successfully used in high-efficiency photovoltaics and bright light sources [138, 139]. Park and colleagues demonstrated the first perovskite-based single photon emission using all-inorganic CsPbI₃ QDs in 2015, revealing high single photon purity emission at room temperature caused by fast nonradiative Auger recombination [140], and also S.C. Boehme et al. revealed single photon purity emission at room temperature. [141] However, photobleaching and blinking limit its optical stability. In this chapter, cryogenic micro-PL and micro-TRPL spectroscopies are used to examine single CsPbX₃ (X = Br, I) PNCs with two different capping ligands. We deduced the average homogeneous linewidth of excitonic optical transitions for both cases. In comparison to the typical OLA/OA ligands, a significant reduction of the

blinking effect is observed in the case of ZW ligands, and strong linewidth narrowing and higher stability are observed. Furthermore, a slightly longer decay time (in a factor ~ 1.35) was measured for CsPbBr₃ single PNCs with ZW ligands, making them better suited for single photon sources. However, in the case of CsPbI₃ PNCs, the same strategy of using ZW ligands does not work, and the most used OLA/OA ligands are still the best candidate. In fact, we have measured $g^2(0) \sim 0.3$ for these CsPbI₃ PNCs. Furthermore, the spectral diffusion effect is significantly reduced in both single CsPbBr₃ (ZW ligands) and CsPbI₃ PNCs (OLA/OA ligands), resulting in micro-PL linewidths of $\sim 125 \mu\text{eV}$ and $\sim 140 \mu\text{eV}$, respectively.

3.1 Introduction and state of the art

Colloidal semiconductor QDs can be used as single photon emitters [78], which could be important in applications related to quantum technologies (quantum cryptography, quantum sensing and quantum communication) [52, 142]. The majority of these investigations with photons have so far focused on epitaxial self assembled QDs, colloidal CdSe-based QDs, Color centers in Diamond, and single molecules. The common challenges of such applications, such as emission intermittency (blinking), photostability, and spectral diffusion, stem from factors inherent to the QD material (surface traps, enhanced Auger processes, facile photo-ionization, photo-oxidation and other environmental effects) [78]. Specially designed colloidal core-shell heterostructures have been shown to reduce blinking while giving up enhanced multiphoton emission [78].

LHPs exhibit outstanding optoelectronic properties including high absorption coefficient, high carrier mobility, long carrier lifetime, and high defect tolerance [40, 41, 143]. With these semiconductors, low-cost solar

cells with conversion efficiencies of around 20% have been demonstrated [144–146]. Fully inorganic CsPbX₃ (X = Cl, Br, I) PNCs have been synthesized with precise size and compositional control, offering very bright, tunable, narrow-band luminescence over the whole visible wavelength range [55]. Due to the high defect tolerance and lack of detrimental mid-gap surface defects, room-temperature photoluminescence quantum yields of up to 90% can be achieved without any additional surface passivation. This fact opened up a plethora of possibilities for tunable quantum light sources based on compositional and quantum size tuning. These materials have excellent emission properties [42], however, the quality of the optical emission was limited by photobleaching and blinking.

Although colloidal lead halide PNCs have emerged as the basis for versatile photon sources, their processing and optoelectronic applications are hampered by the loss of colloidal stability and structural integrity due to the facile desorption of surface capping molecules during isolation and purification. So, it would be enticing to use the high oscillator strength, high quantum yield, efficient charge transport, solution-processability, and ease of synthesis of PNCs with higher stability (no photobleaching and no blinking) for applications related to the quantum technologies.

In this chapter, to address this issue, we have examined different passivation methods such as encapsulating the single PNCs with Poly(methyl methacrylate) (PMMA), capping PNCs with hBN flakes, and passivating the PNCs by (di-dodecyl dimethylammonium bromide) DDAB ligands, which were not efficient. Alternatively, we undertake another ligand capping strategy, consisting in the use of inexpensive long-chain ZW molecules, *N* – Dodecyl – *N,N* – dimethyl – 3 – ammonio – 1 – propanesulfonate, which are readily available commercially. This type of ligands, in particu-

lar, enables the isolation of clean PNCs with PL QY of more than 90% [56]. Bidentate ZW ligands, which have two functional groups that can bind to NCs, are particularly attractive due to their ability to improve the stability of NCs and enhance ligand–surface interactions [56–58]. The bidentate ZW ligands show great promise for efficient surface passivation and PL enhancement [59]. Krieg et al. [56] suggested using long-chain zwitterionic molecules as capping ligands for CsPbX₃ PNCs, and these ligands demonstrated a significant improvement in durability and stability [56]. With this ligand passivation, the spectral diffusion of the CsPbBr₃ is drastically reduced, and their stability is greatly increased. Their average homogeneous linewidths decreased by an order of magnitude when compared to OLA/OA ligands, and their lifetime increased slightly (factor ~ 1.35), making them ideal for use as a single photon emitter source. However, this strategy did not work for CsPbI₃ PNCs and the typical OLA/OA ligands are still the best option.

3.2 Experimental Details and Methods

Synthesis of Colloidal Solution (OLA/OA ligands):

CsPbX₃ (X=Br, I) PNCs were produced using the hot-injection technique described by Kovalenko and co-workers [55]. Without going through any additional purification process, all the reactants were used as received. In a brief, Cs-oleate solution was prepared by mixing 0.41g of Cs₂CO₃ (Sigma-Aldrich, 99.9%), 1.25 mL of oleic acid (OA, Sigma-Aldrich, 90%), and 20 mL of 1-octadecene (1-ODE, Sigma-Aldrich, 90%) were loaded together into a 50 mL three-neck flask at 120°C under vacuum for 1h under constant stirring. Then, the mixture was N₂-purged and heated at 150°C to reach the complete dissolution of Cs₂CO₃. The solution was stored under N₂, keeping

the temperature at 100°C to prevent Cs-oleate oxidation. For the synthesis of CsPbBr_3 and CsPbBrI_2 PNCs, 1.0 g of PbBr_2 (ABCR, 99.999%), and the corresponding $\text{PbBr}_2/\text{PbI}_2$ mixture, were mixed with 50 mL of 1-ODE into a 100 mL three-neck flask. The mixture was simultaneously degassed and heated at 120°C for 1h under constant stirring. Then, a mixture of 5 mL each of both pretreated (130°C) OA and oleylamine (OLA, Sigma-Aldrich, 98%) were separately added to the flask under N_2 , and the mixture was quickly heated at 170°C . At the same time, 4 mL of Cs-oleate solution was injected to the mixture, followed by 5 seconds in an ice bath to quench the reaction. The colloidal solutions were centrifuged at 4700 rpm for 10 minutes in order to perform the isolation process of PNCs. After discarding the supernatant, PNC pellets were separated and redispersed in toluene to concentrate them at 100 mg/mL.

Synthesis of Colloidal Solution (ZW ligands):

The synthesis of CsPbBr_3 PNCs by adding ZW ligands was performed by mixing stoichiometric amounts of Cs-oleate, Pb-oleate, TOP- Br_2 and sulfo-betaine based on N-Dodecyl-N,N-dimethyl-3-ammonio-1-propanesulfonate (ASC12), with some modifications. [147] To prepare Cs-oleate solution (0.4 M), 1.628 g Cs_2CO_3 (5 mmol), 5 mL oleic acid 16 mmol and 20 mL 1-octadecene (1-ODE) were combined into a three-neck flask under vacuum upon heating to 120°C , until the completion of gas evolution. On the other hand, Pb-oleate (0.5 M) was prepared by mixing 4.61 g Lead (II) acetate trihydrate (12 mmol), 7.6 mL OA (24 mmol) and 16.4 mL ODE in a three-necked flask under vacuum upon heating to 120°C , until complete evaporation of acetic acid and water. Simultaneously, TOP- Br_2 solution (0.5 M) was prepared by combining 6 mL trioctylphosphine (TOP, 13 mmol) 9.4 mL of each toluene and mesitylene, and 0.6 mL bromine (11.5 mmol) under

a N₂ purge.

At this stage, 5 mL of as-prepared Pb-oleate (0.0025 mol), 4 mL Cs-oleate (0.0016 mol), 0.336 g ASC12 (1 mmol) and 10 mL 1-ODE were mixed in a 50-mL three-necked-flask and heated to 120 °C under vacuum. Then, mixture reaction was N₂-purged, and the temperature was increased to reach 180 °C. Here, 5 mL TOP-Br₂ (0.0025 mol) was quickly injected, and the reaction was quenched in an ice bath. To isolate the final product, PNCs were centrifuged at 5000 for 5 min with 60 mL acetone. PNCs pellets were separated from supernatant, redispersed with toluene at 50 mgmL⁻¹.

Material characterization: The CsPbBr₃ PNCs synthesized using zwitterionic (ZW) ligands show improved stability when compared to traditional PNCs with OLA/OA surface ligands. As demonstrated in the TEM image in Figure 3.1.a,c, the dominant shape of CsPbBr₃ PNCs with OLA/OA and ZW ligands is cubic, and the average size of these nanocubes is around 10.8 nm and 11.6 nm, respectively, as determined from their size histograms (obtained from TEM images) in Figure 3.1.b,d. According to Figure 3.1.e,f, the TEM image of CsPbI₃ PNCs synthesized with OLA/OA ligands are also cubic, and its size histogram shows a Gaussian distribution peaked near 13.1 nm, which is slightly larger than CsPbBr₃ PNCs [117, 148]. The green and red colors in this chapter correlate to the CsPbBr₃ and CsPbI₃ PNCs, respectively, and correspond to their emission wavelengths.

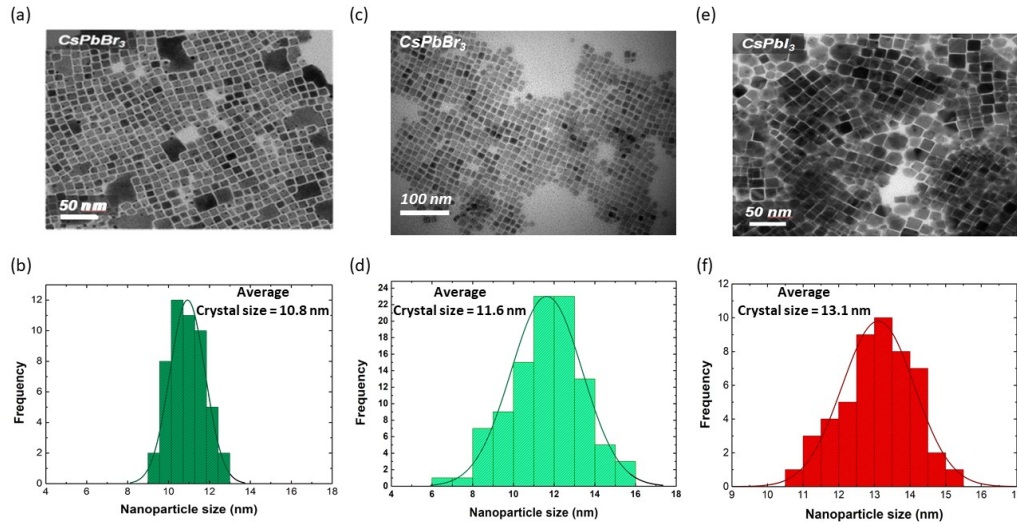


Figure 3.1: Transmission Electron Microscopy (TEM) measured by a JEOL 100 kV microscope, model HT7800 Serie, of colloidal suspensions of CsPbBr₃ PNCs (dropped on a copper grid) with OLA/OA ligands (a), CsPbBr₃ PNCs with ZW ligands (c), and CsPbI₃ PNCs with OLA/OA ligands (e). (b, d, f) Size distribution histograms of these PNCs as obtained from the TEM images.

Preparation of isolated CsPbBr₃ (X=Br, I) NCs dispersed on SiO₂ substrates:

The goal of this study is to measure the emission of light from single PNCs. To do this, we prepared samples with PNCs that were spatially isolated from each other. To prepare the samples, a commercial Si wafer coated with a 285 nm thick SiO₂ film was used, the wafer is cleaned sequentially by ethanol, isopropanol, and acetone. Then, the deposition of PNCs was carried out by dip coating (as explained in Figure 2.2) using a colloidal suspension of PNCs with a controlled concentration (in the case of 0.1 – 1 mg/ml) in Toluene, in order to define an interparticle distance greater than the optical resolution.

3.3 Results and Discussion

Figure 3.2.a indicates how μ -PL spectra of single PNCs of CsPbBr₃ with OLA/OA ligands at 4K are characterized by narrow lines (in green), whose peak energies cover the emission energy range of the inhomogeneously broadened PL spectrum (black line) measured in a high-density sample made with the same PNCs. Lorentzian functions were used to fit these μ -PL spectra whose FWHMs are represented as a histogram in Figure 3.2.b. The mean value of the FWHM for CsPbBr₃ PNCs with OLA/OA ligands is 2.35 meV. As observed in Figures 3.2a,b (see also below), such large FWHMs of μ -PL spectra can be due to spectral diffusion. Exciton phonon interaction should be highly reduced at 4 K and eventually it would depend on the QD/PNC size [117]; however, in our case, we do not find any correlation nor dependence on size for the FWHM, indicating that the linewidth should be limited by spectral diffusion, hence very strong in PNCs with OLA/OA ligands. We have addressed this problem, and examined different methods, such as encapsulating (covering) the single PNCs with Poly(methyl methacrylate) (PMMA), or hBN flakes, and passivating with (di-dodecyl dimethylammonium bromide) DDAB ligands. Figures 3.2.c, shows the μ -PL spectra of a single CsPbBr₃ PNC from a sample encapsulated by spin coating 20 nm of PMMA. The FWHM for this μ -PL spectrum is 2.36 meV, hence still limited by spectral diffusion, other than observing blinking effect. Figures 3.2.d, displays the μ -PL spectra of two single PNCs of sample prepared from a colloidal solution of CsPbBr₃ nanocrystals synthesized with OLA/OA ligands after the passivation with DDAB. It is clear that DDAB passivation is not working, because the linewidths of μ -PL spectra of these two PNCs are 1.47 and 1.36 meV. On the other hand, Utzat et al. [149] indicated that ZW ligands can exhibit higher stability than typical PNCs

with OLA/OA surface ligands. In fact, the μ -PL spectra measured here in single CsPbBr₃ PNCs synthesized now with ZW ligands exhibit very narrow lines (in green), in the order of $\sim 125 \mu\text{eV}$, as shown in Figures 3.2.e. Again, their peak energies perfectly cover the energy range of the inhomogeneously broadened PL spectrum (black line) measured in a high-density sample prepared with the same PNCs. As can be observed by comparing of these μ -PL spectra (Figure 3.2.a) with those for CsPbBr₃ PNCs synthesized with OLA/OA ligands (Figure 3.2.e), the linewidths in ZW-PNCs are less than 10% of those in OLA/OA-PNCs. Indeed, the histogram of FWHMs in ZW-PNCs, is much less disperse and represented by a Gaussian distributions (black line) with a mean value of $250 \mu\text{eV}$ (see the zoom included in Figure 3.2.f), i.e., one order of magnitude lower than the mean value for OLA/OA PNCs. It is worth to highlight that we have measured a value as low as $125 \mu\text{eV}$, which, up to our knowledge, is the narrowest of all currently available values in literature, as summarized in table 3.1, where it is listed the FWHMs obtained by different authors on PNCs with different types of ligands. The results of the present study are shown in the last row of the table (in blue). Our system resolution's linewidth is $\sim 120 \mu\text{eV}$. As a result, we can conclude that the best technique for reducing linewidth broadening (and blinking, as shown below) by spectral diffusion consists in the use of CsPbBr₃ PNCs synthesized with ZW ligands.

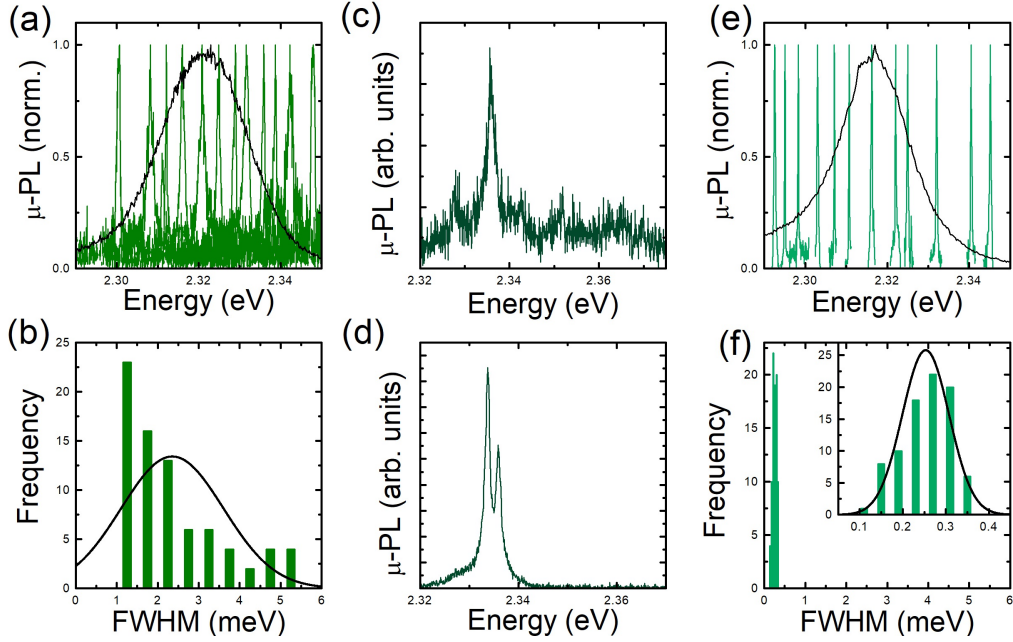


Figure 3.2: (a) The representative μ -PL spectra of single CsPbBr₃ PNCs synthesized with OLA/OA (dark green lines) in comparison to the PL spectra of the corresponding high-density samples made with the same PNCs (black line). (b) Histogram of FWHM values obtained from fittings to the Lorentzian shapes of the μ -PL spectra in (a). (c) μ -PL spectra of a single CsPbBr₃ PNCs in a sample covered with PMMA layer 20 nm thick. (d) μ -PL spectra of two single CsPbBr₃ PNCs in a sample prepared from the original colloidal solution (CsPbBr₃ PNCs synthesized with OLA/OA) after DDAB passivation. (e) Representative μ -PL spectra of single CsPbBr₃ PNCs with ZW (light green lines) as compared to the PL spectrum of the corresponding high-density sample made with the same PNCs (black line). (f) Histogram of FWHM values obtained from fittings to the Lorentzian shapes of the μ -PL spectra in (e).

Figure 3.3.a shows how μ -PL spectra at 4 K of single PNCs of CsPbI₃ synthesized with OLA/OA consist of very narrow lines in the order of ~ 140 μ eV, whose peak energies cover the energy range of the PL spectrum measured in a high-density sample made with the same PNCs. The histogram of FWHMs, as depicted in Figure 3.2.b, is well represented by a Gaussian distributions (black line) from which a FWHM mean value is 250 μ eV, with a lowest value of 140 μ eV. In spite of these nice results, we still observe a poor stability of the PNCs and blinking under laser excitation. In order to try to solve these problems, we examined different passivation/encapsulation

methods. Figures 3.3.c shows the μ -PL spectra of several single CsPbI₃ PNCs from a sample covered with a spin coated PMMA layer 20 nm thick. The linewidths of one of the μ -PL lines is 5.63 meV, hence limited by spectral diffusion and blinking effects, as indicated above for CsPbBr₃ PNCs. We also tested a local encapsulation by hBN nanoflakes transferred onto the PNCs by using polydimethylsiloxane (PDMS), as carried out for 2D perovskites [62, 150]. Unfortunately, hBN nanoflakes suppress the emission of single PNCs, making it difficult to obtain PL signal from samples prepared using diluted colloidal solution, and we prepared new ones with increased concentration, which in turn results in PNC agglomerations on the sample. Figure 3.3.d shows a μ -PL spectrum of a single CsPbI₃ PNC passivated with a hBN flake that exhibits a linewidth of 0.2 meV over a tail of background emission due to agglomeration of PNCs, along with spectral diffusion and blinking. Finally, Figure 3.3.e,f shows μ -PL spectra of single CsPbI₃ PNCs synthesized with ZW molecules, from which we deduce a mean value of FWHM of ~ 1.1 meV, other than blinking effect. Therefore, ZW ligands does not work in the case of CsPbI₃ PNCs, and the conventional OLA/OA ligands are still the best option for CsPbI₃ PNCs (see Figure 3.3.a).

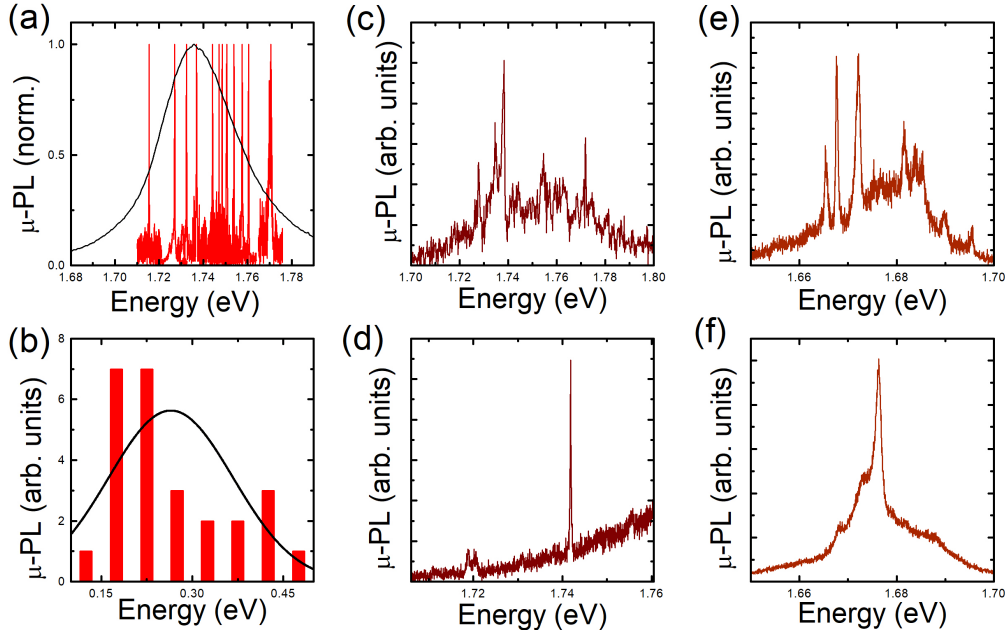


Figure 3.3: (a) The representative μ -PL spectra at 4 K of CsPbI_3 PNCs synthesized with OLA/OA as compared to the PL spectrum (black line) high-density samples made with the same PNCs. (b) Histogram produced using FWHM values obtained from fittings to the Lorentzian shapes of the μ -PL spectra measured. (c) μ -PL of single CsPbI_3 PNCs in a samples covered with a PMMA film 20 nm thick. (d) μ -PL spectrum of a single CsPbI_3 PNCs capped with a hBN. (e, f) μ -PL spectra of single CsPbI_3 PNCs synthesized with ZW.

Figure 3.4.a,b&c shows the statistical distribution of the extracted FWHM of single PNCs of CsPbBr_3 with OLA/OA ligands, CsPbBr_3 with ZW ligands and CsPbI_3 with OLA/OA ligands, respectively, as a function of their emission energy extracted from the μ -PL spectra shown above (Figure 3.2&3.3). Figure 3.4.a reveals that the variation in CsPbBr_3 PNCs with OLA/OA ligands is between 1-6 meV and the values are highly dispersed. In contrast, CsPbBr_3 PNCs with ZW ligands are concentrated around the average value, 0.25 meV, with values between 0.1 and 0.4 meV, but any energy dependency is observed (Figure 3.4.b). We also find a similar fluctuation in CsPbI_3 0.1-0.5 meV (see Figure 3.4.c), but now possibly we observe a certain tendency to increase with confinement, possibly due to a stronger

exciton-phonon interaction by increasing the emission energy (decreasing PNC size) [151].

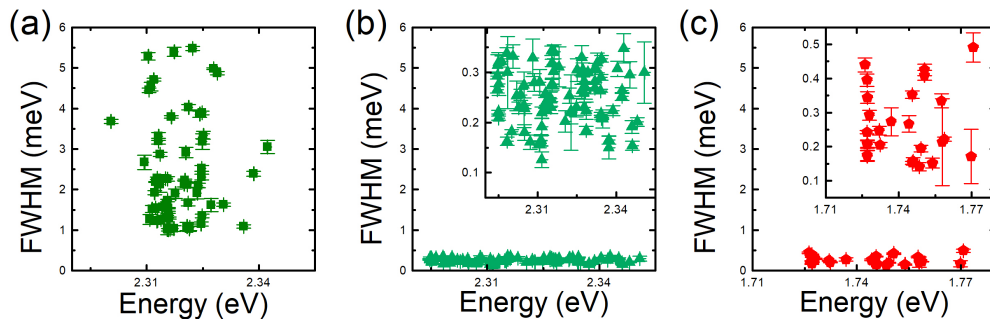


Figure 3.4: Statistics of the FWHMs that were obtained for the μ -PL spectra measured in CsPbBr₃ PNCs synthesized with OLA/OA (a) and ZW (b), and CsPbI₃ PNCs synthesized with OLA/OA (c).

MATERIAL	ligand types	Morphology	Ave. size	FWHM	decay time	TEMP.	Ref.
CsPbBr ₃	ZW	Single Crystal	13.5 (nm)		210 ps	3.6(K)	[149]
CsPbBr ₃	DDAB	Single Crystal	5 (nm)	2 (meV)	0.4 ns	4.6(K)	[141]
CsPbBr ₃	OLA/OA	Single nanoplatelet	23.5 ± 3.2 (nm)	0.94(meV)	79±8 ps	5(K)	[152]
MAPbI ₃		Single Microplate	~1.1 (μm)	~200(μeV)	~0.7 ns	4(K)	[153]
CsPbBr ₃		Single Microcrystals	-compact ~322.1(nm) -porous ~313.0(nm) -islanded ~133.9(nm)	-compact ~540.6(nm) -porous ~543.4(nm) -islanded ~535.6(nm)		4(K)	[154]
CsPb(Cl/Br) ₃	OLA/OA	Single nanocrystals	~9.5 (nm)	~1(meV)	180-250 ps	6(K)	[138]
CsPbI ₃	OLA/OA	Single nanocrystals	~9.3 (nm)	~200(μeV)	~1.02 ns	~4(K)	[139]
CsPbI ₃	OLA/OA	Single nanocrystals	~9.3 (nm)	~200(μeV)	~0.93 and ~1.02 ns	~4(K)	[155]
FAPbI ₃	OLA/OA	Single nanocrystals	10-15 (nm)	1.2(meV)	1.5 ns	~3.6(K)	[156]
CsPbBr ₃	OLA/OA	Single nanocrystals	~9.4(nm)	>1(meV)	~355 ps	~4(K)	[157]
CsPbBr ₃	OLA/OA	Single nanocrystals	8–10(nm)	~170(μeV)	~180 ps	2(K)	[158]
CsPbBr ₃	OLA/OA	Single nanocrystals	~8.8(nm)	~5(meV)		10(K)	[159]
CsPbI ₃	OLA/OA	Single nanocrystals	~9.3(nm)		0.85 ns	3(K)	[160]
CsPbBr ₃ CsPbI ₃	ZW OLA/OA	Single nanocrystals	~11.6(nm) ~13.1(nm)	0.125(meV) 0.140(meV)	0.3 ns ~1 ns	4(K)	

Table 3.1: Most representative results found in literature for CsPbX₃, MAPbX₃, and FAPbX₃, perovskites regarding the PL linewidth evolution. We include the type of ligands, average size, FWHM of the PL, lifetime (τ), Temperature, and references. The results of this study are shown in the last row of the table (in blue).

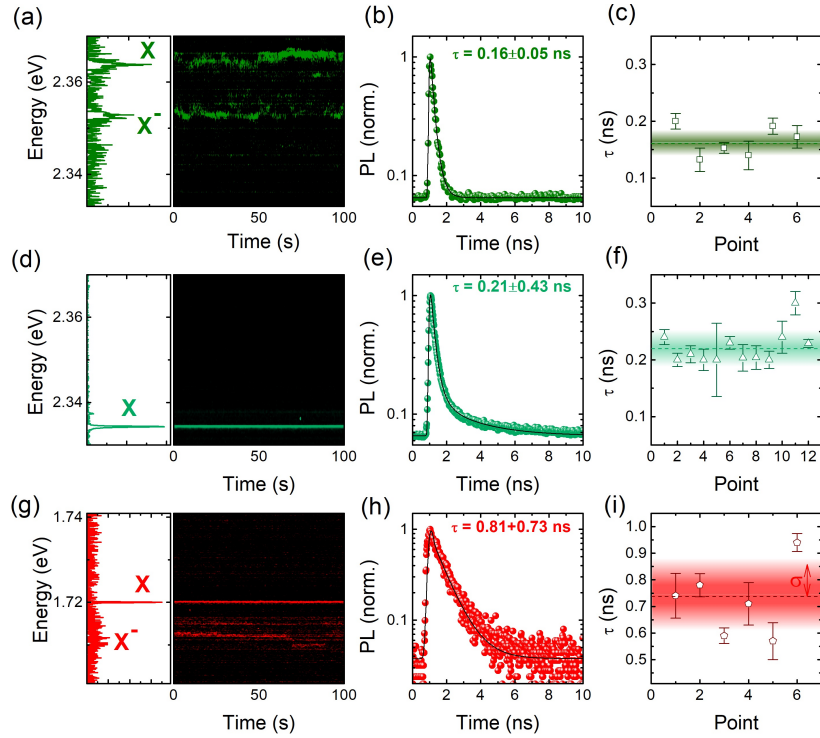


Figure 3.5: μ -PL spectrum (left panel) and time-dependent spectral evolution (right panel) of optical emission of a single CsPbX₃ (Br₃, I₃) NC (a, d, g). Each PL data point has a 1s integration time. CsPbBr₃ PNCs (dark green Line) with OLA/OA ligands (a) and CsPbBr₃ PNCs (light green Line) with ZW ligands, with significantly decreased spectral diffusion and blinking effects, were detected for this single PNC (d) and CsPbI₃ PNCs (red Line) PNCs with OLA/OA ligands (g) demonstrating long-term stability. Example of Time-resolved PL (TRPL) on a 10 ns time scale from the emission of single (b) CsPbBr₃ PNCs with OLA/OA ligands, (e) CsPbBr₃ PNCs with ZW ligands, (h) CsPbI₃ PNCs with OLA/OA ligands. Statistics of decay (τ) of (c) CsPbBr₃ PNCs with OLA/OA ligands, (f) CsPbBr₃ PNCs with ZW ligands, (i) CsPbI₃ PNCs with OLA/OA ligands.

Representative spectral and intensity-time series of single CsPbBr₃ PNCs with OLA/OA and ZW ligands and CsPbI₃ PNCs with OLA/OA ligands, are shown in Figures 3.5.a,d&g, respectively. As demonstrated in the left panel of Figure 3.5.a, for CsPbBr₃ PNCs with OLA/OA ligands, two μ PL lines are observed (time integrated) at central peak energies of 2.364 eV, attributed to recombination of neutral excitons (X), and 2.353 eV, attributed to recombination of the trion (here depicted for the case of a negatively

charged exciton) (X^-), i.e., with the latest with binding energy of 11 meV. This is only a tentative identification based on a review of ref. [161]. The time-dependent evolution of these PL peak are depicted in the image at the right panel of Figure 3.5.a. As evidenced in here, the observed spectral diffusion is clearly contributing to the linewidth broadening, giving an overall linewidth (time integrated) of 0.84 meV for X transition. As probed above for different passivation methods, the best results were synthesis of CsPbBr₃ PNCs was carried out with ZW molecules [56, 149]. As expected, the μ -PL spectra of these single PNCs are not suffering of spectral diffusion (no variation of the μ -PL peak with time), and hence we observe a very narrow μ -PL spectrum of neutral exciton (0.25 meV, time integrated) whose peak energy is observed at 2.334 eV of with time, as observed in left and right panels of Figure 3.5.d. Similarly happens for CsPbI₃ PNCs with OLA/OA ligands, where the μ -PL line associated to recombination of neutral excitons is observed 1.720 eV (X) with a very low linewidth of 0.16 meV (see left panel of Figure 3.5.g), which is due to the weak spectral diffusion (see right panel of Figure 3.5.g). However, a clear emission contribution at 1.711 eV is observed at certain times (see both panels of Figure 3.5.d), which is attributed to the blinking effect to the negatively charged exciton (X^-) state. The (X^-) state exhibits a binding energy of 11 meV, very similar to the value found above for the case of CsPbBr₃ PNCs of similar size, which is also consistent with reported values in literature [139, 155, 161, 162]. It is important to note that no blinking was observed in the case of CsPbBr₃ PNCs with ZW ligands. Figure 3.5.b, illustrates a typical μ -TRPL spectrum for a single CsPbBr₃ PNC with OLA/OA ligands. These PNCs are characterized by exciton lifetimes τ in the order of 0.16 ± 0.05 ns. Figure 3.5.c shows a statistical sampling of the decay time measurement. The mean

value of τ is 0.16 ns with a dispersion of 0.02 ns. In Figure 3.5.e, the μ -PL decay curves obtained for the CsPbBr₃ PNCs with ZW ligands revealed an increased lifetime by a factor ~ 1.35 , (0.21 ± 0.43 ns) as deduced from its statistics in Figure 3.5.f, where the mean value of τ is 0.22 ns, and its dispersion of 0.03 ns. This mean value is consistent with lifetimes reported in the literature for CsPbBr₃ PNCs for OLA/OA, which are in the order of 200 ps [149,163]. Figure 3.5.h shows a typical μ -TRPL spectrum for a single CsPbI₃ PNC with OLA/OA ligands, which is characterized by a decay time τ 0.81 ± 0.073 ns. Figure 3.5.i shows a statistical sampling of the decay time measurements, from which a mean value of $\tau = 0.72$ ns and a dispersion of 0.13 ns are deduced. The results of the present study are shown in the last row of the table 3.1 (in blue).

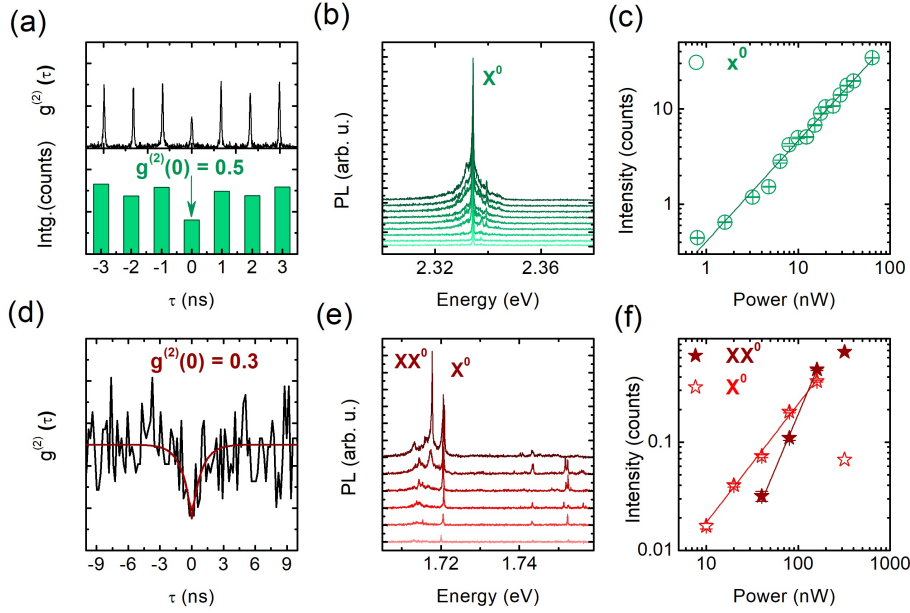


Figure 3.6: (a) (upper panel) photon correlation measurements of the optical emission of single PNCs obtained with Hanbury–Brown and Twiss (HBT) set-up at 4K with a $g^{(2)}(0)$ value of ~ 0.5 for CsPbBr₃ PNCs (ZW) ligands under pulsed excitation, (lower panel) integrated coincidences histogram extracted from the raw data. (b) The μ -PL spectra of a single CsPbBr₃ NC measured and only showed exciton recombination peaks as the pumping power increased from 0.8 to 64 nW. (c) Evolution of the integrated PL intensity with the laser power for exciton (X^0) which was observed experimentally in CsPbBr₃ NCs in a log-log plot showing linear dependence. (d) Measurement result of the second-order correlation function ($g^{(2)}(0) \sim 0.3$) for a single CsPbI₃ Perovskite NC under CW excitation, which is below the antibunching threshold at $g^{(2)}(0) = 0.5$. (e) μ -PL spectra series of a single CsPbI₃ NC as a function of excitation power. (f) Evolution of the integrated intensity as a function of power for exciton (X^0) and biexciton (XX^0) which were observed experimentally in CsPbI₃ NCs in a log-log plot.

Figure 3.6.a shows the photon correlation for the μ -PL peak of a single CsPbBr₃ PNCs with ZW ligands, under pulsed low power excitation (0.8 nW) measured with our Hanbury-Brown-Twiss (HBT) intensity interferometer setup (see Figure 2.12). It demonstrates that $g^{(2)}(0) \sim 0.5$, and hence the quantum nature of the optical emission. The photon correlation trace for the μ -PL peak of a single CsPbI₃ PNCs is shown in Figure 3.6.d, normalized to its long-time amplitude obtained with CW low power excitation (80 nW). This measurement shows that $g^{(2)}(\tau)$ is $\simeq 0.3$ at $\tau = 0$ and then

increases to unity at longer delay times. This is an evidence of single photon emission, $g^2(0) = 1-1/n$, where n is the mean number of photons. So, $g^2(0)=0.3$ gives $n = 1.42$ photons, as shown in Figure 3.6.d. Figure 3.6.b illustrates the μ -PL spectra of a single CsPbBr₃ PNC as a function of the excitation power from 0.8 nW to 64 nW, where a single emission line at 2.334 eV (marked as X^o in the plot). Moreover, a near linear dependence of its intensity is observed with power, as shown in Figure 3.6.c, where a slope $m= 1.06 \pm 0.02$ is deduced. This linear dependence of the μ -PL intensity on laser power confirms that optical emission should arise from the neutral exciton (X^o) recombination [153, 164, 165]. Figure 3.6.e illustrates the μ -PL spectra of a single CsPbI₃ PNC as a function of the excitation power, where a sharp line marked as X^o at 1.721 eV can be observed at the lowest laser power of 10 nW. When the power is increased to 320 nW, a second line (marked as XX^o) red shifted $\simeq 4$ meV with respect to the X^o one appears in the emission spectrum. Figure 3.6.f shows the integrated intensities of the observed lines as a function of laser power. We observe that the intensity of line X^o shows a power dependence with exponent 1.07 ± 0.05 , hence near a linear dependence. The onset of emission from XX^o arises at higher laser powers than that from X^o , and the intensity of the emission increases with a super-linear power dependence, with a fitted exponent of 1.94 ± 0.09 . This variation clearly demonstrates that XX^o is correctly associated to the biexciton recombination in CsPbI₃ PNCs, consistently with observations in literature [138, 139, 166]. It could be claimed that entangled photon pairs can be created via the cascade between XX^o and X^o . So, using this perovskite platform could be an alternative to develop room temperature entangled photon pairs. But, in order to do this, it will be required to analysis of the fine structure splitting (which can be high in perovskite

materials and reduces the chances of producing entangled photon pairs), as well as the problems with stability, durability.

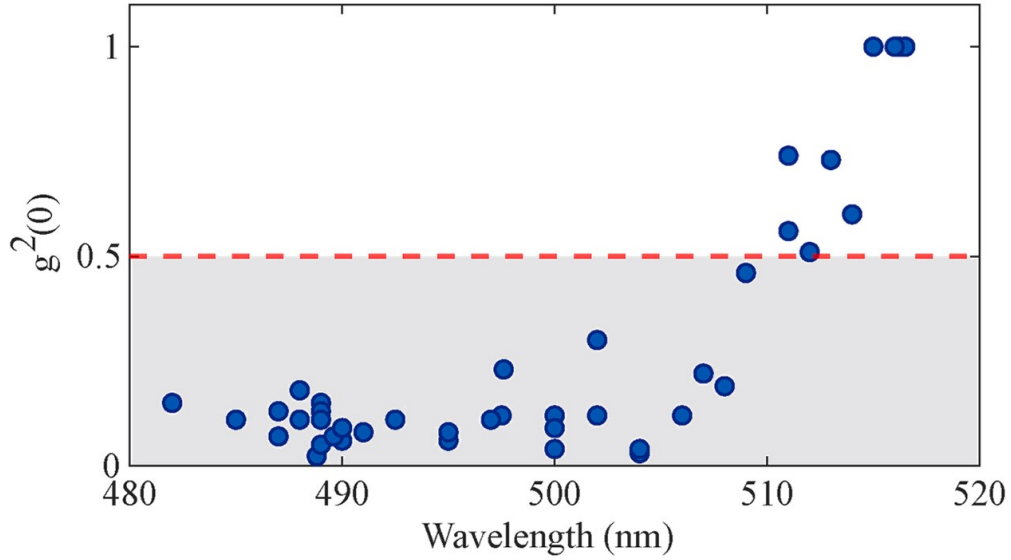


Figure 3.7: Quantum size effect on CsPbBr₃ NCs. Experimental $g^2(0)$ values (blue dots) as a function of the central wavelength of the emission for a set of 40 CsPbBr₃ NCs. The threshold for antibunching is reported (red dashed line). [167]

Figure 3.7 shows a statistically studied by the C.Soci et al. [167], which showing the size-dependent high quality single photon emission (blue dots) as a function of the central wavelength of the emission for a set of 40 CsPbBr₃ NCs. As you can see Figure 3.4.b the average value of peak energy in CsPbBr₃ PNCs with ZW ligands is 2.32 eV (534.5 nm), indicating that we are not in strong confinement, to compare with the Figure 3.7. CsPbBr₃ PNCs have a Bohr radius of ~ 7 nm [168], while the average size of CsPbBr₃ PNCs with ZW ligands is 11.6 nm, as we now when the size of the nanoparticles is larger than the Bohr radius, the quantum confinement is weak. Because of that, we can not achieve a $g^2(0)$ value lower than 0.5 [169]. The Bohr radius of CsPbI₃ PNCs is 12 nm [168], with an average size of 13.1 nm, which is closer to a strong confinement.

3.4 Conclusions

To summarize, in this chapter we used cryogenic μ -PL and μ -TRPL spectroscopy to examine single PNCs with two different capping ligands, and we deduced an average homogeneous linewidth of excitonic optical transitions in freshly prepared samples for both cases (OLA/OA and ZW ligands). In comparison to the typical OLA/OA ligands with ~ 2.35 meV linewidths on average, the homogeneous linewidths of single CsPbBr₃ PNCs with ZW ligands exhibit a significant narrowing with higher stability due to drastically decreased spectral diffusion and blinking effects. In this way, we have obtained a mean linewidth of ~ 250 μ eV with a lowest value of ~ 125 μ eV, which, up to our knowledge, is the actual lowest reported linewidth value (see table 3.1). In fact, this lowest value can be overestimated, as our spectral resolution (120 μ eV) can blur the real linewidth. Furthermore, based on μ -TRPL measurements, we have demonstrated an increase of the exciton lifetime by a factor ~ 1.35 for CsPbBr₃ PNCs with ZW ligands, making them better for quantum light sources. However, in the case of single CsPbI₃ PNCs, the strategy of ZW ligands did not work, and the traditional OLA/OA ligands are still the best candidate, even if exhibiting the blinking phenomenon between X^0 to X^- states. For CsPbI₃ NCs with the average size of ~ 250 μ eV and the lowest value of ~ 140 μ eV for μ -PL linewidth. Furthermore, we obtained $g^2(0) \sim 0.3$ for CsPbI₃ single PNCs. Also we obtain $g^2(0) \sim 0.5$ for CsPbBr₃ single PNCs with ZW ligands, but to achieve the ideal emission, we must optimize the size of the NCs. However, more statistics for $g^2(0)$ at 4 K and higher temperatures will be needed in the future for establishing the potentiality of CsPbBr₃ and CsPbI₃ PNCs for quantum technologies.

Chapter 4

Donor-acceptor discrete optical emission in 2D perovskites

Two-dimensional (2D) van der Waals nanomaterials have attracted considerable attention for potential use in photonic and optoelectronic applications on the nanoscale, due to their outstanding electrical and optical properties. Currently, 2D perovskite belonging to this group of nanomaterials is widely studied for a wide range of optoelectronic applications, due to strong quantum confinement and the sizable band gap in these materials [14–16]. Thanks to their excitonic properties, 2D perovskites are also promising materials for photonics and nonlinear devices working at room temperature. Nevertheless, strong excitonic effects can reduce the photocurrent characteristics when using the thinner perovskites phase. In this chapter it is investigated the presence of single donor-acceptor pair optical transitions in 2D Lead Halide Perovskites, by micro-photoluminescence and time-decay measurements, which are characterized by sub meV linewidths ($\simeq 120\mu eV$) and long decay times (5-8 ns). X-Ray Photoemission and DFT calculations have been employed to investigate the chemical origin of elec-

tronic states responsible of these donor-acceptor pairs. The association of Phenethylammonium with Methylammonium cations, the latter molecule being only present in 2D Halide Perovskites with thicker phases $n \geq 2$, has been identified as a likely source of the donor-acceptor pair formation, corresponding to the displacement of lead atoms and their replacement by methylammonium. The study of discrete donor-acceptor pair (DAP) sharp and bright optical transitions in 2D Lead Halide Perovskites opens new routes to implement DAP as the carrier sources for novel designs of optoelectronic devices with 2D perovskite, as for example enhanced interactions in van der Waals interlayer heterostructures dipolar interactions between localized interlayer excitons in van der Waals heterostructures [170], or to develop new route for single photon emission [171].

4.1 Introduction

Since the discovery of the high light-energy conversion efficiency published in 2009 [24], the use of perovskite materials has been demonstrated in a large number of photonics devices owing to their interesting properties related to charge transport, excitons and photoexcited carriers generation, bandgap tunability and exciton binding energy in halide perovskites (HPs), and ferroelectric properties and magnetic field effects in oxide perovskites [172]. This rapid growth in academic activity has merged with another intense field of research, the study of 2D monolayer semiconductors. The isolation of mechanically exfoliated graphene in 2004 has boosted the engineering of an interesting new set of high-quality 2D semiconductor samples that can be prepared at a low cost and without specialised equipment. This is the case for 2D Lead Halide Perovskites (LHPs) [29, 30], which have recently been analysed more closely because of their potential

integration in high-efficiency photovoltaics and photonic devices [17,31–33].

As a 2D van der Waals family material, layered perovskites show enhanced stability and structural tunability [17,29,34], but with a particular soft lattice and a dynamically disordered structure. Its crystal lattice typically consists of single or multiple organic–inorganic hybrid phases arranged into a Ruddlesden–Popper structure [18] (as it has been explained in the chapter 1.1). In contrast to 3D perovskites, the semiconducting inorganic layer is passivated with insulating organic cations, forming a 2D natural quantum-well structure where the electronic excitations are confined in the inorganic layers [34]. Its optical emission properties can be controlled by the n value, which labels the number of inorganic monolayers building the quantum well structure (from $n = 1, 2, 3$ to $\sim \infty$) [17,34]. Single layer 2D perovskites show strong Coulomb interaction, due to the effect of the quantum confinement and the weak dielectric screening. Consequently, excitonic states for 2D HPs with a small n number are characterized with binding energies up to several hundreds of meV [29], which returns excitonic stability even at room temperature [60].

The intense excitonic features that are present in these small n value 2D HPs play an important role in the development of new and promising optoelectronic devices. At first, the high excitonic binding energy characteristics of small n values 2D HPs reduces the overall photocurrent generation for solar cell applications [63]. Thus, for these purposes, larger n values samples with smaller excitonic binding energies are conventionally used [21]. However, there is a different carrier strategy to produce high photocurrent generation in 2D HPs with small n values. The dissociation of excitons into Donor-Acceptor pairs (DAP) could be used to drive new device designs with small n value 2D HPs. In fact, DAP charge transfer processes has been ob-

served in $n = 1$ LHPs with interfaced with an organic semiconductor used as spacer layer, which enhances photocurrent production, this is possibly induced by increased disorder and reduced dielectric constant in the bulk heterojunctions system [21]. Interestingly, another study has reported that a molecular doping by a small and highly electron acceptor molecules of 3,4,5,6-tetrachloro-1,2-benzoquinone (TCBQ) into $n = 1$ LHPs containing naphthalene cations molecules serving as a donor, give rise to a formation of DAP within the organic layer [64]. These DAP organic species between the inorganic layers can be used to increase the electrostatic screening of the exciton, and hence to tune the excitonic binding energy in 2D hybrid layered perovskite samples [21,64], which is an important strategy to gain control of the performance of optoelectronic devices. However, the charge transfer has not been observed when using a bulkier Phenethylammonium (PEA) organic cations as layer spacers, which isolate the inorganic sheet and thus inhibit the charge transfer processes at the crystal interface, or when using larger LHPs values than $n > 1$ reducing excitonic character [21]. Moreover, DAP charge transfer processes of intrinsic donor and acceptor defects formed within the inorganic layer of $n \geq 2$ LHPs, intercalated with a small methylammonium (MA) cations and isolated with PEA bulkier spacer cations, presented in this chapter, is different to the previously reported DAP formation caused by external doping of $n = 1$ LHPs [21,64].

The isolated DAP carrier optical recombination that provides very narrow linewidths, as low as $\simeq 120\mu eV$, (here it is important to note that our spectral resolution is $\simeq 120\mu eV$) and long-lived as long as 8.6 ns, optical transitions in 2D LHPs based materials at low temperatures has been measured and identified in this chapter. X-Ray photoemission spectroscopic (XPS) has been employed to identify chemical processes giving rise to elec-

tronic states responsible to DAP-related optical transitions. In particular, the DAP appears to be related to the exchange of methylammonium (MA) molecule and Pb atoms present in 2D HPs samples with phase thickness $n = 2$, leading to optical recombination in a broad spectral range between two excitonic transitions. This claim is supported with complementary optical spectroscopic data by means of μ -Raman spectra. The experimental effort is accompanied with predictions from a simple model to calculate the density of states (DOS) as a function of DAP binding energy, which is built up by the attractive Coulombic interaction between their net charges. The analysis helps to interpret and understand the principal signatures and the nature of the DAP state in 2D LHPs, its spectral features, and its relationship with the selected cation spacer and the layer thickness n value.

4.2 Experimental details

Sample preparation:

Two different phases of 2D perovskites single crystals with the lowest quantum well thickness of $n=1$ and $n=2$ were synthesized. The crystal lattice consists of an inorganic octahedral layer that is sandwiched by long organic cations, forming 2D quantum well structures (see Figure 4.1.a-c). The general chemical formula for 2D perovskites is $R_2A_{n-1}B_nX_{3n+1}$, where R_2 is a long organic cation (phenethylammonium, butylammonium, ethylammonium, ...), A is a tiny organic cation (methylammonium (MA), formamidinium (FA), ...), B is a metal inorganic cation (e.g., lead, tin, and so on), and X is a halide inorganic anion (i.e., chloride, bromide, or iodide) [17–21]. Figure 4.1.a-c shows the crystal structures of both PEA_2PbI_4 ($n=1$) and $PEA_2MAPb_2I_7$ ($n=2$) phases. They are made up of a single layer ($n=1$) and a double layer ($n=2$) of perovskite inorganic octahedral flakes com-

posed by $(PbI_6)^-$ anions sandwiched by long organic $(PEA_2)^+$ cations, which serve as spacers. The inorganic double layer is intercalated by short organic $(MA)^+$ cations for $n = 2$. Only the $n = 1$ phase has a well-defined structure, whereas small inclusions of another n phase are formed for a higher inorganic flake thickness $n > 1$ [38].

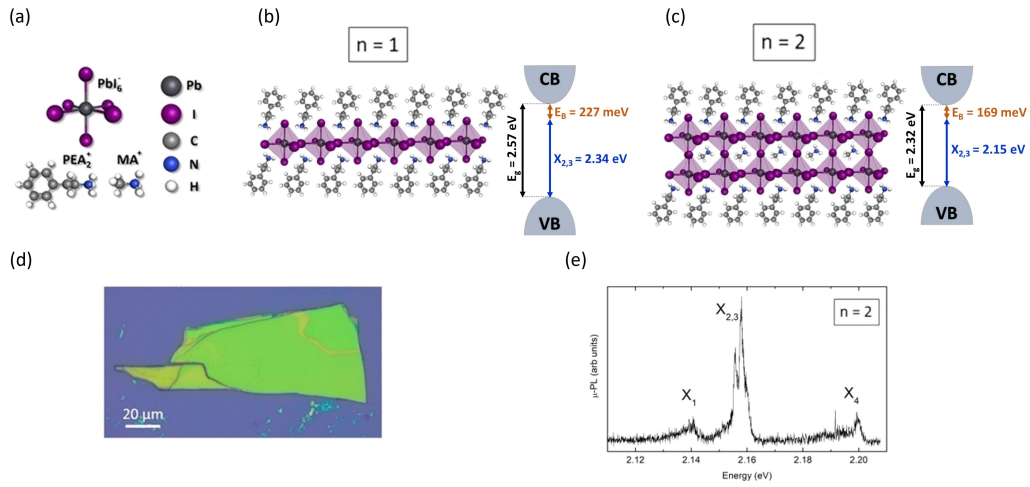


Figure 4.1: (a) 2D perovskites are composed of inorganic octahedral $(PbI_6)^-$, short organic methylammonium $(MA)^+$ cation, and long organic Phenethylammonium $(PEA_2)^+$ cation. (b) Crystal structure of a monolayer of 2D perovskite PEA_2PbI_4 crystal with a quantum well thickness of $n=1$, where a single octahedral sheet is sandwiched by a PEA_2 organic spacer. The inset image shows its energy levels diagram, with indicated valence band (VB), conduction band (CB), electronic band gap (E_g) with values taken from [36], free exciton optical transition ($X_{2,3}$) and the exciton binding energy (E_b). (c) Crystal structure of a monolayer of 2D perovskite $PEA_2MAPb_2I_7$ crystal with a quantum well thickness of $n=2$, consisting of two octahedral sheets intercalated with short MA molecules, sandwiched by a PEA_2 organic spacer. The inset image shows its energy levels diagram, with indicated valence band (VB), conduction band (CB), electronic band gap (E_g) with values taken from [36], free exciton optical transition ($X_{2,3}$) and the exciton binding energy (E_b). (d) Molecularly thin exfoliated flake of 2D perovskites with $n=1$ with tens of μm lateral size. (e) Examples of the micro-PL spectrum containing these excitonic transitions, for $n=2$ sample.

Synthesized crystals can be easily exfoliated down to a single monolayer, thanks to the relatively weak van der Waals interlayer coupling. Exfoliation reduces the occurrence of unwanted hybrid phase formation [38] and leads to a strictly flat crystal orientation to the substrate [39], which may suppress

the substrate's lattice imperfections. In this chapter, synthesized single crystals of both phases were exfoliated onto SiO₂/Si substrates using scotch tape. Exfoliated single-crystal flake ($n = 1$) with a typical lateral size of tens to hundreds of micrometers and a thickness of tens of nanometers is shown in Figure 4.1.d. A confocal microscope has been used to measure μ -photoluminescence (μ -PL) and time-resolved μ -PL (μ -TRPL), (see Chapter 2.11 for more details).

Synthesis:

Synthesis of PEA₂PbI₄ ($n=1$). Solution A, PbO powder (1116 mg, 5 mmol) was dissolved in a mixture of 57% water/water (w/w) aqueous hydriodic acid (HI) solution (5.0 mL, 38 mmol) and 50% aqueous H₃PO₂ (0.85 mL, 7.75 mmol) by heating to boiling under constant magnetic stirring for about 10 min. It was then possible to see the formation of a bright yellow solution. Solution B, in a separate beaker, C₆H₅CH₂CH₂NH₂ (phenethylamine, PEA) (628 μ L, 5 mmol) was neutralized with HI 57% w/w (2.5 mL, 19 mmol) in an ice bath, resulting in a clear pale-yellow solution. If a solid precipitate or the formation of a suspension is observed, then it is possible to heat slightly until it has dissolved. Once both solutions have been prepared, Solution B should be slowly added to Solution A. A quick addition could produce a precipitate, which was subsequently dissolved as the combined solution was heated to boiling. After 10 minutes of maintaining the solution at boiling point, the stirring was stopped, and the solution was allowed to cool down to room temperature. During this time, orange, rectangular-shaped plates began to crystallize. The crystallization was deemed to be complete after 1 hour. The crystals were isolated by suction filtration and thoroughly dried under reduced pressure. The obtained single crystals were washed with cold diethyl ether.

Synthesis of $\text{PEA}_2\text{MAPb}_2\text{I}_7$ ($n=2$). Solution A, PbO powder (1116 mg, 5 mmol) was dissolved in a mixture of 57% w/w aqueous HI solution (5.0 mL, 38 mmol) and 50% aqueous H_3PO_2 (0.85 mL, 7.75 mmol) by heating to boiling under vigorous stirring for about 5 min and forming a yellow solution. Then, $\text{CH}_3\text{NH}_3\text{Cl}$ powder (169 mg, 2.5 mmol) was added very slowly to the hot yellow solution, causing a black precipitate to form, which rapidly redissolved under stirring to achieve a clear bright yellow solution. Solution B, in a separate beaker, $\text{C}_6\text{H}_5\text{CH}_2\text{CH}_2\text{NH}_2$ (PEA) (880 μL , 7 mmol) was neutralized with HI 57 % w/w w/w (2.5 mL, 19 mmol) in an ice bath, resulting in a clear pale-yellow solution. The addition of the PEAI solution to the PbI_2 solution initially produce a black precipitate, which was dissolved under heating the combined solution to boiling. After discontinuing the stirring, the solution was cooled to room temperature, and cherry red crystals started to emerge. The precipitation was deemed to be complete after ~ 1 h. The crystals were isolated by suction filtration and thoroughly dried under reduced pressure. The material was washed with cold diethyl ether.

4.3 Results

4.3.1 Micro-photoluminescence and time decays

The unambiguous identification of the nature of the excitonic states which takes place in the 2D perovskites optical spectra is still under study in the academic community. The excitonic-level structure is described and calculated by Do et al. [61] by resulting in four different bright excitonic transitions ($X_1, X_2, X_3, \& X_4$) (see Figure 4.2 three examples of excitonic spectra), where the X_2 and X_3 states are energetically split into two lin-

early polarized optical transitions. This additional splitting has been linked to exciton fine-structure splitting [62]. This excitonic assignment is followed here, based on the optical spectroscopic findings. Recently, Do et al. [61] demonstrated how spin-orbit coupling splits the excitonic transition in 2D halide perovskites into this four distinct recombination routes. Figure 4.1.f shows an example of the micro-PL spectrum containing these excitonic transitions, for $n=2$ sample. As is shown, the emission from X_1 and X_4 transitions are very weak compared to the central emission from X_2 , and X_3 . The analysis of the spectral characteristics for the first three excitonic transitions (X_1 , X_2 , and X_3), for both $n=1$ and $n=2$ samples, was the main focus of this chapter.

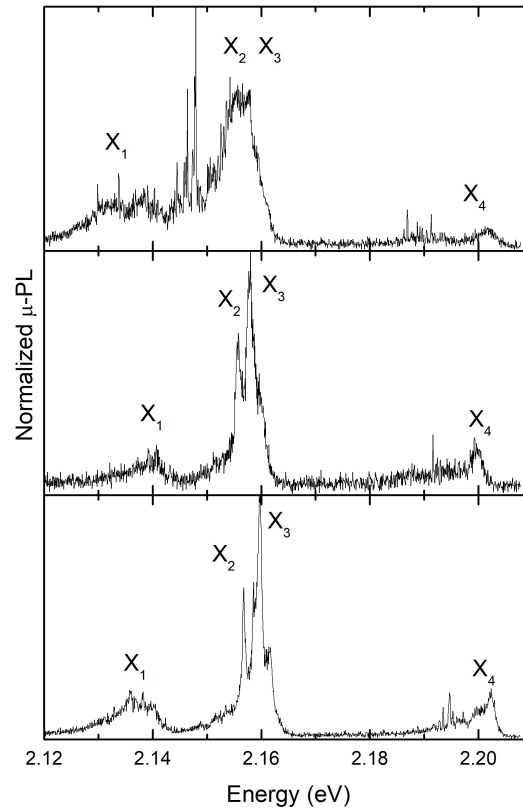


Figure 4.2: Three examples of the μ -photoluminescence spectrum of $n = 2$ 2D perovskite, showing all four excitonic transitions

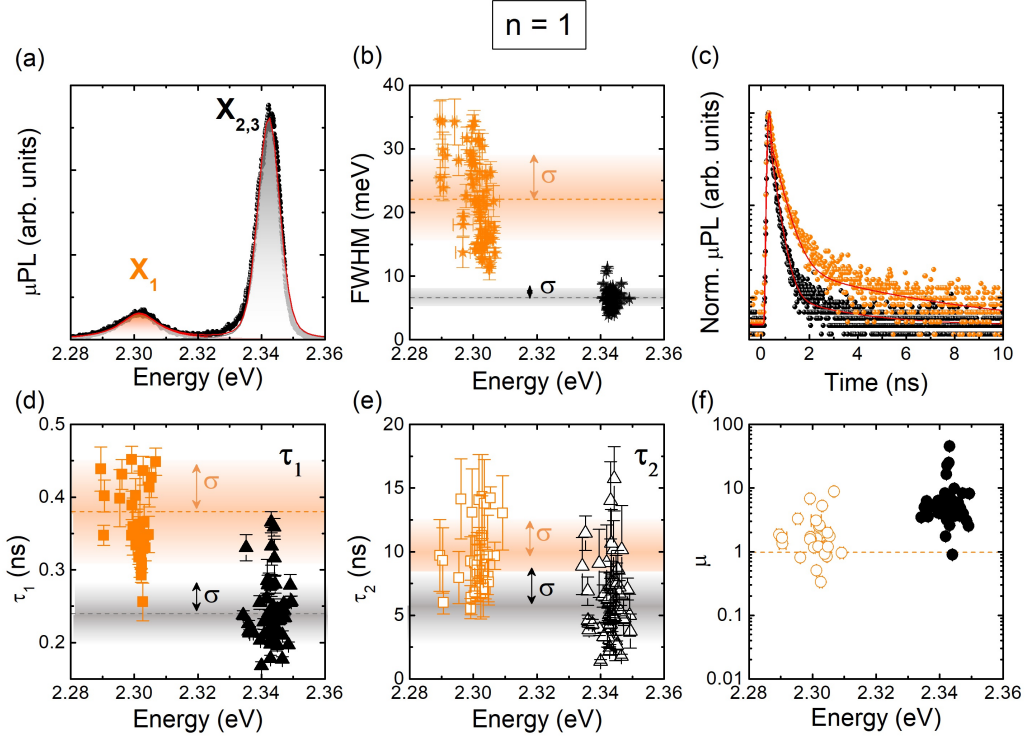


Figure 4.3: General photoluminescence (PL) and time resolved photoluminescence (TRPL) characteristics at low temperature (4 K). An example of measured PL spectra for phase (a) $n=1$. $X_{2,3}$ corresponds to free exciton, and X_1 corresponds to self-trapped exciton. Statistics of X_1 and $X_{2,3}$ peak linewidth FWHM as a function of emission energy of X_1 and $X_{2,3}$ for phase (b). Example of TRPL of X_1 and $X_{2,3}$ on a 10 ns time scale for phase (c). Statistics of X_1 and $X_{2,3}$, fast decay (τ_1) for phases (d), and long decay (τ_2) for phases (e). Statistics of the relative intensity between both fast and slow radiative channels of X_1 and $X_{2,3}$, (μ) as a function of emission energy for phases (f).

Figure 4.3.a displays a typical optical spectrum for the $n=1$ phase samples covering this spectral range of interest. Here, the free exciton recombination is tentatively identify by the $X_{2,3}$ peak (see right panel of Figure 4.1.b-c) [65, 173]. However, the exciton may recombine by another process, (e.g., self-trapped excitons (TE), biexcitons, triexcitons, or phonon replicas) or extrinsic optical transitions as excitons bound to defects [29]. Figure 4.3.b shows the evolution of the FWHM as a function of the emission energy for both X_1 and $X_{2,3}$. $X_{2,3}$ (Black star) shows a mean FWHM = 6.5 meV with standard deviation $\sigma = 1.48$ meV. X_1 (Orange star) data returns

a mean FWHM = 22.1 meV and $\sigma = 6.8$ meV. When analyzing X_1 and $X_{2,3}$ recombination in samples with $n = 1$, both transitions are clearly differentiated by their spectral characteristics. Figure 4.2.c shows a μ -TRPL measurement example for both X_1 and $X_{2,3}$ transitions present in the $n = 1$ phase. TRPL is characterized by two decay channels (characterized with fast τ_1 and slow τ_2 decay times). $X_{2,3}$ shows a first fast decay time in the order of 0.241 ± 0.006 ns and X_1 of 0.393 ± 0.019 ns. Figures 4.3.d-e show a statistical sampling of the decay time measurement for both fast and slow components. The mean-value of $X_{2,3}$ τ_1 is 0.24 ns, with a $\sigma = 0.04$ ns; while for X_1 is 0.38 ns, with a $\sigma = 0.07$ ns. Additionally, the residual long τ_2 shows mean-value of 6 ns for $X_{2,3}$ transition, with $\sigma = 2.8$ ns; while for X_1 it reaches a mean value of 9.5 ns, with $\sigma = 2.7$ ns (Figure 4.3.e). Finally, the relative intensity between both fast and slow radiative channels was analyzed. To do this, a new parameter (μ) is defined to compare the weight of the emitted light from both radiative channels. Hence, it is defined as $\mu = \frac{I_F(T)}{I_S(T)}$, where $I_{F/S}(T) = \int_{t=0}^{t=T} a_1 \exp^{-t/\tau_1/\tau_2} \cdot dt$, and T is the laser period. In this sense, the μ value will describe situations where the fast decay dominates ($\mu > 1$), both channels have similar contribution ($\mu \sim 1$), or where the slow decay dominates ($\mu < 1$). As is shown in the plot in Figure 4.3.f, $\mu > 1$ for almost all cases, both for X_1 (open orange circles), and $X_{2,3}$ (filled black circles). In conclusion, in samples with phase $n=1$, the light intensity contribution from the fast decay time (\simeq hundreds of ps) always dominates over the long decay time (\simeq ns).

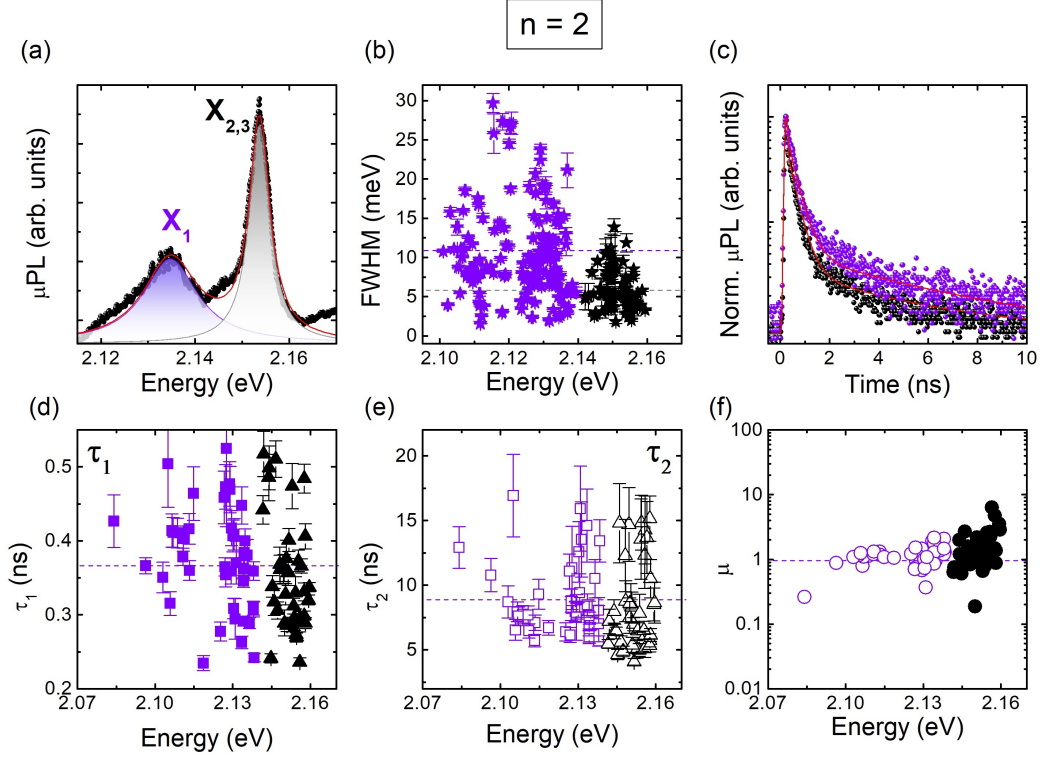


Figure 4.4: General photoluminescence (PL) and time resolved photoluminescence (TRPL) characteristics at low temperature (4 K). An example of measured PL spectra for phase (a) $n=2$. $X_{2,3}$ corresponds to free exciton, and X_1 corresponds to self-trapped exciton. Statistics of X_1 and $X_{2,3}$ peak linewidth FWHM as a function of emission energy of X_1 and $X_{2,3}$ for phase (b). Example of TRPL of X_1 and $X_{2,3}$ on a 10 ns time scale for phase (c). Statistics of X_1 and $X_{2,3}$, fast decay (τ_1) for phases (d), and long decay (τ_2) for phases (e). Statistics of the relative intensity between both fast and slow radiative channels of X_1 and $X_{2,3}$, (μ) as a function of emission energy for phases (f).

Now, a similar analysis is carried out in thicker samples with phase $n = 2$, presented in the following. Figure 4.4.a shows an example of the μ -PL spectra of a representative sample. As before, the first three excitonic transitions are the main focus of the attention. Following similar arguments as described earlier, these are labeled as X_1 , X_2 and X_3 transitions. The increase of the thickness of the inorganic component red shifts their optical emission (see Figure 4.1.f). The $X_{2,3}$ transition is shifted almost 200 meV towards low energy concerning its $n = 1$ counterpart, due to its correspond-

ing thicker inorganic confinement layer. Figure 4.4.b shows X_1 (Violet star) and $X_{2,3}$ (Black star) FWHM values as a function of the emission peak energy, where the $X_{2,3}/X_1$ mean FWHM is 5.7/10.4 meV, with the standard deviation $\sigma = 2.5/5.8$ meV. Here, a larger linewidth dispersion than in the previous statistical analysis, with $n = 1$, is clearly identified. Next, the time decays are analyzed. Figure 4.4.c shows one example of the X_1 and $X_{2,3}$ μ -TRPL measurements, displaying the same double component for both X_1 and $X_{2,3}$ peaks as in the $n = 1$ phase. Figures 4.4.d,e show the statistics of the fast (τ_1) and slow (τ_2) decay times for both X_1 and $X_{2,3}$ transitions. The mean τ_1 value of $X_{2,3}$ is 0.35 ns, with a $\sigma = 0.07$ ns; while for X_1 is 0.38 ns, with a $\sigma = 0.07$ ns. The mean τ_2 value of $X_{2,3}$ is 8.4 ns, with a $\sigma = 3.5$ ns; while for X_1 is 8.8 ns, with a $\sigma = 2.8$ ns. The principal difference between $n = 1$ and $n = 2$ μ -TRPL is the higher observed dispersion for the $n = 2$ phase case, although here mean values are slightly larger than previously. Finally, and as before, the relative intensities of both radiative channels with the parameter μ have been analyzed. Figure 4.4.f shows the dispersion of μ for the phase $n = 2$. As is shown, almost all values are situated close to $\mu \sim 1$ or $\mu > 1$. This means that the fast channel still dominates the optical emission in both $X_{2,3}$ (filled black circles) and X_1 (open violet circles). In a small fraction of cases, the contribution of the slow component dominates ($\mu < 1$). This more complex behaviour adds to the previous findings related to the larger dispersion found for both FWHM, and τ_1 and τ_2 decays. The study on the transient characteristics of the photoluminescence clearly identifies higher complexity when analyzing the $n = 2$ phase than the previous and simpler dynamical situation described in the $n = 1$ phase.

4.3.2 Donor-Acceptor pair optical emission

The higher complexity that is observed in both FWHM and decay time statistics for the $n=2$ phase is accompanied in some cases ($\approx 11\%$ of analysed points across surfaces of different flakes) with the presence of a third and narrow optical transition, in which central peak energy position ranges between X_1 and $X_{2,3}$ optical transitions (see Figure 4.5.a,c,&e). The spectral and decay time characteristics of this third optical transition are presented in this section. It is labeled as a Donor-Acceptor Pair (DAP) state. Later on, additional experimental evidences to support this assignment will be presented. Figures 4.5.a,c&e show μ -PL spectra of $n = 2$ phase samples, where the DAP transition is present. Multi-Lorentzian fitting was performed for each spectrum. The contribution of X_1 and $X_{2,3}$ optical emission is shown with violet and black shadows. Blue shadows indicate the emission from DAP transition, with characteristic FWHMs ranging from 120 μeV (Spectral resolution) up to $\simeq 5$ meV. The FWHM & E_B pairs of the Figure 4.5.a,c&e take the following values—a: 0.12 meV & 0.172 eV, c: 0.3 meV & 0.173 eV, and e: 0.8 meV & 0.170 eV (as shown by the statistics of DAP peak linewidth as a function of E_B in Figure 4.7), which E_B is defined as $E_B = E_{gap} - \hbar\omega$. Where E_{gap} is the gap energy of the $n = 2$ phase, which is 2.32 eV (see the right panel of Figure 4.1.c), and $\hbar\omega$ is the energy of the emitted photon in a DAP transition. Here the μ -TRPL measurements of DAP transitions is performed. Figures 4.5.b,d&f show the X_1 and $X_{2,3}$ time traces following the same evolution described earlier. However, the sharp DAP transition present in this phase shows quite different behaviour. The DAP dynamics (plotted with blue scattered dots) also contain both fast and slow decay times. Nonetheless, here the slow decay represents the dominant intensity contribution. Figure 4.5.g shows the evolution of μ as

a function of E_B . As can be seen, there is a clear energy range where the radiated intensity from the slow decay channel clearly dominates over the fast decay ($\mu < 1$), where this last fast decay contribution is almost negligible; this energy range is marked with a bluish shadow in the Figure 4.5.g,h. In the Figure 4.5.g dot label with (I) is linked to the spectra shown in the Figure 4.5.a, and the μ -PL and μ -TRPL peaks associated with (II) and (III), are shown in the Figure 4.6.a,b and 4.6.c,d, respectively. The residual presence of the fast decay when filtering the DAP transition can be associated with the background emission from X_1 and $X_{2,3}$ transitions. Figure 4.5.h shows a statistical sample of DAP τ_1 and τ_2 values as a function of E_B . It can be assumed that the DAP optical transition is characterized by longer time dynamics, which is in correspondence with its sharpest spectral features. However, neither decay and FWHM are Fourier transform related, and hence the effect of the extra carrier dynamics mechanism in the DAP recombination should be expected, even though the limited spectral resolution ($\simeq 120\mu eV$) reduces the capacity to estimate the real FWHM values. To obtain the full description of the characteristics and magnitude of the correlation time and dephasing process acting on the DAP transition, it will be necessary to perform alternative interferometric measurements to derive its first order coherence function [174].

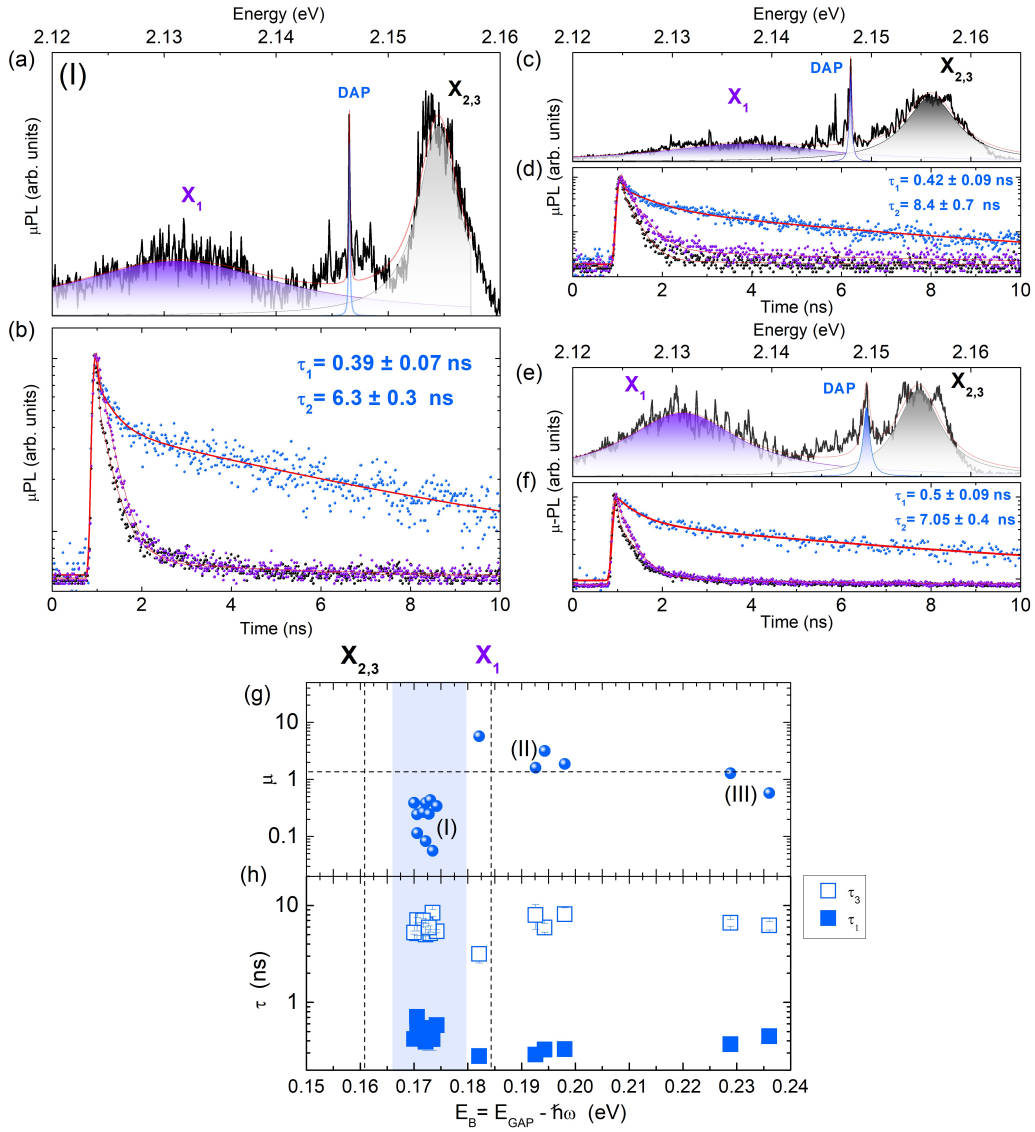


Figure 4.5: Donor Acceptor Pair (DAP) optical emission signatures in $n = 2$ phase samples. (a-c-e) μ -PL spectra of three different samples with highlighted X_1 (violet color), $X_{2,3}$ (black color), and ionized Donor-Acceptor pair emission peaks (DAP, blue color), (b-d-f) their corresponding μ -TRPL traces of the observed $X_{2,3}$ (black scattered dots), X_1 (violet scattered dots), and DAP (blue scattered dots) optical transitions. (g) Statistics of the relative intensity between both fast and slow radiative channels, (μ) as a function of its binding energy for the DAP transition. ((I) is linked to (a), and the μ -PL and μ -TRPL peaks associated with (II) and (III), are shown in Figure 4.6.a,b, and Figure 4.6.c,d, respectively). (e) Statistics of the fast (τ_1) and slow (τ_2) decay times as a function of the binding energy of the DAP state.

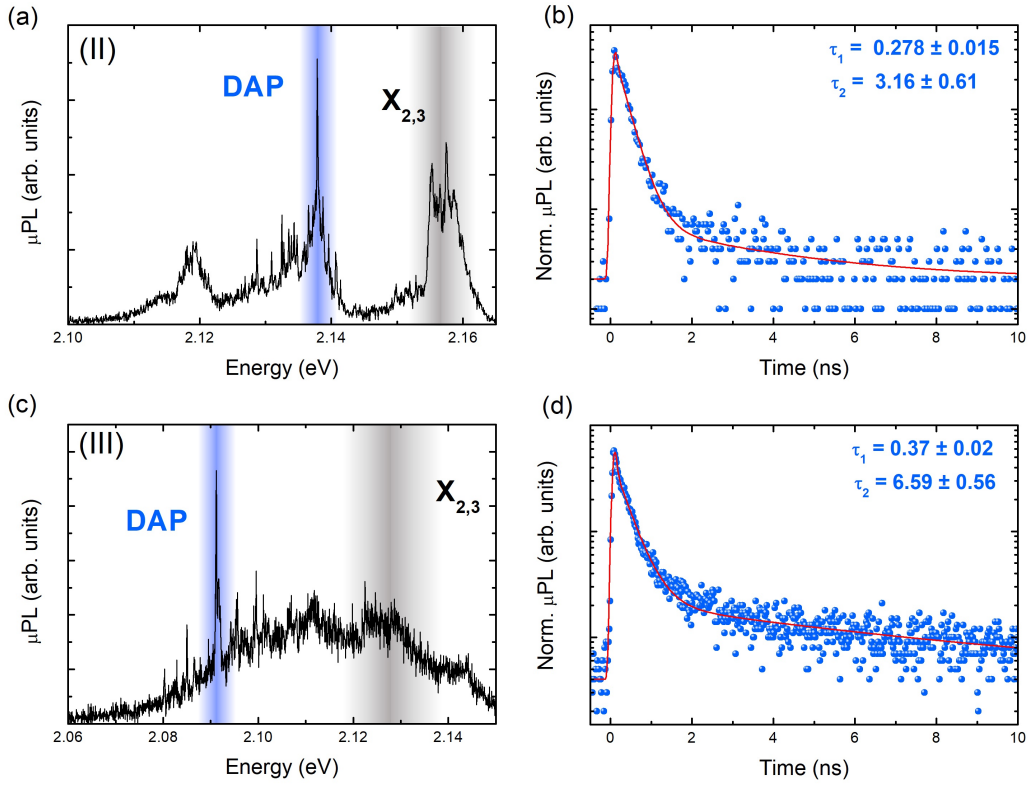


Figure 4.6: (a) μ -PL spectra with highlighted $X_{2,3}$ emission peak (black color) and ionized Donor-Acceptor pair emission peak (DAP, blue color) with the label of (II) with the binding energy of 0.182 eV, as shown in Figure 4.5.g. (b) μ -TRPL traces corresponding to the observed DAP optical transition in (a). (c) μ -PL spectra with the label of (III) with the binding energy of 0.23 eV, as presented in Figure 4.5.g. (d) μ -TRPL traces corresponding to the observed DAP optical transition in (c).

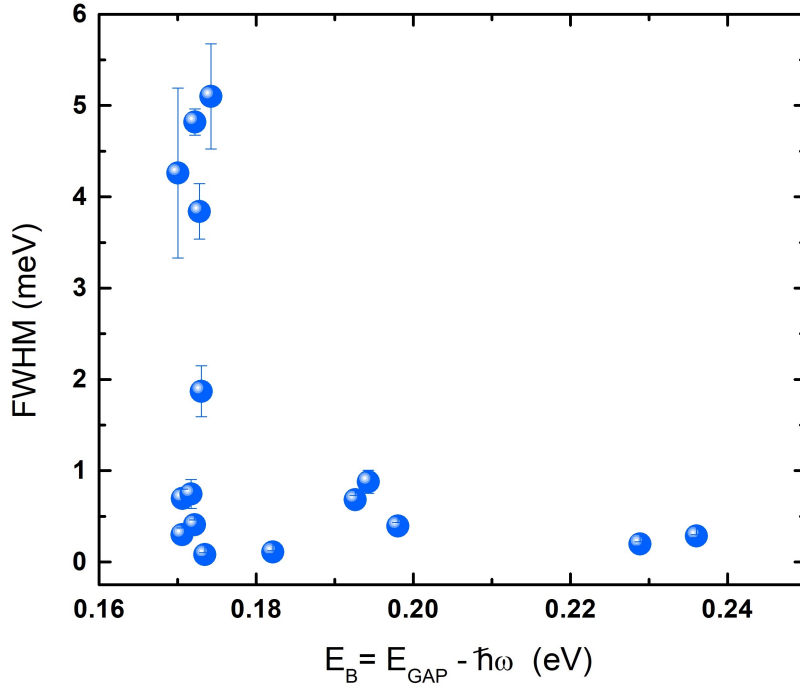


Figure 4.7: Statistics of DAP peak FWHM as a function of E_B for phase $n=2$

Photoelectronic characterization:

XPS experiments have been performed to identify the electronic states that originate the DAP transition. Figures 4.8.a-c show the Pb 4f, I 3d, and N 1s core level spectra acquired in both phases $n = 1$, $n = 2$ and in a reference bulk sample. These measurements are expected to provide for direct information about the oxidation degree and chemical environment of each atomic species. In the bulk samples, Pb 4f and I 3d core-level spectra are dominated by Pb^{+2} and I^{-1} spin-orbit doublets with a $Pb4f_{7/2}$ component located at 138.1 eV and a $I3d_{5/2}$ component at 618.7 eV, respectively (Figures 4.8.a-b). These components are attributable to Pb and I atoms in the inorganic octahedral anions. Together with the main Pb^{+2} core-level signal, it has observed traces from Pb^0 (with its $Pb4f_{7/2}$ component located at 135.9 eV), which reveals the presence of metallic Pb segregated to the

surface of the bulk sample (Figures 4.8.a). As in bulk samples, traces from Pb^{+2} and Pb^0 species have been observed in the Pb 4f and I 3d core-level spectra acquired in the n=2 sample.

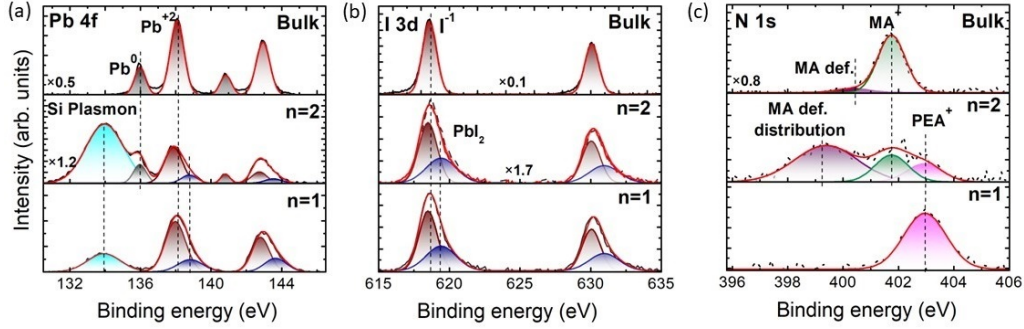


Figure 4.8: XPS spectra of (a) Pb 4f , (b) I 3d and (c) N 1s core-levels measured in $n = 1$, $n = 2$ and bulk lead iodine perovskite crystal phases. The broad peak appearing on the low binding energy side of Pb 4f spectra for $n = 1$ and 2 samples (shaded in light blue), corresponds to the second replica of the Si 2p plasmon (plasmon energy of ~ 17.8 eV from Si $2p_{3/2}$). XPS analysis results (a-c) suggest that different composition of organic components in each n and bulk crystal phases give rise to creation of different kinds of defects.

However, additional Pb 4f and I 3d doublets have been found, these appearing at the high energy side of the main Pb^{+2} and I^{-1} doublets with their $Pb4f_{7/2}$ and $I3d_{5/2}$ components located at 138.9 eV and 619.5 eV, respectively (Figures 4.8.a-b). These results, together with the fact that these new Pb 4f and I 3d components exhibit an atomic Pb/I ratio of $\sim 0.3 \pm 0.1$, suggests that their origin may be related to the presence of PbI_2 -like species at the sample surface, and also μ -Raman spectroscopy results shown in Figure 4.10 support this assignment. The $n=1$ samples (Figures 4.8.a-b), which were used to measure the Pb 4f and I 3d core-levels, and spectra reveal the presence of Pb and I atoms in PbI_2 -like species coexisting with these located in the inorganic octahedral anions. However, no traces from metallic Pb^0 have been observed, interestingly.

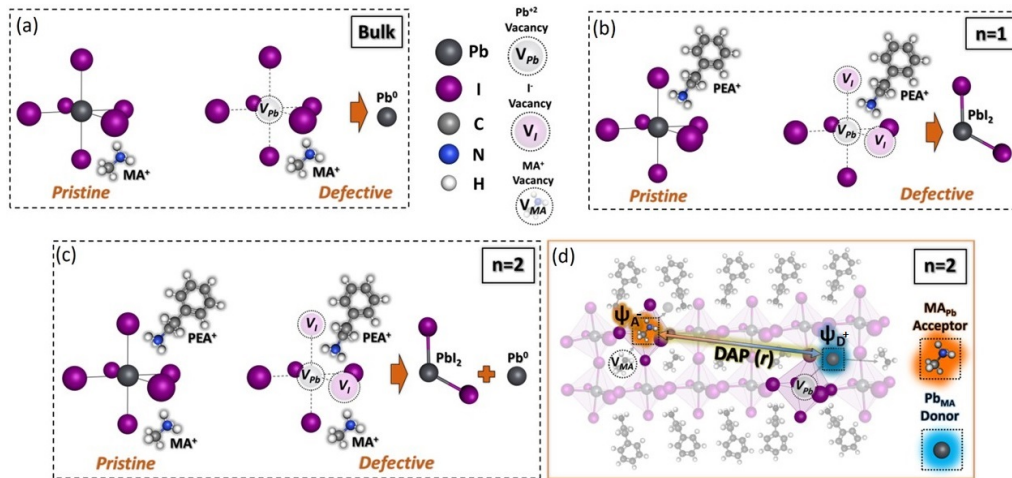


Figure 4.9: (a-c) Simplified scheme of ideal and defective PbI_6 octahedra units surrounded by different compositions of organic cations for each crystal phase with corresponding defects identified by XPS. Results indicate that (a) MA^+ cations present in bulk crystals seem to promote metallic Pb^0 segregation generating Pb vacancies (V_{Pb}), whereas (b) PEA_2^+ cations in $n=1$ crystal phase tend to decompose inorganic sheets into lead iodine PbI_2 -like species favouring the generation of V_{Pb} and I vacancies (V_I). (c) Coexistence of both MA^+ and PEA_2^+ cations in $n=2$ crystal phase enhances in multiple defect generation. (d) The joint action of both MA^+ and PEA_2^+ cations in $n=2$ crystals promotes the generation of MA_{Pb} acceptors, besides of Pb_{MA} donors. As a consequence, these two kind of defects tend to form DAPs with a recombination emission energy that depends on their distance r .

Figures 4.9.a-c. show comparison of simplified schemes of ideal and defected PbI_6 octahedra units (including different organic cation types) for each crystal XPS analysis (see Figure 4.8.a-c). These photoemission results indicate a different chemical behavior as going from one kind of samples to the other, which imply a rich structural-dependent chemical activity. Of course, Pb 4f and I 3d spectra appear dominated by signals coming from (pristine) inorganic octahedral sheets in all kind of samples (Figure 4.9.a-c). However, metallic Pb^0 has been detected, but not PbI_2 -like species, in the bulk samples (Figure 4.9.a) and PbI_2 -like species, but not metallic Pb^0 , in the $n=1$ samples (Figure 4.9.b). Only in the $n=2$ samples both metallic Pb^0 and PbI_2 -like species coexist (Figure 4.9.c). Structurally, these samples differ one from each other, precisely, in the nature of their organic

components: MA^+ cations constitute the organic species in bulk samples, whereas PEA_2 ones are those of the $n=1$ samples. These facts suggest that different organic components give rise to defects of different chemical nature: MA^+ cations somehow promote segregation of metallic Pb^0 whereas PEA_2 cations tend to favor decomposition of inorganic sheets to produce PbI_2 -like species.

Perovskites can naturally host a wide variety of optically active defects whose optical recombination energy depends on their chemical nature [60]. For instance, several defects acting as acceptors (I_i , MA_{Pb} , V_{MA} , V_{Pb} , I_{MA} , I_{Pb}) or donors (MA_i , Pb_{MA} , V_I , Pb_i , MA_I , Pb_I) have been found in 3D [175–177] and 2D [37] LHPs (here, V = vacancy, subscript i = interstitial, and A_B denotes A substitutes for B) [176]. Taking this into account, XPS results reported here reveal a rich n-dependent chemical activity in 2D perovskites, which would give rise to optically active defects whose nature would depend on the specific organic component involved in. This fact becomes particularly relevant for disentangling optical properties of 2D perovskites with $n=2$, in which both PEA_2 and MA^+ organic cations coexist in a similar proportion (see Figure 4.1.c and Figure 4.9.c). In fact, it is thought that a joined action of the two organic cations present in the $n=2$ perovskites is responsible for the generation of DAPs in 2D perovskites with $n=2$ depicted in (Figure 4.9.d): MA^+ cations seem to promote Pb segregation, but the presence of PEA_2 cations, which strongly disturb the inorganic sheet, collaterally enhances Pb segregation favouring that MA^+ cations to occupy Pb atomic sites within the octahedrals and creating MA_{Pb} acceptors [37]. At the same time, displaced Pb atoms may occupy MA^+ sites out of the octahedrals, eventually acting as Pb_{MA} donors. It seems reasonable to assume that the effects of both cations was particularly efficient

when acting on the same sites of the crystals, then, it would be expected that MA_{Pb} -related acceptors and Pb_{MA} -related donors are close to each other. As a result, first the donor and acceptor must be neutralized. Then, they will emit a photon, and in the final state, the wavefunctions of MA_{Pb} -related acceptors and Pb_{MA} -related donors will easily interact, producing DAPs (see Figure 4.9.d).

The N 1s core-level spectra Figure 4.8.c, as measured by XPS in 2D perovskites, seem to support the scenario proposed above. In the samples, the N 1s signal stems from the organic components of the 2D perovskites. In fact, in the bulk and in the 2D perovskite with $n=1$, the dominant N 1s singlet signal comes from the MA^+ and PEA_2 cations, respectively. Only an additional weak signal can be observed at the low energy side of the N 1s spectrum measured in the bulk sample, which may be attributed to MA^+ cations in Pb sites (hereafter called the MA^+ defective). Indeed, the N 1s spectrum acquired in the 2D perovskite with $n=2$ exhibits both peaks coming from the MA^+ and PEA_2 cations located at their own crystal sites. However, a new component develops, as the Pb 4f component attributed to PbI_2 also does (Figure 4.8.a) tentatively attributed to the aforementioned MA^+ defective as these two components appear in the low energy side of the N 1s spectra. Moreover, in the $n = 2$ sample, the N 1s contribution of MA^+ defects is shifted to lower binding energies than in the bulk perovskite, indicating that PEA_2 promotes the exchange of MA^+ cations with Pb in octahedral sites favouring MA^+ to act as acceptors. Figure 4.9.d shows an example of DAP formation of Pb_{MA} and MA_{Pb} anti-sites defects created in $n=2$ perovskites [37]. Influence of DAP distance r and concentration of created individual DAP to their optical recombination properties, will be discussed in the section 4.4.

μ -Raman spectroscopy:

μ -Raman spectroscopy is a powerful technique for studying the crystal quality of 2D materials. Laser power dependent Raman spectra of 2D HPs with phase thickness of $n = 1$ and $n = 2$ is depicted in Figure 4.10.a and b, respectively. For both phases, two intense peaks centers at 102 cm^{-1} and 132 cm^{-1} were identified. The lower frequency peak is associated to the PbI_2 [178, 179] and the higher frequency peak to the organic cation [178] vibrations.

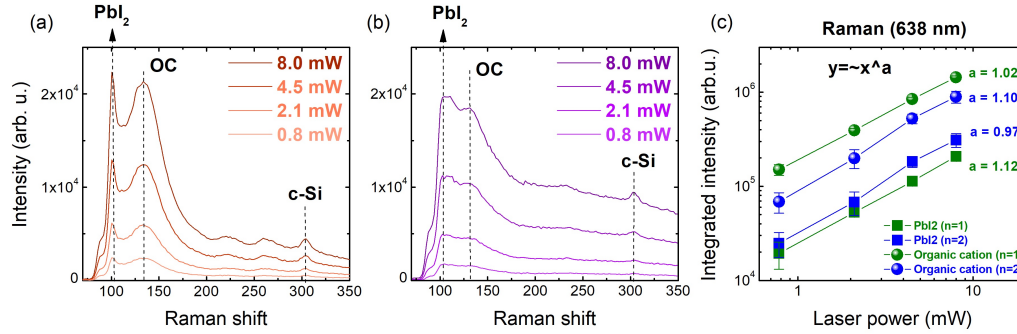


Figure 4.10: Raman spectra of phase (a) $n = 1$ and (b) $n = 2$ 2D HPs as a function of laser power with marked peaks attributed to PbI_2 , organic cation (OC) and c-Si vibration modes. (c) Raman integrated intensity of the PbI_2 and organic cation related peaks as a function of the laser power for both phases showing a linear dependency as a function of laser power.

Figure 4.10.c shows the integrated intensity as a function of excitation power of the Raman spectra of PbI_2 and the organic cation peaks, for $n=1$ and $n=2$ phases. As it is shown, the evolution follows a linear power dependency for both phases (value a is around 1). By a closer examination of the Raman spectra (see Figure 4.10.a-b) it can be found that the peak related to the vibration of the organic cation is relatively broad, with FWHM around 40 cm^{-1} for both phases $n = 1, 2$. On the other hand, the lowest frequency peak attributed to vibration of the PbI_2 shows more differences between $n = 1, 2$ phases. The PbI_2 related peak is sharper for $n = 1$ (FWHM = 8

cm^{-1}) than for $n = 2$ (FWHM=15 cm^{-1}), suggesting a noticeable better crystal quality of $n = 1$ phase.

4.4 Discussion

With the intention of evaluating the starting hypothesis of addressing these μ -PL and μ -TRPL special features found in the $n = 2$ phase with the DAP state, as suggested by XPS and μ -Raman spectroscopy techniques, I first compare the optical emission results with a simple model to calculate the DAP Density of States as a function of its binding energy in 2D perovskites (see Chapter 1.1). Following this procedure, the possibility of finding sharp-peaked transitions along the energy range between X_1 and $X_{2,3}$ will be estimated. To develop the model, we assume the existence of donor (D) and acceptor (A) states within the bandgap. According to Ref. [180], the substitution defects of MA and Pb leads to D and A states below and above the conduction and valence band edges of approximately $\simeq 0.15$ eV. [181] The energy of the emitted photon in a DAP transition ($E_{SP}(r)$) is given by Equation 1.10.

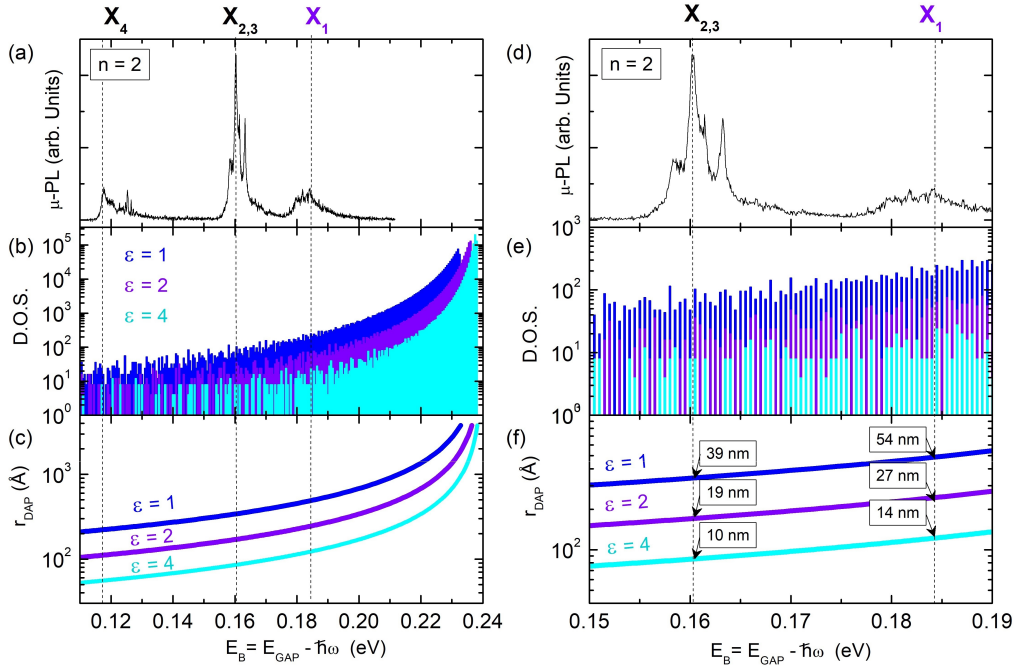


Figure 4.11: (a) Example of a spectra labeled as a x_1 , $X_{2,3}$, & X_4 , to show the positions of the exciton transitions. (b) Model output of the DAP density of states (DOS) as a function of binding energy, in logarithmic scale for three different dielectric constants. (d, e and f) is the zoom of (a, b, and c), from 0.15 to 0.19 eV, respectively.

Figure 4.11.a depicts a μ -PL spectra for the phase $n = 2$ labeled as a X_1 , $X_{2,3}$, & X_4 , to indicate the position of the exciton transitions. For the calculations, a two-layers 2D perovskite was assumed in order to simulate the case with phase $n = 2$. The density of states (DOS) is obtained by calculating E_{SP} for all possible distance between an electron in the donor site and the hole in the acceptor site. Figure 4.11.b shows the DOS as a function of a binding energy (E_B) for three different values of the dielectric screening ϵ . The first situation, $\epsilon = 1$ represents the unscreened situation, which is typical of molecules. As evidenced by the DAP peaks with energy position close to the $X_{2,3}$ peak, the dielectric screening of the studied samples would be between 2 and 4, showing discrete DAP peaks for the range between X_1 and $X_{2,3}$ transitions. So the binding energy is around 0.16, 0.18

eV, which is zoomed in Figure 4.11.e to show clearly the energy where the picks are. Figure 4.11.c depict the DAP separation as a function of E_B from 0.11 eV to 0.24 eV; at the energy of 0.24 eV, the energies of the donor and acceptor are in the infinite radius. The energy decreases as the radius rises. Hence, the binding energy decreases as the Coulomb interaction reduces as the final state is separated, and eventually it will achieve the same energy as the donor acceptor without the Coulomb interaction. The numbers for the stream of the $X_{2,3}$ and X_1 positions are clearly displayed in Figure 4.11.f, and as you can see, the radius ranges are from 10 nm to 54 nm.

4.5 Conclusions

The analysis made in this chapter shows that the research on DAP in 2D materials represents a growing field with high potential for manipulating and controlling spin states by engineering emitters with a well-defined donor-acceptor distance and orientation [182–184]. The observation of narrow and discrete PL lines associated with DAP transitions with dramatically slow decay times is added to recent reported properties, such as exciton binding energy tunability by donor acceptor interactions [64] and DAP single photon emission performance in 2D hBN [184]. It showed that the two organic components present in the n=2 sample promoted the formation of the defects responsible for the DAP transition using XPS spectroscopy, as it has shown and reported by the XPS spectroscopy characterization. In detail, the coexistence of MA^+ and PEA_2 cation, giving rise to Pb segregation, causing the inorganic lattice sheet distortion, might favour the displacement and exchange of MA^+ and Pb atoms, hence the formation of MA_{Pb} acceptor and Pb_{MA} donor states. The model predicts the presence of low density DAP states in the spectral range close to the $X_{2,3}$ emission,

and hence both low DOS and large donor acceptor wavefunction separation explain the measured DAP narrow optical transitions with nanosecond lifetimes. To provide a future application based on the control of these states, specific sample preparation routes should be designed to control and optimize the DAP state population, localization, or isolation. Due to its featured spectral properties, along with their high photoluminescence brightness, the DAP state in 2D Perovskites represents an interesting electronic state to be considered for the development of the emerging field of quantum technologies [185, 186].

Chapter 5

Light-Matter interaction and Light mode coupling in an open-access fiber based optical microcavity

In the recent decade, optical microcavities have attracted a great deal of interest in a broad range of research fields. The monolithic structure of most microcavities, such as Fabry-Perot (FP) or whispering-gallery-mode (WGM) resonators, lack the capability of large-range spectral and spatial tuning. As an alternative, an open-access microcavity system combines several advantages: realization of small mode volume, large-range tunability, flexible structural engineering, and easiness of integration with external emitters. Thus, this fiber-based cavity system results from an outstanding scheme to implement a new physics and potential applications such as polariton simulators [187], Bosonic condensation [188] phase transition in 2D driven open quantum systems [189] and thermal decoherence of a nonequi-

librium polariton quantum fluid [190] which are promising candidates for the future development of the exciting field of quantum technologies.

Here, in addition to exploring how open access fiber-based microcavity modes interact with perovskite materials at room temperature, a detailed numerical investigation is presented in order to clearly comprehend any potential coupling between leaky optical modes of a FP cavity (weakly confined cavity modes) and the standing optical modes in one of the FP mirrors (DBR Bloch modes (BM)). In this chapter, experimental spectroscopic features of this light mode coupling are presented, as well as the simulation of a model based on COMSOL Multiphysics.

5.1 Introduction

The resonant coupling between ensembles of quantum emitters and a confined electromagnetic field is a rapidly expanding field of study, because it allows for a controlled effect on the coupled matter's properties (i.e. spontaneous emission). The concept of control over spontaneous emission of the quantum system by coupling it to a confined electromagnetic (EM) field was first introduced by Purcell [100]. Spontaneous emission (SE) is not entirely dependent on the properties of matter. More appropriately, in such a way that properties of matter can be manipulated by placing it inside resonant a cavity [191–193]. The Purcell effect can enhance the SE in the cavity in the weak coupling regime (details in chapter 1.2), however when matter becomes strongly coupled (see chapter 1.2) with a light mode, its fundamental properties can change [194].

However, there is another possibility in cavities where cavity modes can strongly couple to other light modes, for instance in Fabry-Perot microcavities in which cavity modes can be coupled with optical modes inside

the distributed Bragg reflectors (DBRs). Researchers are becoming more interested in layering structures with periodically modulated refractive indices in one dimension, also known as Distributed Bragg Reflectors (DBRs). This is due to the ability of periodic layered structures (DBRs) to control photon flows via photonic band gaps, which are photonic analogs of energy band gaps in semiconductors. Because of the photonic band gap in DBRs, there are allowed and forbidden frequency ranges for transmission, resulting in the support of some light modes with these types of structures. The interaction of these DBR modes with the cavity modes may also result in strong coupling (strong coupling between two light modes).

In this chapter, after mounting an open access fiber-based microcavity and controlling various aspects of the assembled setup, CsPbBr₃ NCs and TEA₂SnI₄ microcrystals were deposited inside the cavity, and the cavity modes coupling with the NCs emission was studied at room temperature. Additionally, the spectral characteristics of the FP cavity were numerically simulated in order to accurately understand the potential light-mode coupling between Bloch waves in the DBRs and weakly confined modes of the microcavity outside of its stop band, which we observed experimentally. Here it is necessary to note that, a Bloch wave (also known as a Bloch state or Bloch wavefunction), named after Swiss physicist Felix Bloch [195], is a type of wave function for a particle in a periodically repeating environment, such as electrons moving through a semiconductor such as silicon (whose atoms form a crystal lattice). A Bloch wave description also applies to any wave-like phenomena in a periodic medium, such as photonic crystals or DBRs with a periodically repeating refractive index of these multilayer structures.

5.2 Experimental Details and Methods

Synthesis of CsPbBr₃ PNCs:

This is presented in Chapter 3.2, in the part of Synthesis of Colloidal Solution (OLA/OA ligands).

TEA₂SnI₄ micro crystals:

In a 3 neck round bottom flask, 20 mL of mesitylene and 1 mL of oleic acid were degassed at room temperature for 1 hour in vacuum, Subsequently, a SnI₂-trioctylphosphine solution was injected to the reaction flask under nitrogen atmosphere and the temperature was raised to 160 °C. Finally, 0.11 mL of 2-thiopheneethylamine (TEA) were injected and after 5 seconds, the reaction mixture was cooled down in an ice bath until room temperature. TEA₂SnI₄ microplates were isolated by centrifugation and washed with n-hexane three times. TEA₂SnI₄ microplates were re- dispersed in 3 mL of n-octane and storage in a glovebox.

Preparation of samples for open access microcavity (CsPbBr₃ NCs & TEA₂SnI₄ micro crystals):

The purpose of this research is to couple the PL emission of perovskite materials to cavity modes. In order to achieve this goal, we deposit CsPbBr₃ NCs and TEA₂SnI₄ micro crystals at optimized concentrations on top of the planar DBR forming one of the cavity mirrors, resulting in a uniform monolayer of NCs/microcrystals. The planar DBR is cleaned with ethanol, isopropanol, and acetone before depositing materials. Then, using a spin coating method at 3000 rpm for 60 seconds, perovskite materials with an optimized low concentration were deposited on top of the planar DBR mirror (The concentration of the original solution was 100 mg/mL, and to prepare the samples, 0.1 mg/mL has been used).

5.3 Light-Matter interaction

A critical aspect for developing brighter single-photon sources is manipulating the SE rate. The improved SE criteria in Fabry-Perot microcavities can be achieved by placing photon emitters in an environment that increases the local photonic density of states (LDOS) via the Purcell effect. The modification of the SE in CsPbBr₃ perovskite NCs produced by coupling to Fabry-Perot cavities will be discussed in this section.

The two-dimensional, monolithic, semiconductor microcavities are one of the highest quality factor and most extensively used microcavities for conducting studies such as 2D exciton-polaritonics [68], weak coupling regimens [196], enhancing single photon emission rates [197], and the degree of photon indistinguishability [198], among others. However, in recent years, open-access, fiber based microcavity designs [197] have been shown excellent performances with extremely high collecting efficiencies, high brightness degree and high probability of photon emission into the cavity mode [196, 197]. In these microcavities, one of the DBR mirrors is replaced by a concave dielectric DBR mirror patterned in the optical fiber. The hemispherical (or near hemispherical) geometry of the replaced DBR (see Figure 5.1.a) provides a strong optical confinement of the cavity modes in lateral dimension, and the open style of the fiber cavity allows for independent movement of the fiber mirror (details was presented in chapter 2.2.4).

To test the cavity modes in such an open cavity, we can illuminate the cavity with a white light source (halogen lamp) and measure the transmitted light in the cavity. Cavity resonance condition is fulfilled when $\lambda = 2L/m$, where L is the cavity length and m is the confined mode order. As a result, moving the fiber farther or closer to the flat DBR changes the length of the cavity, L , and changes the wavelength λ of the confined mode, as observed

in Figure 5.1.b. For example, if we reduce the cavity length, L (put the fiber closer to the flat DBR), the mode wavelength will shorten as well, causing the mode transmission peak to shift to higher energies. Figure 5.1.b also shows how the mode intensity decreases as the cavity length is decreased. This intensity drop could be caused by a variety of factors: the reflection coefficients along the stopband can not be constant, the white light source (halogen lamp) has a non-uniform spectrum or a possible relative inclination of the fiber and the flat mirror. Importantly, the capability to shift cavity modes allows us to distinguish them from other signals.

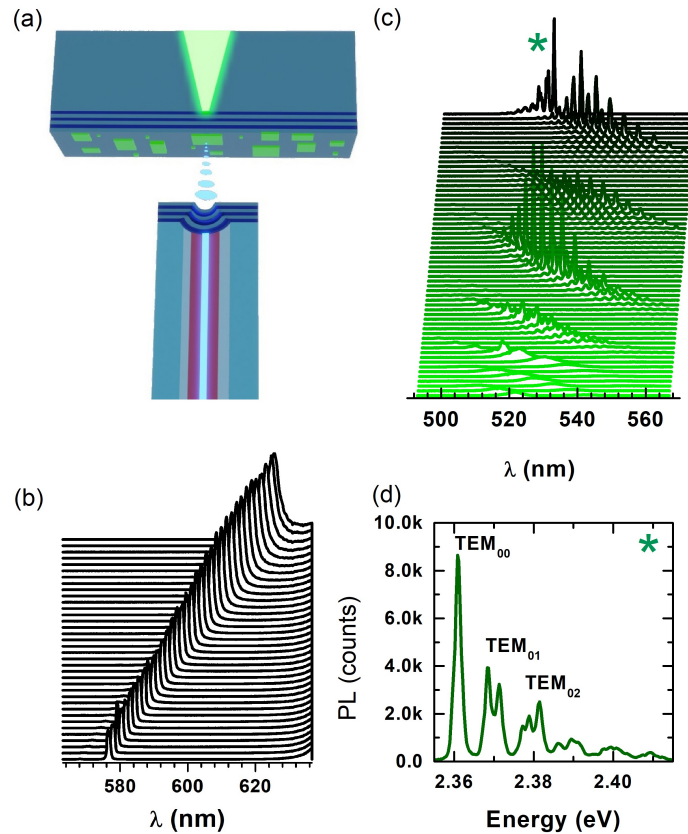


Figure 5.1: (a) A schematic of an open-access, fiber-based microcavity, (b) the cavity transmission spectra with varying cavity lengths, (c) PL emission of CsPbBr₃ NCs at room temperature that interacted with cavity modes at various cavity lengths, (d) interacted PL emission of CsPbBr₃ NCs with cavity modes. (illustrated by * in (c)).

Weak coupling between cavity modes and CsPbBr₃ perovskite nanocrystals:

To investigate how NCs' PL emission interacts with a cavity mode, after depositing the CsPbBr₃ NCs on planar DBR, the fiber is moved close to the flat DBR mirror until the cavity length is small enough to generate confined modes. If the cavity modes were coupled to the NCs' PL emission, the PL would rise dramatically. For long L , we find very weak modes (see Figure 5.1.c), and will not result in a significant emissions enhancement. As L decreases, more intense modes with larger PL enhancement are observed (see Figure 5.1.c). In Figure 5.1.d, a PL spectrum from Figure 5.1.c (marked by *) was selected to show the fundamental transverse EM mode (TEM₀₀), and additional peaks corresponding to groups of higher-order TEM modes: (TEM₀₁), (TEM₀₂), etc. Therefore, the PL emission of Perovskite NCs is modified after the coupling with the cavity modes. Figure 5.2.a depicts the PL emission of CsPbBr₃ NCs inside the cavity after being pumped with a blue laser ($\lambda=450$ nm). The black and grey spectra represent the PL emission before and after cavity mode coupling to the NCs' emission, respectively.

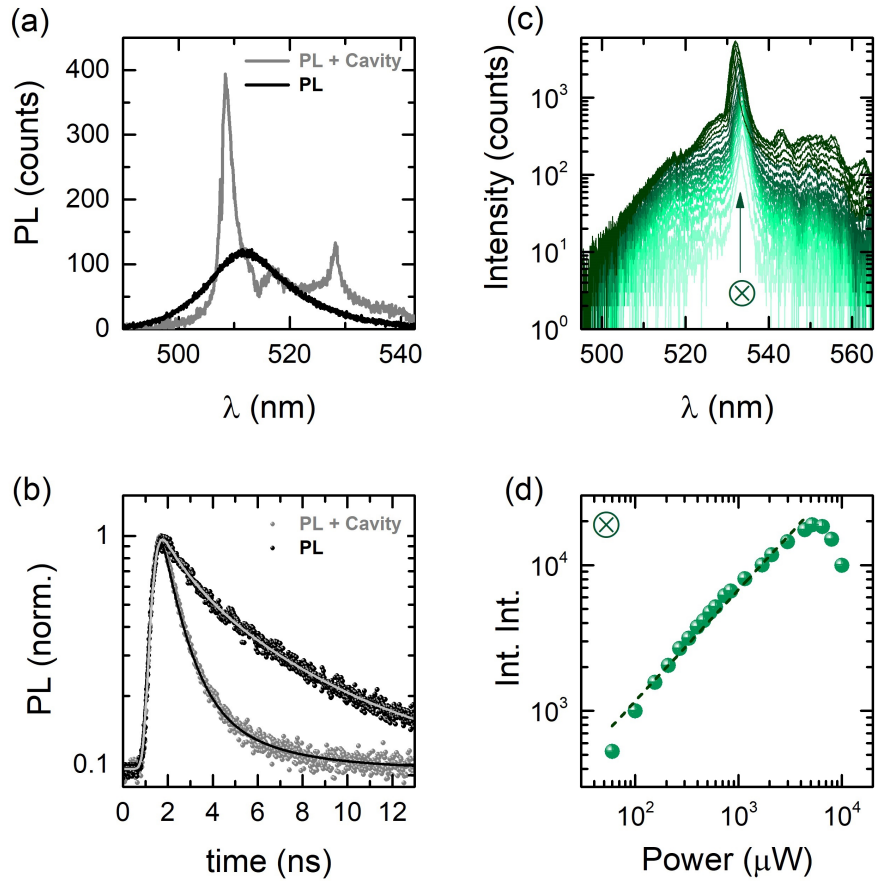


Figure 5.2: (a) PL emission of CsPbBr₃ NCs at room temperature without and with cavity mode coupling, (b) time resolved PL of CsPbBr₃ NCs corresponding to (a) at room temperature. (c) color-coded power-dependent PL emission of CsPbBr₃ NCs coupled to the cavity modes by increasing excitation power from 60 μ W (faded green), to 10 mW (dark green), (d) integrated PL intensity over the spectral emission range of the coupled PL, with slope $m=0.81\pm 0.02$ in a log-log plot.

Figure 5.2.b shows TRPL spectra that correspond to the PL spectra in Figure 5.2.a. The black spectrum depicts the TRPL of CsPbBr₃ NCs at room temperature without coupling to the cavity modes with $\tau_1=1.70$ ns, $\tau_2=6.13$ ns. The grey spectrum represents the TRPL of coupled NCs with $\tau_1=0.57$ ns, $\tau_2=2.35$ ns. We can clearly see a life time shortening as a result of PL emission and cavity mode weak coupling, which results in a Purcell factor enhancement around ~ 3 . Figure 5.2.c represents the excitation

power dependency of couple PL spectra of CsPbBr₃ NCs, where spectra are shown as the excitation power increases from 60 μ W (light green) to 10 mW (dark green). The dependence of the integrated PL intensity on excitation power for the peaks in Figure 5.2.c is shown in a log-log plot in Figure 5.2.d. A fit to the observed variation reveal a slope $m = 0.81 \pm 0.02$. The less than unity slope for this band implies that as excitation power increases, the PL quantum yield decreases. Saturation is observed at high powers, suggesting that the NCs are not lasing under these conditions. Additionally, in Figure 5.2.c it can be seen that at high power there is a slightly blue shift for the spectrum, which probably it is due to the heating of the sample. It is important to note that when depositing the NCs on the planar DBR by spin coating (details in chapter 2), the concentration of the colloidal solution and velocity of the spinner were optimized in order to obtain a more or less uniform mono layer of the NCs on to the planar DBR. Because of the thin film's low thinness, the possibility of observing amplifying spontaneous emission and lasing is reduced. To produce spontaneous amplifying emission due to the coupling of the emission with a cavity mode we need to work with maximum excitation power. The thickness of the deposited material inside the cavity is low (monolayer of NCs) and we are working in the ambient condition. As a result, by going to the higher powers the thin layer of material might be easily damaged. Also, if we deposit a thicker sample inside the cavity, one issue is that as the material thickness increases, the cavity cannot reach the same position; we are in different fundamental mode orders, and hence, the free spectral range (FSR) will be reduced as a consequence of the increased cavity length. This will produce a shorter separation between fundamental mode orders, which can be an important issue when trying to couple the perovskite broad emission to a single cavity

mode.

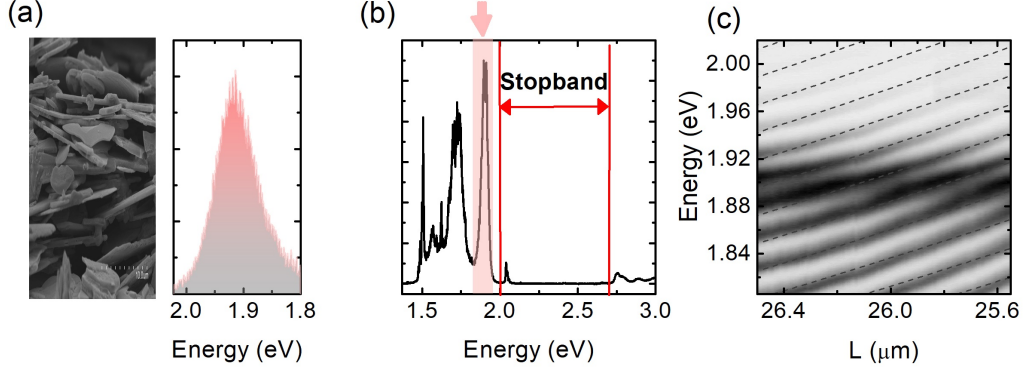


Figure 5.3: (a) SEM image (left panel) and PL spectrum (right panel) of TEA₂SnI₄ microcrystals. (b) Transmission spectrum of the empty cavity with indication of the stopband and the position of the PL emission, which is outside of the stopband (red shadow and arrow). (c) Energy evolution of cavity modes as a function of the cavity length (L).

Figure 5.3 illustrates the coupling of microcavity modes with the emission of TEA₂SnI₄ perovskite microcrystals. The lateral size of the isolated microcrystals is in the order of several micrometers, and their thickness in the range of 200-300 nm, because these are made from many 2D layers as shown in left panel of Figure 5.3.a. The PL spectrum of the TEA₂SnI₄ microcrystals is peaked at ~ 1.91 eV, as shown in the right panel of Figure 5.3.a. The stopband of the fiber-based microcavity, is deduced from Figure 5.3.b where the experimentally measured transmission spectrum using a white light source is plotted. Clearly, the PL emission of TEA₂SnI₄ microcrystals is outside of the stopband. Figure 5.3.c depicts the coupling observed between weakly confined modes of the cavity outside the stopband and the PL emission of the perovskite for relatively large cavity lengths (~ 25 - 26 μm). The movement of the cavity modes without any avoided crossing is characteristic of a weak coupling regime for such large cavity length situation.

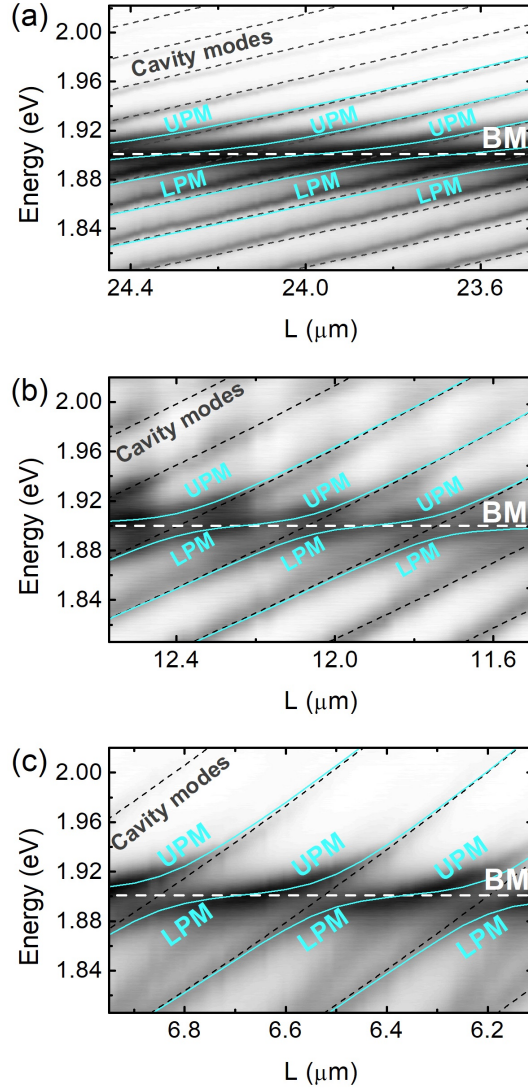


Figure 5.4: The energy evolution of cavity modes as a function of cavity length (L) represents (a-b-c) strong coupling in various cavity length ranges, resulting in 8-10-15 meV vacuum Rabi splitting.

However, by reducing the cavity length clearly an avoided crossing between two modes is observed. The avoided crossing is a direct feature of strong coupling regime (see Figure 5.4.a,b&c). As a consequence, these graphs represent the energy evolution of cavity modes as a function of cavity length (L) due to the strong coupling between two light modes (see section 5.4).

By decreasing the cavity length, the weakly confined cavity modes move and their peak position energy change. In the smaller cavity lengths, the intensity of modes enhances and as can be seen in Figure 5.4.a,b&c they begin to interact strongly with other DBR modes (details presented in numerical modeling section 5.4). The blue lines in Figure 5.4.a,b&c are plotted using the equation for a two coupled oscillator model representing the upper photonic mode (UPM) and lower photonic mode (LPM):

$$E_{UPM,LPM} = \frac{E_{cav} + E_{BM}}{2} \pm \sqrt{\Omega^2 + \left(\frac{E_{BM} - E_{cav}}{2}\right)^2} \quad (5.1)$$

According to fitted data by using Equation 5.1 in Figure 5.4.a,b&c, which correspond to different cavity length ranges, decreasing the cavity length increases the vacuum Rabi splitting from 8 meV to 10 meV and 15 meV. The PL peak emission of the 2D perovskite (~ 1.91 eV) is represented in these figures by a white dashed line.

5.4 Light-mode coupling

The possible light-mode coupling in the fiber-based open-access microcavity has been numerically investigated in this section using COMSOL multi-physics software. Considering the experimental setup, the basic geometry of the simulated microcavity, is in the form of $(DBR)_{Fiber}d_C(DBR)_{Planar}$, where $(DBR)_{Fiber}$ and $(DBR)_{Planar}$ represent the distributed Bragg reflectors in the fiber tip (bottom DBRs in Figure 5.5) and planar substrate (top DBRs in Figure 5.5), respectively, and d_C defines the cavity length. Planer and fiber DBRs are consisting of 13 and 9 pairs with two different dielectric layers with higher (H) and lower (L) refractive indexes. The constituent layers H and L are Nb_2O_5 and SiO_2 , with $n_H=2.35$ and $n_L=1.49$,

respectively, as higher and lower refractive index materials.

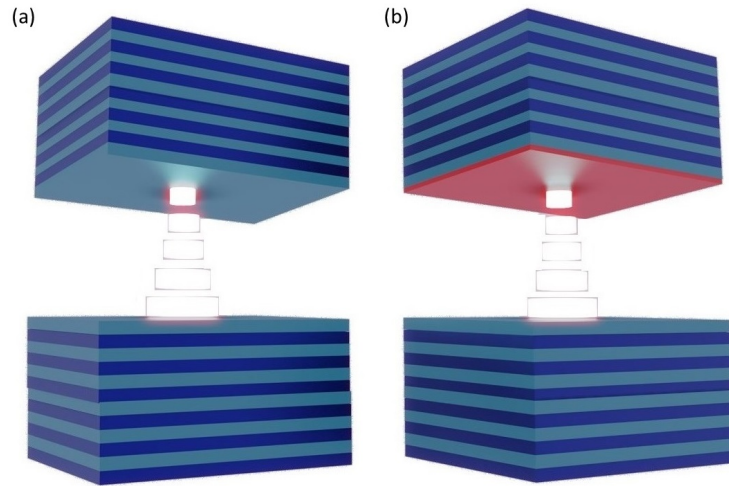


Figure 5.5: Schematic representation of the modeled structure for (a) an empty cavity and (b) a cavity with deposited materials on planar DBR is shown. The top DBRs in both panels are planar, while the bottom DBRs are in the fiber tip and the red layer in panel (b) depicts the deposited active material on the planar DBR.

5.4.1 Bragg photons propagating in the photonic structure

DBRs are examples of one dimensional Photonic Crystals (PCs). In these structures the index of refraction is modulated in one direction by the alternative deposition of layered periodic patterns, which are gaining popularity among researchers. The reflectivities of the fiber and planar DBRs were calculated in Figure 5.6.a,b to show the band gap (grey zone) and allowed frequencies of these DBRs. Figure 5.6.c,d show the electric field intensity distribution for the propagating frequencies of fiber DBR and planar DBR at $E_f=1.92$ eV and $E_p=1.98$ eV, respectively (These modes from fiber DBR with $E_f=1.92$ eV and planer DBR with $E_p=1.98$ eV were chosen since they are in the energy range in which we are interested.). On the other hand, Figure 5.6.e,f, depict the distribution of electric field

intensity in the middle of the photonic band gap ($E_f=E_p=2.35$ eV) for fiber and planar DBRs. The band gap clearly suppresses the electric field and as shown in the Figures 5.6.e,f, the electric field is evanescent inside the structure; however, in the allowed frequencies (outside the band gap) the electric field can propagate inside the DBRs (see Figures 5.6.c,d).

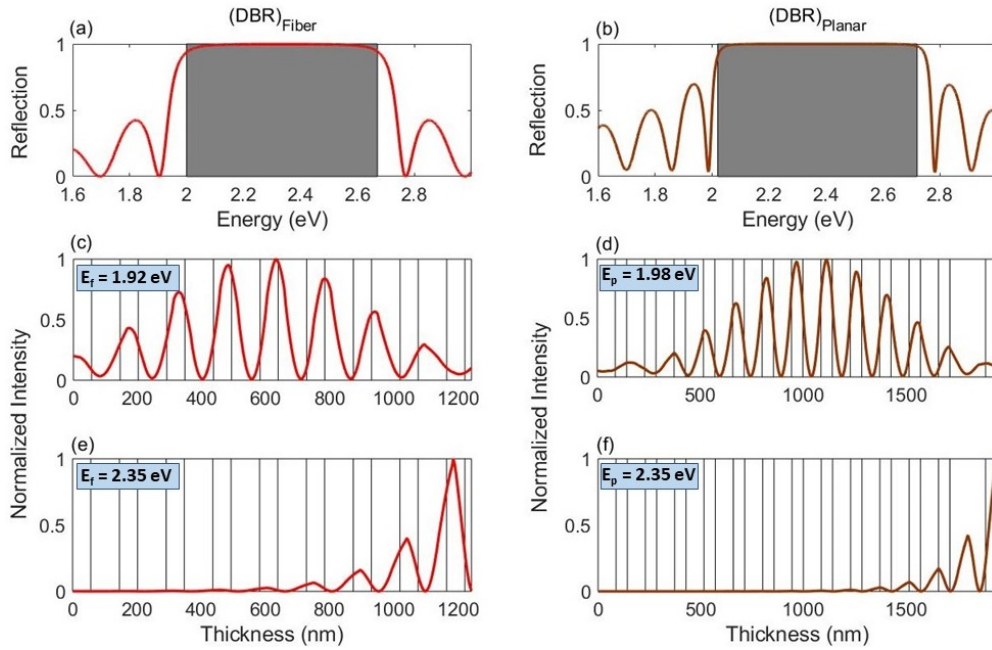


Figure 5.6: The reflection spectra of the (a) fiber DBR and (b) planar DBR as a function of energy, the photonic band gap of DBRs is depicted by the grey zones. (c), (d) Normalized electric field intensity spatial distributions for fiber and planar DBR propagating modes at $E_f=1.92$ eV and $E_p=1.98$ eV, respectively. (e), (f) Normalized electric field intensity spatial distributions in the middle of the band gaps of fiber and planar DBRs.

5.4.2 DBR-based microcavities

As mentioned in previous section (see Figure 5.5), DBRs are made up of layers of alternating refractive index dielectric materials with thickness of $d_i = \lambda_0/4n_i$ ($i=1, 2$), where n_i is the refractive index of the dielectric material i and λ_0 is the wavelength of light in vacuum. By supplying adequate periods of the layers in the DBRs' manufacturing, nearly all of the light

is reflected back into the cavity in the structure's stopband. To achieve good coupling between the emitter and the cavity mode, the first should be deposited inside the microcavity so that it overlaps with an anti-node (maximum) of the cavity field. As a result, the electric field distribution inside the cavity is critical to the design of the microcavity.

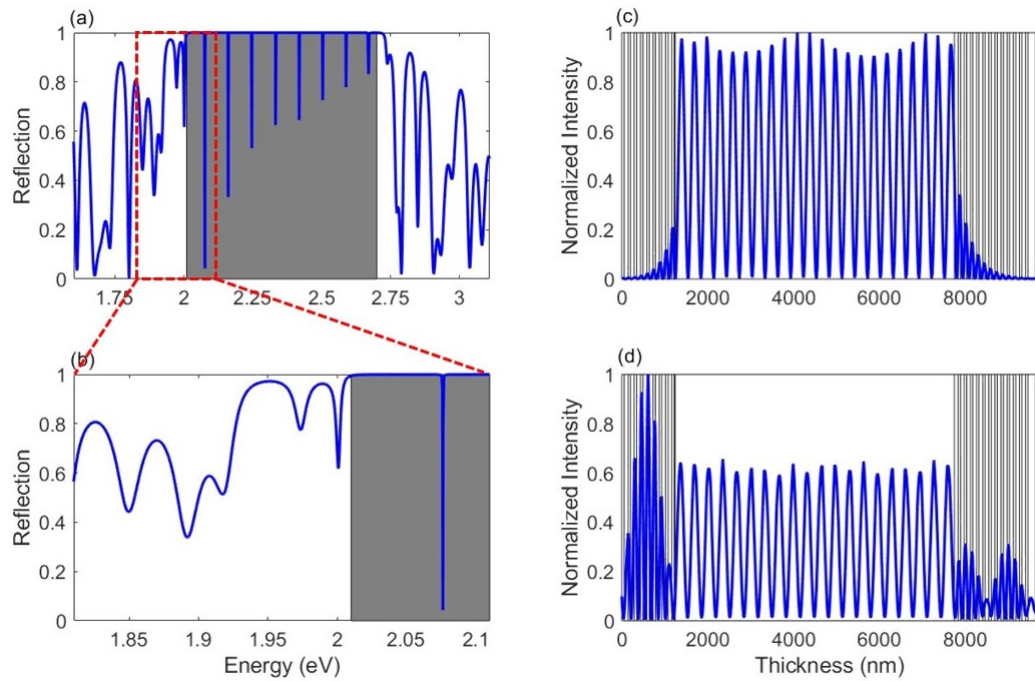


Figure 5.7: The reflection spectra of the (a) DBR based microcavity as a function of energy, (b) zoom of the reflection curve shown in (a), the stop band of the microcavity is depicted by the grey color. (c), (d) Normalized electric field intensity spatial distributions for the strongly confined mode of the microcavity at $E=2.07$ eV and the weakly confined mode outside the stop band at $E=1.89$ eV, respectively.

It is important to emphasize here that the electric field distribution is maximized inside the cavity for cavity modes with very high-quality factors (Q factors) that are strongly confined within the microcavity's stop band (grey area in Figures 5.7.a,b). As shown in Figures 5.7.c, for this type of strongly confined cavity modes, the electric field is maximum inside the cavity and is exponentially attenuated (evanescent) inside the DBRs. However,

there is another type of modes outside of the stop band; unlike highly confined cavity modes with high Q factors, these modes are weakly confined. The electric field distribution for these modes behaved differently. The electric field intensity is not maximized inside the cavity for these modes, nor is it attenuated inside the DBRs; in fact, the electric field can be maximized inside the DBRs (see Figures 5.7.d). This behavior results in interaction between these modes and the DBR modes described in previous section. The DBR modes shown in Figures 5.6.a,b are fixed, but these weakly confined modes move by changing the cavity length, and then occasionally could get into resonance with the fixed DBRs modes. On resonance both modes can be coupled, and if the energy exchange between them is reversible then the strong coupling regimen can be achieved. The strong coupling between these two optical modes can be achieved even with empty cavity, and hence illuminated just with external light. In this sense the emitter here will act as an external light source. However, the role of the optical emitter will include extra effects, as it is going to be shown in the next section.

5.4.3 Interaction of weakly confined cavity modes with propagating Bragg photons

The coupling of DBR modes and weakly confined cavity modes will be investigated in this section. We will compare the coupling in an empty microcavity and in a microcavity with deposited materials (TEA_2SnI_4 micro crystals) to demonstrate the role of emitter in modulating this strong light-mode coupling.

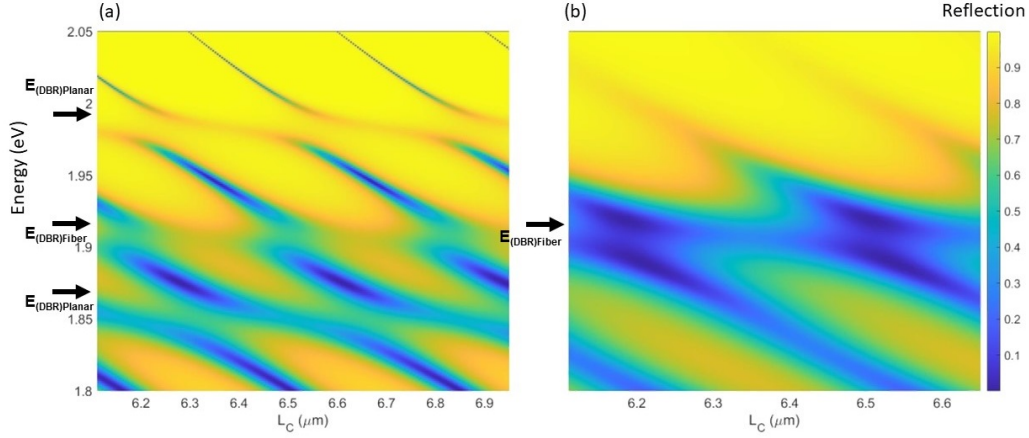


Figure 5.8: The reflection spectra as a function of cavity length for (a) an empty cavity and (b) a cavity with 300 nm thin film of active material on to the planar DBR with PL emission at $E=1.91\text{eV}$.

The reflection spectra of an empty cavity and a cavity with active material are plotted as a function of the cavity length in Figures 5.8.a,b, respectively. In the numerical model the active material is considered as a 300 nm thin layer on top of the planar DBR (see Figures 5.8.b). In the empty cavity (Figure 5.8.a), three avoided crossings can be seen as a result of coupling the weakly confined cavity modes with three different fixed DBR modes. In this specific energy range (from 1.8 eV to 2.05 eV), one of the DBR modes is placed at $E_f=1.92$ eV (see Figure 5.6.a), which corresponds to a DBR optical mode from the fiber DBR (labeled as $(DBR)_{Fiber}$), however the second and third modes are located at $E_p=1.86\text{eV}$ and 1.98eV (see Figure 5.6.b). corresponds to optical modes from planar DBRs (labeled as $(DBR)_{Planar}$). These DBR modes are depicted in Figure 5.8 with black arrows. In contrast to the empty cavity, when the active material is inside the cavity, there is only one avoided crossing at the same energy range but with a larger splitting. To quantify the comparison of the splitting between the empty cavity and the cavity with materials, the Rabi splitting has been extracted from the simulated data, and there is an 8 meV enhancement

in the Rabi splitting from empty cavity ($\Omega = 12meV$) to the cavity with materials ($\Omega = 20meV$). As shown in Figure 5.8.b, the avoided crossing is caused by coupling between weakly confined cavity modes and a DBR mode from $(DBR)_{Fiber}$, and two other avoided crossings are completely erased.

To understand how deposited materials inside the cavity contribute to this behavior, the electric field intensity distribution inside the structure is calculated for both an empty cavity and a cavity with material, as shown in Figures 5.9 and Figure 5.10, respectively.

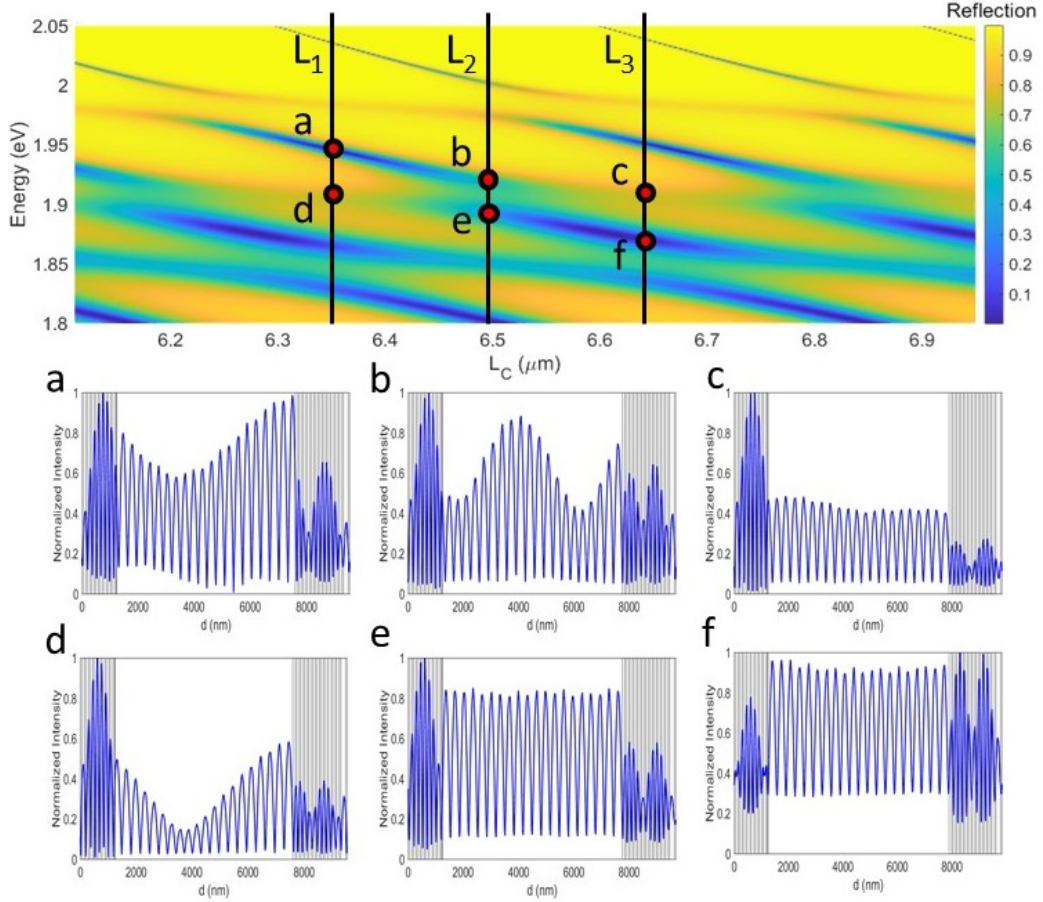


Figure 5.9: Top panel: The reflection spectra as a function of cavity length for an empty cavity. Bottom panels: The distribution of electric field intensity from point a to f on the top panel. These points are selected at three different cavity lengths $L=6.35, 6.5,$ and $6.65 \mu\text{m}$ around the fiber DBR mode, $E_f=1.92 \text{ eV}$, in which the avoided crossing occurring in both empty and filled cavities.

The reflection spectra as a function of cavity length for an empty cavity are shown in the top panel of Figure 5.9, with six points (a-f) selected around the fiber DBR mode energy based on three different cavity lengths $L = 6.35, 6.5, \text{ and } 6.65 \mu\text{m}$. The energy of this mode from the fiber DBR was chosen in both empty and filled cavities because it is the only mode that we observed avoiding crossing in both empty and filled cavities. Figures 5.9.a-f depict the distribution of the electric field intensity corresponding to the points a-f on the top panel of Figures 5.9, respectively. According to these figures, the electric field is maximized in both fiber and planar DBRs, which can interact with DBR modes and results various avoided crossings.

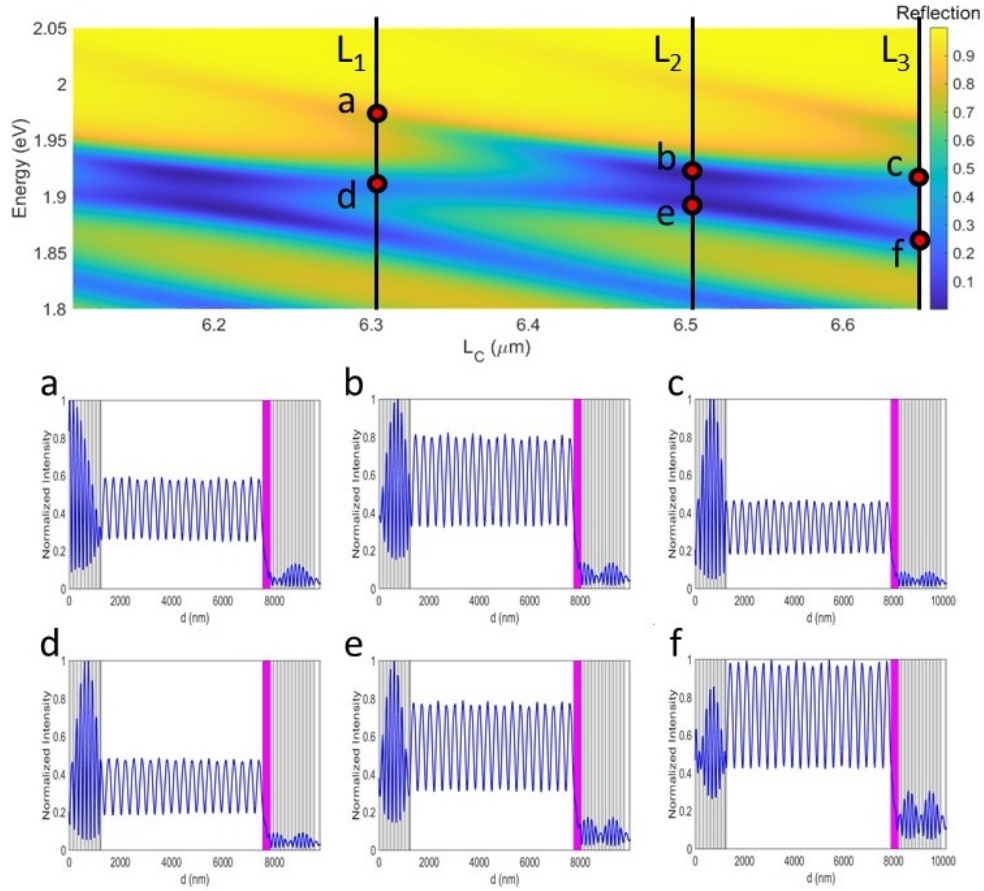


Figure 5.10: Top panel: The reflection spectra as a function of cavity length for a cavity with a 300 nm layer of active material with emission at $E=1.91$ eV. Bottom panels: The distribution of electric field intensity from point a to f on the top panel. These points are selected at three different cavity lengths $L=6.3$, 6.5 , and 6.65 μm around the fiber DBR mode, $E_f=1.92$ eV. the colored layer represents deposited materials on the planar DBR.

Similar to the case of the empty cavity, the reflection spectra as a function of cavity length for a microcavity with 300 nm thin layer on planar DBR are shown in the top panel of Figure 5.10. In this case, as in the previous one, six points (a-f) on the counter plot (top panel in Figures 5.10) are chosen around the fiber DBR mode energy in three different cavity lengths $L=6.3$, 6.5 , 6.65 μm . Figures 5.10.a-f depict the distribution of electric field intensity corresponding to the points a-f on the top panel of Figures 5.10,

respectively. According to these figures, the electric field is dramatically suppressed in the planar DBR after depositing materials inside the cavity, and the electric field is maximized only in the fiber DBR in comparison to the empty cavity. As a result, after depositing the materials inside the cavity, the number of avoided crossings are reduced.

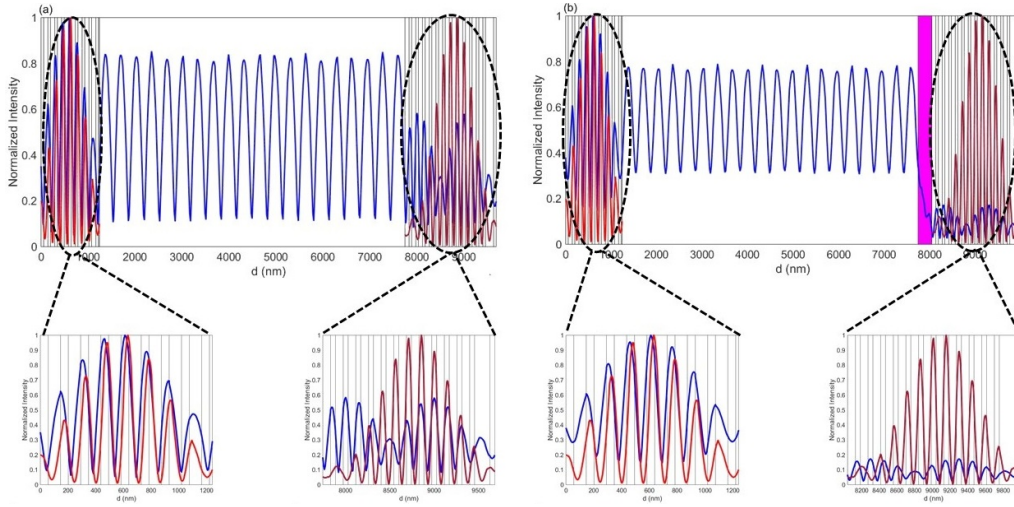


Figure 5.11: Overlapping electric field intensity distributions of the cavity mode and DBR modes in (a) an empty cavity and (b) a cavity with a 300 nm layer deposited inside the cavity.

Finally, the coupling strength of the weakly confined cavity mode with DBR modes is calculated to understand how deposited materials modify mode coupling:

$$m = \int E_{Cavity}^2 \times E_{DBRs}^2 \quad (5.2)$$

Figures 5.11.a,b represent the overlapping electric field intensity distributions of the cavity mode and DBR modes in an empty cavity and a cavity with a 300 nm layer deposited inside the cavity, respectively. We will define m value as a figure of merit, and this figure of merit gives us the overlapping between the field distribution of the DBR and the field distribution of

the cavity. Regarding the electric field in Figures 5.11.a,b, the m value for empty cavity is $m=52$ and $m=37$ for $(DBR)_{Fiber}$ and $(DBR)_{Planar}$, respectively. However, in the filled cavity, these values are $m=480$ and $m=1.85$. Therefore, the coupling strength in the empty cavity in both DBRs is more or less similar; however, after depositing the materials on the planar DBR, the electric field in the planar DBR is suppressed and the m value decreases, while the coupling in the fiber DBR dramatically intensifies.

In terms of the benefits of this coupling, the simulation of polaritons with light is one possible application for this type of light-light mode strong coupling. Polariton is a quasi-particle (half-light, half-matter) generated by a strong coupling between an emitter and a cavity mode. Then, by controlling two light modes, we can evaluate mode couplings, Rabi splitting, and strong coupling. In this sense, the weakly confined modes interact with the mirrors; however, as the resonance approaches, the weakly confined modes are coupled to modes in one of the mirrors but not the other. So there is more transferred light from one of the mirrors because the light is more coupled to that mirror, which can be kind of unidirectional coupling. The other is an optical analog of Rabi splitting, as is Rabi-like interaction, which is two coupled oscillator models [199–201].

5.5 Conclusions

In this chapter, after designing and building an open access fiber-based microcavity and controlling various aspects of the assembled setup, CsPbBr₃ NCs were deposited inside the cavity, and the cavity modes interaction with the NCs emission was studied at room temperature. The cavities' specific geometry provides strong optical confinement of the modes, and its open style allows for independent movement of the fiber mirror, allowing for

in-situ tuning of the cavity resonance without the reduction in coupling. Additionally, the setup was numerically modeled in order to accurately understand the potential Light mode coupling between Bloch waves in the DBRs and weakly confined cavity modes of the microcavity outside of its stop band, which we observed experimentally. The simulation results revealed that Bloch waves in DBRs and weakly confined cavity modes of the microcavity outside of its stop band can be strongly, and the coupling strength can be modified by depositing materials inside the cavity.

Chapter 6

Conclusions

The main goal of this Ph.D. thesis was focused on the incorporation of perovskite materials emitting in the visible wavelengths in photonic and quantum applications, particularly, the implementation of outstanding optical properties of 2D and colloidal LHPs NCs to bring different functionalities, such as single photon light generation, single donor-acceptor discrete optical emission and perovskite polaritons, into various photonics and quantum implementations. The following are the most important results of this Ph.D.:

■ Optical stability of CsPbX₃ (X=Br, I) perovskite nanocrystal for single photon emission

In chapter 3, we used cryogenic micro-PL and micro-TRPL spectroscopy to examine single PNCs with two different capping ligands, and we deduced an average homogeneous linewidth of excitonic optical transitions in freshly prepared samples for both cases. In comparison to the typical OLA/OA ligands with the ~ 2.35 meV linewidths on average, the homogeneous linewidths of the single CsPbBr₃ NCs with ZW ligands exhibit a

significant narrowing with higher stability due to drastically decreased spectral diffusion and blinking effects. The mean value of PL linewidth for NCs with the ZW ligands with the average value of $\sim 250 \mu\text{eV}$, and the lowest value of $\sim 125 \mu\text{eV}$ being the narrowest value reported so far in the literature for CsPbBr₃ NCs. Furthermore, based on micro TRPL measurements, a slightly longer (factor ~ 1.35) decay time was observed for CsPbBr₃ single NCs with ZW ligands, making them better for quantum light sources, as demonstrated by $g^2(0) \sim 0.5$. However, in the case of single CsPbI₃ NCs, this strategy (using ZW ligands instead of OLA/OA) did not work, and the traditional OLA/OA ligands were still the best candidate. For CsPbI₃ NCs with the average size of $\sim 250 \mu\text{eV}$ and the lowest value of $\sim 140 \mu\text{eV}$ for μ -PL linewidth, we obtained a $g^2(0) \sim 0.3$ second order photon correlation function, which is better than $g^2(0) \sim 0.5$ from CsPbBr₃ single NCs with ZW ligands.

■ Donor-acceptor discrete optical emission in 2D perovskites

In chapter 4, observation of the narrow and discrete PL lines associated to DAP transitions is added to recent reported properties, such as exciton binding energy tunability by donor acceptor interactions [64] and DAP single photon emission performance in 2D hBN [184]. By means of XPS spectroscopy, we showed that the two organic components present in the n=2 sample promote the formation of the defects responsible of the DAP transition. In detail, the coexistence of MA^+ cation, giving rise to Pb segregation, and PEA_2 cation, causing the inorganic lattice sheet distortion, might favour the displacement and exchange of MA^+ and Pb atoms, hence the formation of MA_{Pb} acceptor and Pb_{MA} donor states. The model predicts the presence of low density DAP states in the spectral range close to the $X_{2,3}$ emission, and hence both low DOS and large donor acceptor

wavefunction separation explain the measured DAP narrow optical transitions with nanosecond lifetimes. To provide a future application based on the control of these states, specific sample preparation routes should be designed to control and optimize the DAP state population, localization, or isolation.

■ **Light-Matter interaction and Light mode coupling in an open-access fiber-based optical microcavity**

In chapter 5, an open-access, fiber-based microcavity has been used to study weak and strong coupling regimens. After mounting an open access fiber-based microcavity, CsPbBr₃ NCs were deposited inside the cavity, and the cavity modes interaction with the NCs emission was studied at room temperature. The cavities' specific geometry provides strong optical confinement of the modes, and its open style allows for independent movement of the fiber mirror, allowing for in-situ tuning of the cavity resonance. Additionally, the setup was numerically modeled in order to accurately understand the potential light-mode coupling between Bloch waves in the DBRs and weakly confined modes of the microcavity outside of its stop band, which we observed experimentally during the experiments. The simulation results revealed that Bloch waves in DBRs and weakly confined modes of the microcavity outside of its stop band can be strongly coupled even in the empty cavity, and the coupling strength can be modified by depositing materials inside the cavity.

Overall, we believe perovskite materials are promising candidates for future photonics and quantum applications. LHPs have a PLQY of approximately 100%, making them an excellent contender for single-photon sources. Furthermore, work on 2D perovskites shows that the research on DAP in 2D materials represents a growing field with high potential, and observation

of the narrow and discrete PL lines associated to DAP transitions is added to recent reported properties of DAP in 2D materials. Furthermore, revealing the light-mode coupling simultaneously with the light matter coupling in an open access microcavity is very beneficial for the future development of coupled complex microcavities for quantum photonic applications based on the combination and Light-Matter interaction and light mode strong coupling, such as qubit initializers or quantum sensing systems in the field of acousto-optics and optomechanics.

Appendices

A. List of acronyms

■ 2D:	Two-Dimensional
■ APD:	Avalanche photodiode
■ BBO:	Barium borate (nonlinear crystal)
■ CCD:	Charged-coupled device
■ CW:	Continuous Wave
■ DAP:	Donor-Acceptor pair
■ DBRs:	Distributed Bragg reflectors
■ DDAB:	Didodecyl dimethylammonium bromide
■ DOS:	Density of states
■ FA:	Formamidinium
■ FP:	Fabry-Perot
■ FSR:	Free spectral range
■ FWHM:	Full Width at Half Maximum
■ hBN:	Hexagonal boron nitride
■ HBT:	Hanbury-Brown and Twiss
■ HP:	Halide Perovskite
■ LARP:	Ligand assisted reprecipitation
■ LDOS:	Local photon density of states

■ LHP:	Lead Halide Perovskite
■ LT, RT:	Low, Room Temperature
■ MA:	Methylammonium
■ MLs:	Mono-layers
■ μ -PL:	Micro-photoluminescence
■ μ -TRPL:	Micro-Time Resolved photoluminescence
■ NA:	Numerical Aperture
■ NCs:	Nanocrystals
■ Nd:YAG:	Neodymium-doped Yttrium Aluminum Garnet
■ NPs:	Nanoparticles
■ OA:	Oleic Acid
■ OC:	Organic cation
■ OLA:	Oleylamine
■ PCs:	Photonic crystals
■ PDMS:	Polydimethylsiloxane
■ PEA:	Phenethylammonium
■ PF:	Purcell Factor
■ PL:	Photoluminescence
■ PLQY:	Photoluminescence Quantum Yield

■ PMMA:	Polymethylmethacrylate
■ PNCs:	Perovskite nanocrystals
■ QDs:	Quantum Dots
■ QE:	Quantum Emitter
■ Q-factor:	Quality Factor
■ QY:	Quantum Yield
■ RoC:	Radius of Curvature
■ SE:	Spontaneous emission
■ Si, SiO₂:	Silicon, Silicon Oxide
■ SM:	Single mode
■ TCSPC:	Time correlated single photon counting
■ TE:	Trapped excitons
■ TEM:	Transmission Electron Microscopy
■ TLS:	Two-Level Systems
■ TRPL:	Time Resolved Photoluminescence
■ UHV:	Ultra-high vacuum
■ UV:	Ultraviolet
■ vdW:	Van der Waals
■ WGM:	Whispering-gallery-mode

- XPS: X-ray photoelectron spectroscopy
- ZDT: Zero delay time
- ZW: Zwitterionic

B. Publications

B.1. Included in the thesis

B.1.1 Papers published in Journals

- **Setatira Gorji**; Marie Krečmarová; Alejandro Molina; Maria C Asensio; Andrés F Gualdrón Reyes; Jesus Rodriguez Romero; Hamid Pashaei Adl; Rodolfo Canet Albiach; Luca Schio; Massimo Tormen; Luca Floreano; Iván Mora Seró; Juan P Martínez Pastor; Juan F Sánchez Royo; Guillermo Muñoz Matutano. "Donor-acceptor discrete optical emission in 2D perovskites". (<https://doi.org/10.48550/arXiv.2204.06400>) (Submitted).
- **Setatira Gorji**; and et al. "Optical stability of CsPbX₃ (X=Br, I) perovskite nanocrystal for single photon emission". (Under preparation).
- **Setatira Gorji**; and et al. "Light-Matter interaction and Light mode coupling in an open-access fiber based optical microcavity". (Under preparation).

B.1.2 Conferences (posters)

- **Setatira Gorji**; and et al. "Light-Light coupling for optomechanics quantum sensing" (Flash talks ICMUV Conference). July (2023), Valencia, Spain.
- **Setatira Gorji**; and et al. "Quantum light emission from CsPbX₃ (X=Br, I) perovskite nanocrystals with high optical stability" (Quantum Nanophotonics). March (2023), Benasque, Spain.

- **Setatira Gorji;** and et al. "Optical stability of CsPbX₃ (Br, I) perovskite nanocrystal for single photon emission" Sustainable Metal-halide perovskites for photovoltaics, optoelectronics, and photonics Conference (Sus-MHP). December (2022), Valencia Spain.
- **Setatira Gorji;** and et al. "Strong coupling between TEA₂SnI₄ perovskite emission and open access fiber cavities at room temperature", Proceedings of International Conference on Emerging Light Emitting Materials (EMLEM22). October (2022), Limassol, Cyprus. (<https://doi.org/10.29363/nanoge.emlem.2022.053>)
- **Setatira Gorji;** and et al, "Donor-acceptor discrete optical emission in 2D perovskites", Proceedings of International Conference on Emerging Light Emitting Materials (EMLEM22). October (2022), Limassol, Cyprus
- **Setatira Gorji;** and et al, "Tunable fiber based open cavities for exciton polaritons with single nanocubes and 2D perovskites ". Quantum nanophotonics conference, March (2021), online poster.
- **Setatira Gorji;** and et al, "Tunable fiber based open cavities for exciton polaritons with perovskites materials" ICMUV Youth Conference, June (2021).Spain.

B.2 Not included in the thesis

- Waqas Zia; Clara A. Aranda; Jan Pospisil; Alexander Kovalenko; Monika Rai; Cristina Momblona; **Setatira Gorji;** Guillermo Muñoz Matutano; Michael Saliba. "Impact of Low-Temperature Seed-Assisted Growth on the Structural and Optoelectronic Properties of MAPbBr₃

Single Crystals”. *Chemistry of Materials*. (2023). (<https://doi.org/10.1021/acs.chemmater.3c00780>)

- Hamid Pashaei Adl; **Setatira Gorji**; Guillermo Muñoz Matutano; Andres F Gualdrón Reyes; Isaac Suarez; Vladimir S Chirvony; Ivan Mora Sero; Juan P. Martínez Pastor. ”Superradiance Emission and Its Thermal Decoherence in Lead Halide Perovskites Superlattices”. *Advanced Optical Materials*. 2202497. (2023). (<https://doi.org/10.1002/adom.202202497>)
- Hamid Pashaei Adl; **Setatira Gorji**; Andres F Gualdrón Reyes; Ivan Mora Sero; Isaac Suarez; Juan P. Martínez Pastor. ”Enhanced Spontaneous Emission of CsPbI₃ Perovskite Nanocrystals Using a Hyperbolic Metamaterial Modified by Dielectric Nanoantenna”. *Nanomaterials*. 13 - 1, pp. 11. Multidisciplinary Digital Publishing Institute, (2023). (<https://doi.org/10.3390/nano13010011>)
- Rodolfo Canet Albiach; Marie Krečmarová; Jose Bosch Bailach; Andrés F Gualdrón Reyes; Jesus Rodríguez Romero; **Setatira Gorji**; Hamid Pashaei Adl; Iván Mora Seró; Juan P Martínez Pastor; Juan F Sánchez Royo; Guillermo Muñoz Matutano. ”Revealing giant exciton fine-structure splitting in 2D perovskites using van der Waals passivation”. *Nano Letters*. 22 - 18, pp. 7621 - 7627. American Chemical Society, (2022). (<https://doi.org/10.1021/acs.nanolett.2c02729>)
- Hamid Pashaei Adl, **Setatira Gorji**, Guillermo Muñoz-Matutano, Ivan Sanchez Alarcon, Rafael Abargues, Andres F. Gualdrón-Reyes, Ivan Mora-Sero, Juan P. Martínez-Pastor, ”Homogeneous and inhomogeneous broadening in single perovskite nanocrystals investigated by micro-photoluminescence”, *journal of luminescence*, (2021).

<https://doi.org/10.1016/j.jlumin.2021.118453>

- Krečmarová, Marie; Canet-Albiach, Rodolfo; Hamid Pashaei Adl; **Gorji, Setatira**; Muñoz-Matutano, Guillermo; Nesládek, Miloš; Martínez-Pastor, Juan P.; Sanchez-Royo, Juan, "Extrinsic Effects on the Optical Properties of Surface Colour Defects generated in Hexagonal Boron Nitride Nanosheets", ACS Applied Materials & Interfaces, (2021). <https://doi.org/10.1021/acsami.1c11060>
- Hamid Pashaei Adl, **Gorji, S.**, Habil, M. K., Suarez, I., Chirvony, V. S., Gualdrón Reyes, A. F., I. Mora-Sero, L. M Valencia, M. de la Mata, J. Hernandez-Saz, S. I Molina, C. J Zapata-Rodriguez, Martínez Pastor, J. P. "Purcell Enhancement and Wavelength Shift of Emitted Light by CsPbI₃ Perovskite Nanocrystals Coupled to Hyperbolic Metamaterials". ACS photonics, 7(11), 3152-3160, (2020). <https://doi.org/10.1021/acsp Photonics.0c01219>
- Hamid Pashaei Adl; **Setatira Gorji**; Guillermo Muñoz Matutano. "Tailoring the spontaneous emission of Nanocube perovskites". Elsevier. (Book chapter) (Accepted).

B.1.2 Conferences (posters)

- Adl HP, **Gorji S**, and et al. "The thermal decoherence of superradiance in halide perovskite supercrystals", Proceedings of International Conference on Emerging Light Emitting Materials (EMLEM22). (2022), Limassol, Cyprus. <https://doi.org/10.29363/nanoge.emlem.2022.044>
- Rodolfo Canet-Albiach, Marie Krecmarova, José Bosch Bailach, Andrés

F Gualdrón-Reyes, Jesús Rodríguez-Romero, **Setatira Gorji**, and et al. "Revealing Giant Exciton Fine-Structure Splitting in 2D Perovskites using van der Waals Passivation", Proceedings of International Conference on Emerging Light Emitting Materials (EMLEM22). (2022), Limassol, Cyprus.

- Raúl Ivan Sánchez-Alarcón, Omar Eduardo Solís-Luna, Cristina Momblona, Teresa S Ripollés, Rafael Abargues, Pablo P Boix, **Setatira Gorji**, and et al. "Bottom-up synthesis of orange-red emitting two dimensional 2-thiophene ethyl ammonium tin (II) halide perovskite microcrystals", Proceedings of International Conference on Emerging Light Emitting Materials (EMLEM22). (2022), Limassol, Cyprus. (<https://doi.org/10.29363/nanoge.emlem.2022.050>)
- Hamid Pashaei Adl, **Setatira Gorji**, and et al, "Manipulating spontaneous emission of the CsPbI₃ Perovskite NCs using hybrid (HMM-Mie resonator) structures", Proceedings of Applied Light-Matter Interactions in Perovskite Semiconductors 2021 (ALMIPS2021), Online, Spain, October 5th - 7th, (2021).
- Martinez-Pastor JP, Adl HP, **Gorji S**, and et al. "Lead halide perovskite nanocrystals: optical properties and nanophotonics. In Low-Dimensional Materials and Devices (2021)" Aug 1 (Vol. 11800, p. 1180013). International Society for Optics and Photonics. (<https://doi.org/10.1117/12.2595442>)
- Hamid Pashaei Adl, **Setatira Gorji**, and et al, "Purcell enhancement and photoluminescence spectra shift of the APbI₃ (A=Cs, FA) Perovskite nanocrystals coupled to Hyperbolic Metamaterials", META 2021, the 11th International Conference on Metamaterials, Photonic

Crystals and Plasmonics, University of Warsaw, Warsaw, Poland, 20-23 July, (2021).

- Hamid Pashaei Adl, **Setatira Gorji**, and et al, "Manipulating the exciton radiative recombination rate of the CsPbI₃ Perovskite nanocrystals using Hyperbolic Metamaterials", online OPTOEL 2021, 30 June-2nd July, (2021)
- Hamid Pashaei Adl, **Setatira Gorji**, "Manipulating the exciton radiative recombination rate of the organic-inorganic APbI₃ (A= FA, Cs) Perovskite nanocrystals using Hyperbolic Metamaterials "ICMUV Youth Conference, June (2021). Spain.
- Marie Krecmarova, Rodolfo Canet-Albiach, Hamid Pashaei Adl, **Setatira Gorji**, and et al, "Temperature dependent emission properties of mechanically exfoliated layered lead halide perovskites", nanoGe Online Meetup, October, (2020).
- Hamid Pashaei Adl, **Setatira Gorji**, and et al, "Spontaneous emission enhancement of organic inorganic FAPbI₃ Perovskite Nano Crystals by using Hyperbolic Metamaterials", nanoGe Online Meetup Conferences Shape Controlled Nanocrystals: Synthesis, Characterization Methods and Applications (ShapeNC), May 7, (2020).
- Hamid Pashaei Adl, **Setatira Gorji**, and et al, "Purcell Enhancement of the Spontaneous Emission of CsPbI₃ Perovskite Nano Crystals by using Hyperbolic Metamaterials", Research Network Perovskites for solar energy conversion and optoelectronics meeting, Seville, Spain, 26th February, (2020).

-
- Hamid Pashaei Adl, **Setatira Gorji**, and et al, “Temperature Sensitive Enhancement of Spontaneous Emission of CsPbI₃ Perovskite Nano Crystals by Hyperbolic Metamaterials”, Optoel, Zaragoza, Spain. 03 - 05 July (2019).

Chapter 7

Bibliography

- [1] Hyojin Park, Chihyeon Ha, and Ju-Hyuck Lee. Advances in piezoelectric halide perovskites for energy harvesting applications. *Journal of Materials Chemistry A*, 8(46):24353–24367, 2020.
- [2] Emilio J Juarez-Perez, Rafael S Sanchez, Laura Badia, Germá Garcia-Belmonte, Yong Soo Kang, Ivan Mora-Sero, and Juan Bisquert. Photoinduced giant dielectric constant in lead halide perovskite solar cells. *The journal of physical chemistry letters*, 5(13):2390–2394, 2014.
- [3] Jialiang Xu, Xinyue Li, Jianbo Xiong, Chunqing Yuan, Sergey Semin, Theo Rasing, and Xian-He Bu. Halide perovskites for nonlinear optics. *Advanced Materials*, 32(3):1806736, 2020.
- [4] J David Zook and Thomas N Casselman. Electro-optic and electroreflectance effects in perovskite-type crystals. *Surface Science*, 37:244–250, 1973.
- [5] Letian Dou, Yang Yang, Jingbi You, Ziruo Hong, Wei-Hsuan Chang, Gang Li, and Yang Yang. Solution-processed hybrid perovskite pho-

-
- photodetectors with high detectivity. *Nature communications*, 5(1):5404, 2014.
- [6] Zhenqian Yang, Yuhao Deng, Xiaowei Zhang, Suo Wang, Huazhou Chen, Sui Yang, Jacob Khurgin, Nicholas X Fang, Xiang Zhang, and Renmin Ma. High-performance single-crystalline perovskite thin-film photodetector. *Advanced Materials*, 30(8):1704333, 2018.
- [7] Hyeon Kim, Lianfeng Zhao, Jared S Price, Alex J Grede, Kwangdong Roh, Alyssa N Brigeman, Mike Lopez, Barry P Rand, and Noel C Giebink. Hybrid perovskite light emitting diodes under intense electrical excitation. *Nature communications*, 9(1):4893, 2018.
- [8] Sudhir Kumar, Jakub Jagielski, Nikolaos Kallikounis, Young-Hoon Kim, Christoph Wolf, Florian Jenny, Tian Tian, Corinne J Hofer, Yu-Cheng Chiu, Wendelin J Stark, et al. Ultrapure green light-emitting diodes using two-dimensional formamidinium perovskites: achieving recommendation 2020 color coordinates. *Nano letters*, 17(9):5277–5284, 2017.
- [9] Alexander EK Kaplan, Chantalle J Krajewska, Andrew H Proppe, Weiwei Sun, Tara Sverko, David B Berkinsky, Hendrik Utzat, and Mouni G Bawendi. Hong–ou–mandel interference in colloidal cspbbr₃ perovskite nanocrystals. *Nature Photonics*, pages 1–6, 2023.
- [10] Sankaramangalam Balachandran Bhagyalakshmi, Dong Zhang, and Vasudevanpillai Biju. Electroluminescence of halide perovskite single crystals showing stochastically active multiple emitting centers. *The Journal of Physical Chemistry C*, 126(42):17826–17835, 2022.

- [11] Quinten A Akkerman. Spheroidal cesium lead chloride–bromide quantum dots and a fast determination of their size and halide content. *Nano Letters*, 22(20):8168–8173, 2022.
- [12] Xiande Zheng, Lei Zhang, Xiaoge Wang, Yiguo Qing, Jie Chen, Yaoda Wu, Sihao Deng, Lunhua He, Fuhui Liao, Yan Wang, et al. Synthesis, structure, and superconductivity of b-site doped perovskite bismuth lead oxide with indium. *Inorganic Chemistry Frontiers*, 7(19):3561–3570, 2020.
- [13] Masood Mehrabian, Sina Dalir, Ghodrat Mahmoudi, Barbara Mirosław, Maria G Babashkina, Anna V Dektereva, and Damir A Safin. A highly stable all-inorganic cspbbr₃ perovskite solar cell. *European Journal of Inorganic Chemistry*, 2019(32):3699–3703, 2019.
- [14] Sijia Miao, Tianle Liu, Yujian Du, Xinyi Zhou, Jingnan Gao, Yichu Xie, Fengyi Shen, Yihua Liu, and Yuljae Cho. 2d material and perovskite heterostructure for optoelectronic applications. *Nanomaterials*, 12(12):2100, 2022.
- [15] Jingying Liu, Yunzhou Xue, Ziyu Wang, Zai-Quan Xu, Changxi Zheng, Bent Weber, Jingchao Song, Yusheng Wang, Yuerui Lu, Yupeng Zhang, et al. Two-dimensional ch₃nh₃pbi₃ perovskite: synthesis and optoelectronic application. *ACS nano*, 10(3):3536–3542, 2016.
- [16] Ufuk Erkc, Pablo Solís-Fernández, Hyun Goo Ji, Keisuke Shinokita, Yung-Chang Lin, Mina Maruyama, Kazu Suenaga, Susumu Okada, Kazunari Matsuda, and Hiroki Ago. Vapor phase selective growth of two-dimensional perovskite/ws₂ heterostructures for optoelectronic applications. *ACS applied materials & interfaces*, 11(43):40503–40511, 2019.

-
- [17] Antonio Gaetano Ricciardulli, Sheng Yang, Jurgen H Smet, and Michael Saliba. Emerging perovskite monolayers. *Nature Materials*, pages 1–12, 2021.
- [18] Constantinos C Stoumpos, Duyen H Cao, Daniel J Clark, Joshua Young, James M Rondinelli, Joon I Jang, Joseph T Hupp, and Mercuri G Kanatzidis. Ruddlesden–popper hybrid lead iodide perovskite 2d homologous semiconductors. *Chemistry of Materials*, 28(8):2852–2867, 2016.
- [19] Xun Xiao, Jian Zhou, Kepeng Song, Jingjing Zhao, Yu Zhou, Peter Neil Rudd, Yu Han, Ju Li, and Jinsong Huang. Layer number dependent ferroelasticity in 2d ruddlesden–popper organic-inorganic hybrid perovskites. *Nature Communications*, 12(1):1–6, 2021.
- [20] Michael Seitz, Alvaro J Magdaleno, Nerea Alcázar-Cano, Marc Meléndez, Tim J Lubbers, Sanne W Walraven, Sahar Pakdel, Elsa Prada, Rafael Delgado-Buscalioni, and Ferry Prins. Exciton diffusion in two-dimensional metal-halide perovskites. *Nature Communications*, 11(1):1–8, 2020.
- [21] Lianfeng Zhao, YunHui L Lin, Hoyeon Kim, Noel C Giebink, and Barry P Rand. Donor/acceptor charge-transfer states at two-dimensional metal halide perovskite and organic semiconductor interfaces. *ACS Energy Letters*, 3(11):2708–2712, 2018.
- [22] Aili Wang, Chuantian Zuo, Xiaobin Niu, Liming Ding, Jianning Ding, and Feng Hao. Recent promise of lead-free halide perovskites in optoelectronic applications. *Chemical Engineering Journal*, 451:138926, 2023.

- [23] Michael Saliba. Polyelemental, multicomponent perovskite semiconductor libraries through combinatorial screening. *Advanced Energy Materials*, 9(25):1803754, 2019.
- [24] Akihiro Kojima, Kenjiro Teshima, Yasuo Shirai, and Tsutomu Miyasaka. Organometal halide perovskites as visible-light sensitizers for photovoltaic cells. *Journal of the American Chemical Society*, 131(17):6050–6051, 2009.
- [25] Luciana C Schmidt, Antonio Pertegás, Soranyel Gonzalez-Carrero, Olga Malinkiewicz, Said Agouram, Guillermo Minguez Espallargas, Henk J Bolink, Raquel E Galian, and Julia Perez-Prieto. Nontemplate synthesis of $\text{CH}_3\text{NH}_3\text{PbBr}_3$ perovskite nanoparticles. *Journal of the American Chemical Society*, 136(3):850–853, 2014.
- [26] Jin-Tai Lin, Chen-Cheng Liao, Chia-Shuo Hsu, Deng-Gao Chen, Hao-Ming Chen, Ming-Kang Tsai, Pi-Tai Chou, and Ching-Wen Chiu. Harnessing dielectric confinement on tin perovskites to achieve emission quantum yield up to 21%. *Journal of the American Chemical Society*, 141(26):10324–10330, 2019.
- [27] Arkajyoti Chakrabarty, Samridhi Satija, Upanshu Gangwar, and Sameer Sapra. Precursor-mediated synthesis of shape-controlled colloidal CsPbBr_3 perovskite nanocrystals and their nanofiber-directed self-assembly. *Chemistry of Materials*, 32(2):721–733, 2019.
- [28] Juan Navarro Arenas. Optoelectronic devices based on caesium lead halide perovskite nanocrystals. 2020.
- [29] Jean-Christophe Blancon, Jacky Even, Costas C Stoumpos, Mercuri G Kanatzidis, and Aditya D Mohite. Semiconductor physics

-
- of organic–inorganic 2d halide perovskites. *Nature Nanotechnology*, 15(12):969–985, 2020.
- [30] Pengchen Zhu and Jia Zhu. Low-dimensional metal halide perovskites and related optoelectronic applications. *InfoMat*, 2(2):341–378, 2020.
- [31] Duyen H Cao, Constantinos C Stoumpos, Omar K Farha, Joseph T Hupp, and Mercuri G Kanatzidis. 2d homologous perovskites as light-absorbing materials for solar cell applications. *Journal of the American Chemical Society*, 137(24):7843–7850, 2015.
- [32] Letian Dou. Emerging two-dimensional halide perovskite nanomaterials. *Journal of Materials Chemistry C*, 5(43):11165–11173, 2017.
- [33] Roman Krahne. Two-dimensional layered perovskites for photonic devices. 2021.
- [34] Kai Leng, Wei Fu, Yanpeng Liu, Manish Chhowalla, and Kian Ping Loh. From bulk to molecularly thin hybrid perovskites. *Nature Reviews Materials*, 5(7):482–500, 2020.
- [35] Zhizhong Chen, Yuwei Guo, Esther Wertz, and Jian Shi. Merits and challenges of ruddlesden–popper soft halide perovskites in electro-optics and optoelectronics. *Advanced Materials*, 31(1):1803514, 2019.
- [36] Yani Chen, Yong Sun, Jiajun Peng, Junhui Tang, Kaibo Zheng, and Ziqi Liang. 2d ruddlesden–popper perovskites for optoelectronics. *Advanced Materials*, 30(2):1703487, 2018.
- [37] Zewen Xiao, Weiwei Meng, Jianbo Wang, and Yanfa Yan. Defect properties of the two-dimensional $(\text{CH}_3\text{NH}_3)_2\text{Pb}(\text{SCN})_2$ per-

- ovskite: a density-functional theory study. *Physical Chemistry Chemical Physics*, 18(37):25786–25790, 2016.
- [38] Junze Li, Jun Wang, Yingjun Zhang, Haizhen Wang, Gaoming Lin, Xuan Xiong, Weihang Zhou, Hongmei Luo, and Dehui Li. Fabrication of single phase 2d homologous perovskite microplates by mechanical exfoliation. *2D Materials*, 5(2):021001, 2018.
- [39] Balaji Dhanabalan, Andrea Castelli, Milan Palei, Davide Spirito, Liberato Manna, Roman Krahne, and Milena Arciniegas. Simple fabrication of layered halide perovskite platelets and enhanced photoluminescence from mechanically exfoliated flakes. *Nanoscale*, 11(17):8334–8342, 2019.
- [40] Luis K Ono, Shengzhong Liu, and Yabing Qi. Reducing detrimental defects for high-performance metal halide perovskite solar cells. *Angewandte Chemie International Edition*, 59(17):6676–6698, 2020.
- [41] Yuanhang Cheng, Yong Peng, Alex K-Y Jen, and Hin-Lap Yip. Development and challenges of metal halide perovskite solar modules. *Solar RRL*, 6(3):2100545, 2022.
- [42] Zhi-Kuang Tan, Reza Saberi Moghaddam, May Ling Lai, Pablo Docompato, Ruben Higler, Felix Deschler, Michael Price, Aditya Sadhanala, Luis M Pazos, Dan Credgington, et al. Bright light-emitting diodes based on organometal halide perovskite. *Nature nanotechnology*, 9(9):687–692, 2014.
- [43] Guichuan Xing, Nripan Mathews, Swee Sien Lim, Natalia Yantara, Xinfeng Liu, Dharani Sabba, Michael Grätzel, Subodh Mhaisalkar,

-
- and Tze Chien Sum. Low-temperature solution-processed wavelength-tunable perovskites for lasing. *Nature materials*, 13(5):476–480, 2014.
- [44] Qing Zhang, Son Tung Ha, Xinfeng Liu, Tze Chien Sum, and Qihua Xiong. Room-temperature near-infrared high-q perovskite whispering-gallery planar nanolasers. *Nano letters*, 14(10):5995–6001, 2014.
- [45] Felix Deschler, Michael Price, Sandeep Pathak, Lina E Klintberg, David-Dominik Jarausch, Ruben Higler, Sven Huttner, Tomas Leijtens, Samuel D Stranks, Henry J Snaith, et al. High photoluminescence efficiency and optically pumped lasing in solution-processed mixed halide perovskite semiconductors. *The journal of physical chemistry letters*, 5(8):1421–1426, 2014.
- [46] Xiaoming Wen, Anita Ho-Baillie, Shujuan Huang, Rui Sheng, Sheng Chen, Hsien-chen Ko, and Martin A Green. Mobile charge-induced fluorescence intermittency in methylammonium lead bromide perovskite. *Nano Letters*, 15(7):4644–4649, 2015.
- [47] Th Basché, WE Moerner, M Orrit, and H Talon. Photon antibunching in the fluorescence of a single dye molecule trapped in a solid. *Physical review letters*, 69(10):1516, 1992.
- [48] Stephen A Empedocles, David J Norris, and Mounqi G Bawendi. Photoluminescence spectroscopy of single cdse nanocrystallite quantum dots. *Physical review letters*, 77(18):3873, 1996.
- [49] Peter Michler, Alper Kiraz, Christoph Becher, WV Schoenfeld, PM Petroff, Lidong Zhang, Ella Hu, and A Imamoglu. A quantum dot single-photon turnstile device. *science*, 290(5500):2282–2285, 2000.

- [50] Christian Kurtsiefer, Sonja Mayer, Patrick Zarda, and Harald Weinfurter. Stable solid-state source of single photons. *Physical review letters*, 85(2):290, 2000.
- [51] Rosa Brouri, Alexios Beveratos, Jean-Philippe Poizat, and Philippe Grangier. Photon antibunching in the fluorescence of individual color centers in diamond. *Optics letters*, 25(17):1294–1296, 2000.
- [52] Matthew D Eisaman, Jingyun Fan, Alan Migdall, and Sergey V Polyakov. Invited review article: Single-photon sources and detectors. *Review of scientific instruments*, 82(7):071101, 2011.
- [53] Jeremy L O’Brien. Optical quantum computing. *Science*, 318(5856):1567–1570, 2007.
- [54] Christian L Degen, Friedemann Reinhard, and Paola Cappellaro. Quantum sensing. *Reviews of modern physics*, 89(3):035002, 2017.
- [55] Loredana Protesescu, Sergii Yakunin, Maryna I Bodnarchuk, Franziska Krieg, Riccarda Caputo, Christopher H Hendon, Ruo Xi Yang, Aron Walsh, and Maksym V Kovalenko. Nanocrystals of cesium lead halide perovskites (cs₄pbx₃, x= cl, br, and i): novel optoelectronic materials showing bright emission with wide color gamut. *Nano letters*, 15(6):3692–3696, 2015.
- [56] Franziska Krieg, Stefan T Ochsenbein, Sergii Yakunin, Stephanie Ten Brinck, Philipp Aellen, Adrian Suess, Baptiste Clerc, Dominic Guggisberg, Olga Nazarenko, Yevhen Shynkarenko, et al. Colloidal cs₄pbx₃ (x= cl, br, i) nanocrystals 2.0: Zwitterionic capping ligands for improved durability and stability. *ACS energy letters*, 3(3):641–646, 2018.

-
- [57] Aaron Malinoski, Guoxiang Hu, and Chen Wang. Strong bidentate coordination for surface passivation and ligand-shell engineering of lead halide perovskite nanocrystals in the strongly quantum-confined regime. *The Journal of Physical Chemistry C*, 125(44):24521–24530, 2021.
- [58] Hyunki Kim, Nicholas Hight-Huf, Ji-Hwan Kang, Phoebe Bisnoff, Suvini Sundararajan, Theo Thompson, Michael Barnes, Ryan C Hayward, and Todd Emrick. Polymer zwitterions for stabilization of cspbbr₃ perovskite nanoparticles and nanocomposite films. *Angewandte Chemie*, 132(27):10894–10898, 2020.
- [59] Nadesh Fiuza-Maneiro, Kun Sun, Iago Lopez-Fernandez, Sergio Gomez-Grana, Peter Muller-Buschbaum, and Lakshminarayana Polavarapu. Ligand chemistry of inorganic lead halide perovskite nanocrystals. *ACS Energy Letters*, 8(2):1152–1191, 2023.
- [60] Yulia Lekina and Ze Xiang Shen. Excitonic states and structural stability in two-dimensional hybrid organic-inorganic perovskites. *Journal of Science: Advanced Materials and Devices*, 4(2):189–200, 2019.
- [61] T Thu Ha Do, Andres Granados del Aguila, Dong Zhang, Jun Xing, Sheng Liu, MA Prosnikov, Weibo Gao, Kai Chang, Peter CM Christianen, and Qihua Xiong. Bright exciton fine-structure in two-dimensional lead halide perovskites. *Nano Letters*, 20(7):5141–5148, 2020.
- [62] Rodolfo Canet-Albiach, Marie Krecmarova, José Bosch Bailach, Andrés F Gualdrón-Reyes, Jesús Rodríguez-Romero, Setatira Gorji, Hamid Pashaei-Adl, Iván Mora-Seró, Juan P Martinez Pastor,

- Juan Francisco Sánchez-Royo, et al. Revealing giant exciton fine-structure splitting in two-dimensional perovskites using van der waals passivation. *Nano Letters*, 22(18):7621–7627, 2022.
- [63] Martin A Green, Anita Ho-Baillie, and Henry J Snaith. The emergence of perovskite solar cells. *Nature Photonics*, 8(7):506–514, 2014.
- [64] James V Passarelli, Catherine M Mauck, Samuel W Winslow, Collin F Perkinson, Jacob C Bard, Hiroaki Sai, Kristopher W Williams, Ashwin Narayanan, Daniel J Fairfield, Mark P Hendricks, et al. Tunable exciton binding energy in 2d hybrid layered perovskites through donor–acceptor interactions within the organic layer. *Nature Chemistry*, 12(8):672–682, 2020.
- [65] Simon Kahmann, Eelco K Tekelenburg, Herman Duim, Machteld E Kamminga, and Maria A Loi. Extrinsic nature of the broad photoluminescence in lead iodide-based ruddlesden–popper perovskites. *Nature Communications*, 11(1):1–8, 2020.
- [66] Anthony Mark Fox, Mark Fox, et al. *Quantum optics: an introduction*, volume 15. Oxford university press, 2006.
- [67] R Lo Savio, SL Portalupi, D Gerace, A Shakoov, TF Krauss, L O’Faolain, LC Andreani, and Matteo Galli. Room-temperature emission at telecom wavelengths from silicon photonic crystal nanocavities. *Applied Physics Letters*, 98(20):201106, 2011.
- [68] Andrew Wood et al. Emerging quantum correlations from interacting fibre-cavity polaritons. 2019.
- [69] Rui Su, Antonio Fieramosca, Qing Zhang, Hai Son Nguyen, Emmanuelle Deleporte, Zhanghai Chen, Daniele Sanvitto, Timothy CH

-
- Liew, and Qihua Xiong. Perovskite semiconductors for room-temperature exciton-polaritonics. *Nature Materials*, 20(10):1315–1324, 2021.
- [70] Guillermo Muñoz-Matutano, Andrew Wood, Mattias Johansson, Xavier Vidal, Ben Q Baragiola, Andreas Reinhard, Aristide Lemaître, Jacqueline Bloch, Alberto Amo, Gilles Nogues, et al. Emergence of quantum correlations from interacting fibre-cavity polaritons. *Nature Materials*, 18(3):213–218, 2019.
- [71] Aymeric Delteil, Thomas Fink, Anne Schade, Sven Höfling, Christian Schneider, and Ataç İmamoğlu. Towards polariton blockade of confined exciton-polaritons. *Nature Materials*, 18(3):219–222, 2019.
- [72] Han Nijssen and IJH Isbrücker. Notes on the guiane species of corydoras lacépède, 1803, with descriptions of seven new species and designation of a neotype for corydoras punctatus (bloch, 1794)—(pisces, cypriniformes, callichthyidae). *Zoologische Mededelingen*, 42(5):21–50, 1967.
- [73] Peter Michler. *Single quantum dots: Fundamentals, applications and new concepts*, volume 90. Springer Science & Business Media, 2003.
- [74] Sean A Blanton, Ahmad Dehestani, Peter C Lin, and Philippe Guyot-Sionnest. Photoluminescence of single semiconductor nanocrystals by two-photon excitation microscopy. *Chemical physics letters*, 229(3):317–322, 1994.
- [75] Stephen A Empedocles, Robert Neuhauser, Kentaro Shimizu, and Mounji G Bawendi. Photoluminescence from single semiconductor nanostructures. *Advanced Materials*, 11(15):1243–1256, 1999.

- [76] Stephen A Emedocles and Mounji G Bawendi. Influence of spectral diffusion on the line shapes of single cdse nanocrystallite quantum dots. *The Journal of Physical Chemistry B*, 103(11):1826–1830, 1999.
- [77] Manoj Nirmal, Bashir O Dabbousi, Mounji G Bawendi, JJ Macklin, JK Trautman, TD Harris, and Louis E Brus. Fluorescence intermittency in single cadmium selenide nanocrystals. *Nature*, 383(6603):802–804, 1996.
- [78] Alexander L Efros and David J Nesbitt. Origin and control of blinking in quantum dots. *Nature Nanotechnology*, 11(8):661–671, 2016.
- [79] Yongfen Chen, Javier Vela, Han Htoon, Joanna L Casson, Donald J Werder, David A Bussian, Victor I Klimov, and Jennifer A Hollingsworth. “giant” multishell cdse nanocrystal quantum dots with suppressed blinking. *Journal of the American Chemical Society*, 130(15):5026–5027, 2008.
- [80] Guillermo Muñoz Matutano. *Excitons and trions in isolated cuⁱa notic nanostructures of indium arsenide*. PhD thesis, Universitat de València, 2010.
- [81] Jason McKeever, Andreea Boca, A David Boozer, Joseph R Buck, and H Jeff Kimble. Experimental realization of a one-atom laser in the regime of strong coupling. *Nature*, 425(6955):268–271, 2003.
- [82] Charles Kittel and Paul McEuen. *Introduction to solid state physics*. John Wiley & Sons, 2018.
- [83] Sotirios Baskoutas and Andreas F Terzis. Size-dependent band gap of colloidal quantum dots. *Journal of applied physics*, 99(1):013708, 2006.

-
- [84] Louis Brus. Electronic wave functions in semiconductor clusters: experiment and theory. *The Journal of Physical Chemistry*, 90(12):2555–2560, 1986.
- [85] Alexander L Efros and Al L Efros. Interband absorption of light in a semiconductor sphere. *Sov. Phys. Semicond*, 16(7):772–775, 1982.
- [86] Dennis Sullivan and DS Citrin. Time-domain simulation of two electrons in a quantum dot. *Journal of Applied Physics*, 89(7):3841–3846, 2001.
- [87] Litty Irimpan, VPN Nampoori, and P Radhakrishnan. Visible luminescence mechanism in nano zno under weak confinement regime. *Journal of applied physics*, 104(11):113112, 2008.
- [88] PIJUS KANTI Samanta. Strong and weak quantum confinement and size dependent optoelectronic properties of zinc oxide. *Ann Univ Craiova Phys*, 28:17–23, 2018.
- [89] Howard Reiss, CS Fuller, and FJ Morin. Chemical interactions among defects in germanium and silicon. *Bell System Technical Journal*, 35(3):535–636, 1956.
- [90] Jacques I Pankove. *Optical processes in semiconductors*. Courier Corporation, 1975.
- [91] Naoya Aihara, Kunihiko Tanaka, Hisao Uchiki, Ayaka Kanai, and Hideaki Araki. Donor-acceptor pair recombination luminescence from monoclinic Cu_2Sns_3 thin film. *Applied Physics Letters*, 107(3):032101, 2015.

- [92] ZC Feng, A Mascarenhas, and WJ Choyke. Low temperature photoluminescence spectra of (001) cdte films grown by molecular beam epitaxy at different substrate temperatures. *Journal of luminescence*, 35(6):329–341, 1986.
- [93] Joanna M Urban, Trang Thi Huyen Nguyen, Gabriel Chehade, Aymeric Delteil, Gaëlle Trippé-Allard, Geraud Delpont, Emmanuelle Deleporte, Jean-Pierre Hermier, and Damien Garrot. Discrete donor-acceptor pair transitions in $\text{ch}_3\text{nh}_3\text{pb}_3$ perovskite single crystals. *physica status solidi (RRL)–Rapid Research Letters*, 2023.
- [94] Jenya Tilchin, Dmitry N Dirin, Georgy I Maikov, Aldona Sashchiuk, Maksym V Kovalenko, and Efrat Lifshitz. Hydrogen-like wannier-mott excitons in single crystal of methylammonium lead bromide perovskite. *ACS nano*, 10(6):6363–6371, 2016.
- [95] Simone L Portalupi, Matteo Galli, Christopher Reardon, TF Krauss, Liam O’Faolain, Lucio C Andreani, and Dario Gerace. Planar photonic crystal cavities with far-field optimization for high coupling efficiency and quality factor. *Optics express*, 18(15):16064–16073, 2010.
- [96] S Roshan Entezar, M Habil Karimi, and H Pashaei Adl. Optical isolation via one-dimensional magneto-photonic crystals containing nonlinear defect layer. *Optics Communications*, 352:91–95, 2015.
- [97] Hamid Pashaei Adl, Farzaneh Bayat, Nadia Ghorani, Sohrab Ahmadi-Kandjani, and Habib Tajalli. A defective 1-d photonic crystal-based chemical sensor in total internal reflection geometry. *IEEE Sensors Journal*, 17(13):4046–4051, 2017.

-
- [98] B Tavakkoly Moghaddam, S Roshan Entezar, and H Pashaei Adl. Nonlinear properties of a graded-index photonic heterostructure. *Pramana*, 80(5):887–894, 2013.
- [99] Amnon Yariv and Pochi Yeh. *Optical waves in crystals*, volume 5. Wiley New York, 1984.
- [100] Edward M Purcell, Henry Cutler Torrey, and Robert V Pound. Resonance absorption by nuclear magnetic moments in a solid. *Physical review*, 69(1-2):37, 1946.
- [101] Lukas Novotny and Bert Hecht. *Principles of nano-optics*. Cambridge university press, 2012.
- [102] KH Drexhage. Beeinflussung der fluoreszenz eins europiumchelates durch einen spiegel. *Ber. Bunsenges. Phys. Chem.*, 70:1179, 1966.
- [103] Ph Goy, JM Raimond, M Gross, and S Haroche. Observation of cavity-enhanced single-atom spontaneous emission. *Physical review letters*, 50(24):1903, 1983.
- [104] Daniel Kleppner. Inhibited spontaneous emission. *Physical review letters*, 47(4):233, 1981.
- [105] Eli Yablonovitch. Inhibited spontaneous emission in solid-state physics and electronics. *Physical review letters*, 58(20):2059, 1987.
- [106] Sajeev John. Strong localization of photons in certain disordered dielectric superlattices. *Physical review letters*, 58(23):2486, 1987.
- [107] John D Joannopoulos, Pierre R Villeneuve, and Shanhui Fan. Photonic crystals: putting a new twist on light. *Nature*, 386(6621):143–149, 1997.

- [108] JK Trautman and JJ Macklin. Time-resolved spectroscopy of single molecules using near-field and far-field optics. *Chemical Physics*, 205(1-2):221–229, 1996.
- [109] Hamid Pashaei Adl, Setatira Gorji, Mojtaba Karimi Habil, Isaac Suarez, Vladimir S Chirvony, Andres F Gualdrón-Reyes, Ivan Mora-Sero, Luisa M Valencia, Maria de la Mata, Jesus Hernandez-Saz, et al. Purcell enhancement and wavelength shift of emitted light by cspbi3 perovskite nanocrystals coupled to hyperbolic metamaterials. *ACS photonics*, 7(11):3152–3160, 2020.
- [110] Hamid Pashaei Adl, Setatira Gorji, Andrés F Gualdrón-Reyes, Iván Mora-Seró, Isaac Suárez, and Juan P Martínez-Pastor. Enhanced spontaneous emission of cspbi3 perovskite nanocrystals using a hyperbolic metamaterial modified by dielectric nanoantenna. *Nanomaterials*, 13(1):11, 2023.
- [111] Jean-Michel Raimond and Serge Haroche. Exploring the quantum. *Oxford University Press*, 82:86, 2006.
- [112] Mattia Signoretto, Nathalie Zink-Lorre, Juan P Martínez-Pastor, Enrique Font-Sanchis, Vladimir S Chirvony, Ángela Sastre-Santos, Fernando Fernández-Lázaro, and Isaac Suárez. Purcell-enhancement of the radiative pl decay in perylenediimides by coupling with silver nanoparticles into waveguide modes. *Applied Physics Letters*, 111(8):081102, 2017.
- [113] Thi Tuyen Ngo, Isaac Suarez, Rafael S Sanchez, Juan P Martinez-Pastor, and Ivan Mora-Sero. Single step deposition of an interacting layer of a perovskite matrix with embedded quantum dots. *Nanoscale*, 8(30):14379–14383, 2016.

-
- [114] Seth Coe-Sullivan, Jonathan S Steckel, W-K Woo, Mounqi G Bawendi, and Vladimir Bulović. Large-area ordered quantum-dot monolayers via phase separation during spin-casting. *Advanced Functional Materials*, 15(7):1117–1124, 2005.
- [115] Marvin Minsky. Memoir on inventing the confocal scanning microscope. *Scanning*, 10(4):128–138, 1988.
- [116] CJR Sheppard and A Choudhury. Image formation in the scanning microscope. *Optica Acta: International Journal of Optics*, 24(10):1051–1073, 1977.
- [117] Hamid Pashaei Adl, Setatira Gorji, Guillermo Muñoz-Matutano, Raúl I Sánchez-Alarcón, Rafael Abargues, Andrés F Gualdrón-Reyes, Iván Mora-Seró, and Juan P Martínez-Pastor. Homogeneous and inhomogeneous broadening in single perovskite nanocrystals investigated by micro-photoluminescence. *Journal of Luminescence*, 240:118453, 2021.
- [118] Amicia D Elliott. Confocal microscopy: principles and modern practices. *Current protocols in cytometry*, 92(1):e68, 2020.
- [119] Tony Wilson. Confocal microscopy. *San Diego*, 1990.
- [120] Martin Kroner. *Resonant photon-exciton interaction in semiconductor quantum dots*. PhD thesis, lmu, 2008.
- [121] Stefan Wilhelm, Bernhard Grobler, Martin Gluch, and Hartmut Heinz. Confocal laser scanning microscopy: principles. *Microscopy from Carl Zeiss, microspecial*, 2003.

- [122] Nathan S Claxton, Thomas J Fellers, and Michael W Davidson. Laser scanning confocal microscopy. *Encyclopedia of Medical Devices and Instrumentation*, 21:1–37, 2006.
- [123] Robert H Webb. Confocal optical microscopy. *Reports on Progress in Physics*, 59(3):427, 1996.
- [124] J Benito Alén Millán. *Espectroscopía óptica confocal aplicada al estudio de cajas cuánticas aisladas de arseniuro de indio (InAS)*. PhD thesis, Universitat de València, 2005.
- [125] P Török and Luciano Mule’Stagno. Applications of scanning optical microscopy in materials science to detect bulk microdefects in semiconductors. *Journal of Microscopy*, 188(1):1–16, 1997.
- [126] Frank L Pedrotti, Leno M Pedrotti, and Leno S Pedrotti. *Introduction to optics*. Cambridge University Press, 2017.
- [127] <https://www.ivgfiber.com/fibers.htm>.
- [128] Jan M Binder, Alexander Stark, Nikolas Tomek, Jochen Scheuer, Florian Frank, Kay D Jahnke, Christoph Müller, Simon Schmitt, Mathias H Metsch, Thomas Uden, et al. Qudi: A modular python suite for experiment control and data processing. *SoftwareX*, 6:85–90, 2017.
- [129] Ernst Ruska. The development of the electron microscope and of electron microscopy (nobel lecture). *Angewandte Chemie International Edition in English*, 26(7):595–605, 1987.
- [130] Naoya Shibata, Yuji Kohno, A Nakamura, S Morishita, Takehito Seki, A Kumamoto, Hidetaka Sawada, Takeru Matsumoto, SD Findlay, and

-
- Yuichi Ikuhara. Atomic resolution electron microscopy in a magnetic field free environment. *Nature communications*, 10(1):1–5, 2019.
- [131] Leif AA Pettersson, Lucimara S Roman, and Olle Inganäs. Modeling photocurrent action spectra of photovoltaic devices based on organic thin films. *Journal of Applied Physics*, 86(1):487–496, 1999.
- [132] Peter Peumans, Aharon Yakimov, and Stephen R Forrest. Small molecular weight organic thin-film photodetectors and solar cells. *Journal of Applied Physics*, 93(7):3693–3723, 2003.
- [133] Max Born and Emil Wolf. *Principles of optics: electromagnetic theory of propagation, interference and diffraction of light*. Elsevier, 2013.
- [134] Klaus-Jürgen Bathe. Finite element method. *Wiley encyclopedia of computer science and engineering*, pages 1–12, 2007.
- [135] Gouri Dhatt, Emmanuel Lefrançois, and Gilbert Touzot. *Finite element method*. John Wiley & Sons, 2012.
- [136] JN Reddy. An introduction to the finite element method mcgraw-hill. *Inc., New York*, 1993.
- [137] <https://www.comsol.com/multiphysics/finite-element-method>.
- [138] Gabriele Raino, Georgian Nedelcu, Loredana Protesescu, Maryna I Bodnarchuk, Maksym V Kovalenko, Rainer F Mahrt, and Thilo Stoferle. Single cesium lead halide perovskite nanocrystals at low temperature: fast single-photon emission, reduced blinking, and exciton fine structure. *ACS nano*, 10(2):2485–2490, 2016.

- [139] Fengrui Hu, Chunyang Yin, Huichao Zhang, Chun Sun, William W Yu, Chunfeng Zhang, Xiaoyong Wang, Yu Zhang, and Min Xiao. Slow auger recombination of charged excitons in nonblinking perovskite nanocrystals without spectral diffusion. *Nano letters*, 16(10):6425–6430, 2016.
- [140] Young-Shin Park, Shaojun Guo, Nikolay S Makarov, and Victor I Klimov. Room temperature single-photon emission from individual perovskite quantum dots. *ACS nano*, 9(10):10386–10393, 2015.
- [141] Simon C Boehme, Maryna I Bodnarchuk, Max Burian, Federica Bertolotti, Ihor Cherniukh, Caterina Bernasconi, Chenglian Zhu, Rolf Erni, Heinz Amenitsch, Denys Naumenko, et al. Strongly confined cspbbr3 quantum dots as quantum emitters and building blocks for rhombic superlattices. *ACS nano*, 2023.
- [142] Igor Aharonovich, Dirk Englund, and Milos Toth. Solid-state single-photon emitters. *Nature Photonics*, 10(10):631–641, 2016.
- [143] Abhishek Swarnkar, Vikash Kumar Ravi, and Angshuman Nag. Beyond colloidal cesium lead halide perovskite nanocrystals: analogous metal halides and doping. *ACS Energy Letters*, 2(5):1089–1098, 2017.
- [144] Michael M Lee, Joël Teuscher, Tsutomu Miyasaka, Takuro N Murakami, and Henry J Snaith. Efficient hybrid solar cells based on meso-superstructured organometal halide perovskites. *Science*, 338(6107):643–647, 2012.
- [145] Wanyi Nie, Hsinhan Tsai, Reza Asadpour, Jean-Christophe Blancon, Amanda J Neukirch, Gautam Gupta, Jared J Crochet, Manish Chhowalla, Sergei Tretiak, Muhammad A Alam, et al. High-efficiency

-
- solution-processed perovskite solar cells with millimeter-scale grains. *Science*, 347(6221):522–525, 2015.
- [146] Nam Joong Jeon, Jun Hong Noh, Woon Seok Yang, Young Chan Kim, Seungchan Ryu, Jangwon Seo, and Sang Il Seok. Compositional engineering of perovskite materials for high-performance solar cells. *Nature*, 517(7535):476–480, 2015.
- [147] Franziska Krieg, Peter C Sercel, Max Burian, Hordii Andrusiv, Maryna I Bodnarchuk, Thilo Stoferle, Rainer F Mahrt, Denys Naumenko, Heinz Amenitsch, Gabriele Rainò, et al. Monodisperse long-chain sulfobetaine-capped cspbbr3 nanocrystals and their superfluorescent assemblies. *ACS central science*, 7(1):135–144, 2020.
- [148] Hamid Pashaei Adl. *Manipulation of emitted light by structured lead halide perovskite nanocrystals for photonics applications*. PhD thesis, Universitat de València, 2021.
- [149] Hendrik Utzat, Weiwei Sun, Alexander EK Kaplan, Franziska Krieg, Matthias Ginterseder, Boris Spokoyny, Nathan D Klein, Katherine E Shulenberger, Collin F Perkinson, Maksym V Kovalenko, et al. Coherent single-photon emission from colloidal lead halide perovskite quantum dots. *Science*, 363(6431):1068–1072, 2019.
- [150] Setatira Gorji, Marie Krecmarova, Alejandro Molina, Maria C Asensio, Andrés F Gualdrón-Reyes, Jesús Rodríguez-Romero, Hamid Pashaei-Adl, Rodolfo Canet-Albiach, Luca Schio, Massimo Tormen, et al. Donor-acceptor discrete optical emission in 2d perovskites. *arXiv preprint arXiv:2204.06400*, 2022.

- [151] G Moody, ME Siemens, AD Bristow, X Dai, D Karaiskaj, AS Bracker, D Gammon, and ST Cundiff. Exciton-exciton and exciton-phonon interactions in an interfacial gas quantum dot ensemble. *Physical Review B*, 83(11):115324, 2011.
- [152] Caixia Huo, Chee Fai Fong, Mohamed-Raouf Amara, Yuqing Huang, Bo Chen, Hua Zhang, Lingjun Guo, Hejun Li, Wei Huang, Carole Diederichs, et al. Optical spectroscopy of single colloidal cspbbr3 perovskite nanoplatelets. *Nano Letters*, 20(5):3673–3680, 2020.
- [153] Junyang Yuan, Dawei Zhou, Chen Zhuang, Yong Zhou, Chunfeng Zhang, Lin Wang, Min Xiao, and Xiaoyong Wang. Single-photon emission from single microplate mapbi3 nanocrystals with ultranarrow photoluminescence linewidths and exciton fine structures. *Advanced Optical Materials*, 10(18):2200606, 2022.
- [154] Shengnan Feng, Qilin Qin, Xiaopeng Han, Chunfeng Zhang, Xiaoyong Wang, Tao Yu, and Min Xiao. Universal existence of localized single-photon emitters in the perovskite film of all-inorganic cspbbr3 microcrystals. *Advanced Materials*, 34(1):2106278, 2022.
- [155] Chunyang Yin, Liyang Chen, Nan Song, Yan Lv, Fengrui Hu, Chun Sun, W Yu William, Chunfeng Zhang, Xiaoyong Wang, Yu Zhang, et al. Bright-exciton fine-structure splittings in single perovskite nanocrystals. *Physical review letters*, 119(2):026401, 2017.
- [156] Ming Fu, Philippe Tamarat, Jean-Baptiste Trebbia, Maryna I Bodnarchuk, Maksym V Kovalenko, Jacky Even, and Brahim Lounis. Unraveling exciton–phonon coupling in individual fapbi 3 nanocrystals emitting near-infrared single photons. *Nature communications*, 9(1):1–10, 2018.

-
- [157] Fengrui Hu, Huichao Zhang, Chun Sun, Chunyang Yin, Bihu Lv, Chunfeng Zhang, William W Yu, Xiaoyong Wang, Yu Zhang, and Min Xiao. Superior optical properties of perovskite nanocrystals as single photon emitters. *ACS nano*, 9(12):12410–12416, 2015.
- [158] Ming Fu, Philippe Tamarat, He Huang, Jacky Even, Andrey L Rogach, and Brahim Lounis. Neutral and charged exciton fine structure in single lead halide perovskite nanocrystals revealed by magneto-optical spectroscopy. *Nano letters*, 17(5):2895–2901, 2017.
- [159] Buyang Yu, Chunfeng Zhang, Lan Chen, Xinyu Huang, Zhengyuan Qin, Xiaoyong Wang, and Min Xiao. Exciton linewidth broadening induced by exciton–phonon interactions in cspbbr3 nanocrystals. *The Journal of Chemical Physics*, 154(21):214502, 2021.
- [160] Yan Lv, Chunyang Yin, Chunfeng Zhang, William W Yu, Xiaoyong Wang, Yu Zhang, and Min Xiao. Quantum interference in a single perovskite nanocrystal. *Nano Letters*, 19(7):4442–4447, 2019.
- [161] Chenglian Zhu, Tan Nguyen, Simon C Boehme, Anastasiia Moskalenko, Dmitry N Dirin, Maryna I Bodnarchuk, Claudine Katan, Jacky Even, Gabriele Rainò, and Maksym V Kovalenko. Many-body correlations and exciton complexes in cspbbr 3 quantum dots. *Advanced Materials*, 35(9):2208354, 2023.
- [162] Philippe Tamarat, Elise Prin, Yuliia Berezovska, Anastasiia Moskalenko, Thi Phuc Tan Nguyen, Chenghui Xia, Lei Hou, Jean-Baptiste Trebbia, Marios Zacharias, Laurent Pedesseau, et al. Universal scaling laws for charge-carrier interactions with quantum confinement in lead-halide perovskites. *Nature Communications*, 14(1):229, 2023.

- [163] Michael A Becker, Roman Vaxenburg, Georgian Nedelcu, Peter C Ser-
cel, Andrew Shabaev, Michael J Mehl, John G Michopoulos, Samuel G
Lambrakos, Noam Bernstein, John L Lyons, et al. Bright triplet ex-
citons in caesium lead halide perovskites. *Nature*, 553(7687):189–193,
2018.
- [164] Hong-Hua Fang, Raissa Raissa, Mustapha Abdu-Aguye, Sampson Ad-
jokatse, Graeme R Blake, Jacky Even, and Maria Antonietta Loi.
Photophysics of organic–inorganic hybrid lead iodide perovskite sin-
gle crystals. *Advanced Functional Materials*, 25(16):2378–2385, 2015.
- [165] TLKZ Schmidt, K Lischka, and W Zulehner. Excitation-power depen-
dence of the near-band-edge photoluminescence of semiconductors.
Physical Review B, 45(16):8989, 1992.
- [166] Yann Louyer, Louis Biadala, J-B Trebbia, Mark J Fernée, Ph Tama-
rat, and Brahim Lounis. Efficient biexciton emission in elongated
cdse/zns nanocrystals. *Nano letters*, 11(10):4370–4375, 2011.
- [167] Cesare Soci, Giorgio Adamo, Daniele Cortecchia, Kaiyang Wang,
Shumin Xiao, Qinghai Song, Anna Lena Schall-Giesecke, Piotr J
Cegielski, Max C Lemme, Dario Gerace, et al. Roadmap on per-
ovskite nanophotonics. *Optical Materials: X*, 17:100214, 2023.
- [168] Chenglian Zhu, Malwina Marczak, Leon Feld, Simon C Boehme,
Caterina Bernasconi, Anastasiia Moskalenko, Ihor Cherniukh, Dmitry
Dirin, Maryna I Bodnarchuk, Maksym V Kovalenko, et al. Room-
temperature, highly pure single-photon sources from all-inorganic lead
halide perovskite quantum dots. *Nano Letters*, 22(9):3751–3760, 2022.

-
- [169] Hina Igarashi, Mitsuaki Yamauchi, and Sadahiro Masuo. Correlation between single-photon emission and size of cesium lead bromide perovskite nanocrystals. *The Journal of Physical Chemistry Letters*, 14(9):2441–2447, 2023.
- [170] Weijie Li, Xin Lu, Sudipta Dubey, Luka Devenica, and Ajit Srivastava. Dipolar interactions between localized interlayer excitons in van der waals heterostructures. *Nature Materials*, 19(6):624–629, 2020.
- [171] Qinghai Tan, Jia-Min Lai, Xue-Lu Liu, Dan Guo, Yongzhou Xue, Xi-uming Dou, Bao-Quan Sun, Hui-Xiong Deng, Ping-Heng Tan, Igor Aharonovich, et al. Donor–acceptor pair quantum emitters in hexagonal boron nitride. *Nano Letters*, 2021.
- [172] Lukas Schmidt-Mende, Vladimir Dyakonov, Selina Olthof, Feray Ünlü, Khan Moritz Trong Lê, Sanjay Mathur, Andrei D Karabanov, Doru C Lupascu, Laura M Herz, Alexander Hinderhofer, et al. Roadmap on organic–inorganic hybrid perovskite semiconductors and devices. *APL Materials*, 9(10):109202, 2021.
- [173] Wancai Li, Chen Fang, Haizhen Wang, Shuai Wang, Junze Li, Jiaqi Ma, Jun Wang, Hongmei Luo, and Dehui Li. Surface depletion field in 2d perovskite microplates: Structural phase transition, quantum confinement and stark effect. *Nano Research*, 12(11):2858–2865, 2019.
- [174] Alice Berthelot, Ivan Favero, Guillaume Cassabois, Christophe Voisin, Claude Delalande, Ph Roussignol, Robson Ferreira, and Jean-Michel Gérard. Unconventional motional narrowing in the optical spectrum of a semiconductor quantum dot. *Nature Physics*, 2(11):759–764, 2006.

- [175] Feng Wang, Sai Bai, Wolfgang Tress, Anders Hagfeldt, and Feng Gao. Defects engineering for high-performance perovskite solar cells. *Npj Flexible Electronics*, 2(1):1–14, 2018.
- [176] Aboma Merdasa, Yuxi Tian, Rafael Camacho, Alexander Dobrovolsky, Elke Debroye, Eva L Unger, Johan Hofkens, Villy Sundstrom, and Ivan G Scheblykin. “supertrap” at work: extremely efficient non-radiative recombination channels in mapbi3 perovskites revealed by luminescence super-resolution imaging and spectroscopy. *ACS Nano*, 11(6):5391–5404, 2017.
- [177] Wan-Jian Yin, Tingting Shi, and Yanfa Yan. Unusual defect physics in ch₃nh₃pb₃ perovskite solar cell absorber. *Applied Physics Letters*, 104(6):063903, 2014.
- [178] Paul Pistor, Alejandro Ruiz, Andreu Cabot, and Victor Izquierdo-Roca. Advanced raman spectroscopy of methylammonium lead iodide: development of a non-destructive characterisation methodology. *Scientific Reports*, 6(1):1–8, 2016.
- [179] Martin Ledinsky, Philipp Loper, Bjoern Niesen, Jakub Holovsky, Soo-Jin Moon, Jun-Ho Yum, Stefaan De Wolf, Antonín Fejfar, and Christophe Ballif. Raman spectroscopy of organic–inorganic halide perovskites. *The Journal of Physical Chemistry Letters*, 6(3):401–406, 2015.
- [180] D. G. Thomas, M. Gershenson, and F. A. Trumbore. Pair spectra and “edge” emission in gallium phosphide. *Phys. Rev.*, 133:A269–A279, Jan 1964.

-
- [181] Xiaoxi Wu, M. Tuan Trinh, Daniel Niesner, Haiming Zhu, Zachariah Norman, Jonathan S. Owen, Omer Yaffe, Bryan J. Kudisch, and X.-Y. Zhu. Trap states in lead iodide perovskites. *Journal of the American Chemical Society*, 137(5):2089–2096, 2015. PMID: 25602495.
- [182] Lukas Kobr, Daniel M Gardner, Amanda L Smeigh, Scott M Dyar, Steven D Karlen, Raanan Carmieli, and Michael R Wasielewski. Fast photodriven electron spin coherence transfer: a quantum gate based on a spin exchange j-jump. *Journal of the American Chemical Society*, 134(30):12430–12433, 2012.
- [183] Yilei Wu, Jiawang Zhou, Jordan N Nelson, Ryan M Young, Matthew D Krzyaniak, and Michael R Wasielewski. Covalent radical pairs as spin qubits: Influence of rapid electron motion between two equivalent sites on spin coherence. *Journal of the American Chemical Society*, 140(40):13011–13021, 2018.
- [184] Qinghai Tan, Jia-Min Lai, Xue-Lu Liu, Dan Guo, Yongzhou Xue, Xi-uming Dou, Bao-Quan Sun, Hui-Xiong Deng, Ping-Heng Tan, Igor Aharonovich, et al. Donor–acceptor pair quantum emitters in hexagonal boron nitride. *Nano Letters*, 22(3):1331–1337, 2022.
- [185] Dario Ballarini and Simone De Liberato. Polaritonics: from microcavities to sub-wavelength confinement. *Nanophotonics*, 8(4):641–654, 2019.
- [186] Darrick E Chang, Vladan Vuletić, and Mikhail D Lukin. Quantum nonlinear optics—photon by photon. *Nature Photonics*, 8(9):685–694, 2014.

- [187] Natalia G Berloff, Matteo Silva, Kirill Kalinin, Alexis Askitopoulos, Julian D Töpfer, Pasquale Cilibrizzi, Wolfgang Langbein, and Pavlos G Lagoudakis. Realizing the classical xy hamiltonian in polariton simulators. *Nature materials*, 16(11):1120–1126, 2017.
- [188] F Baboux, L Ge, Thibault Jacqmin, M Biondi, E Galopin, A Lemaître, L Le Gratiet, Isabelle Sagnes, S Schmidt, Hakan E Türeci, et al. Bosonic condensation and disorder-induced localization in a flat band. *Physical review letters*, 116(6):066402, 2016.
- [189] G Dagvadorj, JM Fellows, S Matyjaśkiewicz, FM Marchetti, I Carusotto, and MH Szymańska. Nonequilibrium phase transition in a two-dimensional driven open quantum system. *Physical Review X*, 5(4):041028, 2015.
- [190] Sebastian Klemmt, Petr Stepanov, Thorsten Klein, Anna Minguzzi, and Maxime Richard. Thermal decoherence of a nonequilibrium polariton fluid. *Physical Review Letters*, 120(3):035301, 2018.
- [191] Mathias Steiner, Frank Schleifenbaum, Clemens Stupperich, Antonio Virgilio Failla, Achim Hartschuh, and Alfred Johann Meixner. Microcavity-controlled single-molecule fluorescence. *ChemPhysChem*, 6(10):2190–2196, 2005.
- [192] Alexey Chizhik, Frank Schleifenbaum, Raphael Gutbrod, Anna Chizhik, Dmitry Khoptyar, Alfred J Meixner, and Jörg Enderlein. Tuning the fluorescence emission spectra of a single molecule with a variable optical subwavelength metal microcavity. *Physical review letters*, 102(7):073002, 2009.

-
- [193] Mathias Steiner, Antonio Virgilio Failla, Achim Hartschuh, Frank Schleifenbaum, Clemens Stupperich, and Alfred Johann Meixner. Controlling molecular broadband-emission by optical confinement. *New Journal of Physics*, 10(12):123017, 2008.
- [194] Thomas W Ebbesen. Hybrid light–matter states in a molecular and material science perspective. *Accounts of chemical research*, 49(11):2403–2412, 2016.
- [195] Felix Bloch. Quantum mechanics of electrons in crystal lattices. *Z. Phys*, 52:555–600, 1928.
- [196] Feng Li, Yiming Li, Yin Cai, Peng Li, Haijun Tang, and Yan-peng Zhang. Tunable open-access microcavities for solid-state quantum photonics and polaritonics. *Advanced Quantum Technologies*, 2(10):1900060, 2019.
- [197] Natasha Tomm, Alisa Javadi, Nadia Olympia Antoniadis, Daniel Najer, Matthias Christian Löbl, Alexander Rolf Korsch, Rüdiger Schott, Sascha René Valentin, Andreas Dirk Wieck, Arne Ludwig, et al. A bright and fast source of coherent single photons. *Nature Nanotechnology*, 16(4):399–403, 2021.
- [198] Pascale Senellart, Glenn Solomon, and Andrew White. High-performance semiconductor quantum-dot single-photon sources. *Nature nanotechnology*, 12(11):1026–1039, 2017.
- [199] Hamed Arianfard, Jiayang Wu, Saulius Juodkazis, and David J Moss. Optical analogs of rabi splitting in integrated waveguide-coupled resonators. *Advanced Physics Research*, page 2200123, 2023.

- [200] S Jena, RB Tokas, S Thakur, and DV Udupa. Rabi-like splitting and refractive index sensing with hybrid tamm plasmon-cavity modes. *Journal of Physics D: Applied Physics*, 55(17):175104, 2022.
- [201] David Moss. Optical embodiments of rabi splitting based in photonic integrated waveguide-coupled resonators. 2023.